

# One and two-color photoassociation spectroscopy of ultracold $^{40}\text{Ca}$

Von der QUEST-Leibniz-Forschungsschule  
der Gottfried Wilhelm Leibniz Universität Hannover  
zur Erlangung des Grades

Doktor der Naturwissenschaften

Dr. rer. nat.

genehmigte Dissertation

von

Dipl.-Phys. Evgenij Pachomow

2017

**Referent:** Prof. Dr. rer. nat. Eberhard Tiemann  
Leibniz Universität Hannover

**Korreferent:** Prof. Dr. rer. nat. Fritz Riehle  
Physikalisch-Technische Bundesanstalt

**Tag der Disputation:** 28. März 2017

# Zusammenfassung

Der erste Teil der vorliegenden Arbeit beschäftigt sich mit der Messung der Verbreiterung des schmalbandigen molekularen Photoassoziationsüberganges  $^1S_0$ - $^3P_1$  in ultrakaltem Calcium bei hoher Anregungsleistung und der Untersuchung der Gültigkeit der Resonanzstreuungstheorie für die Beschreibung dieser Photoassoziationsspektren. Dabei wurden die theoretischen stimulierten Raten für den molekularen Übergang mittels Coupled Channel Modells ermittelt. Die experimentellen stimulierten Raten und die inelastischen Verlustraten wurden in Abhängigkeit von der eingestrahlten Laserleistung und von der Temperatur der Atomwolke untersucht und mit der Theorie verglichen. Aufgrund der gewonnenen Erkenntnisse wird die Vorhersage für die Anwendbarkeit von optischen Feshbachresonanzen mit geringen atomaren Verlusten für weitere Anwendungen gemacht.

Im zweiten Teil der Arbeit wird die Messung der vier schwächst gebundenen Rovibrationszustände im Calciumgrundzustand  $X^1\Sigma_g^+$  mittels der Zweifarben-Photoassoziationsspektroskopie vorgestellt. Durch die gemessenen Bindungsenergien konnten die langreichweitigen Dispersionskoeffizienten  $C_6$ ,  $C_8$ ,  $C_{10}$  inklusive Retardierung vollständig ermittelt werden, welche nun die komplette Beschreibung des Grundzustandes ermöglichen. Hierzu wurden die Franck-Condon Faktoren für die optischen Übergänge  $^1S_0$ - $^3P_1$  von angeregten gebundenen Vibrationszuständen aus den Molekülpotentialen zu  $\Omega = 0$  und  $\Omega = 1$  nach gebundenen molekularen Rovibrationszuständen in  $X^1\Sigma_g^+$  mit Hilfe des Coupled Channel Modells berechnet. Diese machen es möglich, die Aussage über die größten Zerfallskanäle und somit die effektive Erzeugung der Moleküle in einem bestimmten Grundzustand zu machen. Auf Basis des verbesserten Potentials wurde die Streulänge für  $^{40}\text{Ca}$  mit 10 mal kleiner Unsicherheit bestimmt und die Streulängen für alle homonuklearen Paare des stabilen Calciums mit den Aussichten für die Erzeugung des Bose-Einstein-Kondensats abgeschätzt.

**Schlüsselworte:** ultrakalte Calcium-Atome und Calcium-Moleküle, Ein- und Zweifarben-Photoassoziationsspektroskopie, molekulares Grundzustand-Potenzial, optische Feshbach-Resonanzen, Streulänge



# Abstract

In the first part of this thesis the measurement of the high power broadening of the ultra narrow transition  $^1S_0$ - $^3P_1$  to photoassociated calcium molecules is presented. The validity of the resonant scattering theory was investigated for the description of these photoassociation spectra. The stimulated rates for these molecular transitions are determined by means of a coupled channel model. The stimulated rates and corresponding two-body loss rates in dependency of the laser intensity and the temperature of the atomic cloud derived from the experiment are compared with the theoretical values. The feasibility of low loss optical Feshach resonances for further scientific applications was investigated.

The second part of the thesis focuses on the measurement of four most weakly bound molecular rovibrational states in the ground state  $X^1\Sigma_g^+$  of calcium via two-color photoassociation spectroscopy. Using the measured binding energies the long range dispersion coefficients  $C_6$ ,  $C_8$ ,  $C_{10}$  including retardation at long nuclear distances were determined enabling the complete description of the ground state potential. The radiative transitions from the excited vibrational states in the molecular potentials  $\Omega = 0$  and  $\Omega = 1$  of the  $^3P_1+^1S_0$  asymptote to the ro-vibrational states in the molecular ground potential  $X^1\Sigma_g^+$  were calculated. Based on these calculated values the effective production of ultracold  $\text{Ca}_2$  molecules in the desired ground state by spontaneous decay of excited molecules was predicted. The improved ground state potential allowed the calculation of the precise value of the s-wave scattering length improving its uncertainty by a factor of more than 10. Additionally theoretical values of the scattering lengths for all homonuclear pairs of stable calcium were given and estimation for the feasibility of the creation of Bose-Einstein condensates with these isotopes were proposed.

**Keywords:** ultracold calcium atoms and molecules, one and two-color photoassociation spectroscopy, molecular ground-state potential, optical Feshbach resonances, scattering length



# Contents

<b>1</b>	<b>Introduction</b>	<b>9</b>
<b>2</b>	<b>Towards low-loss optical Feshbach resonances</b>	<b>15</b>
2.1	One-color photoassociation spectroscopy . . . . .	15
2.1.1	Photoassociation . . . . .	15
2.1.2	Optical length $l_{\text{opt}}$ . . . . .	21
2.1.3	Losses and inelastic collision rate coefficient $K_{\text{in}}$ . . . . .	21
2.1.4	Spectral line shape . . . . .	23
2.1.5	Inhomogeneous Doppler broadening of the measured spectral lines	24
2.1.6	Scattering length $a$ . . . . .	25
2.1.7	Classification of Ca resonance strength of $^1S_0$ - $^3P_1$ . . . . .	27
2.2	Experimental set-up . . . . .	28
2.2.1	Preparation of ultracold calcium . . . . .	28
2.2.2	Laser systems . . . . .	30
2.2.3	Trap frequencies $\omega_{1,2,3}$ . . . . .	37
2.2.4	Intensity of photoassociation laser . . . . .	39
2.3	High power photoassociation . . . . .	41
2.3.1	Measurement of the power broadened PA lines . . . . .	43
2.3.2	Full width at half maximum (FWHM) of the measured PA lines	43
2.3.3	Results from Voigt fits . . . . .	46
2.3.4	Inelastic collision rate coefficient $K_{\text{in}}$ . . . . .	50
2.3.5	Spectral line areas . . . . .	53
2.3.6	FWHM and $\beta$ at different temperatures . . . . .	55
2.4	Prospects for large modification of the scattering length $a$ . . . . .	58
<b>3</b>	<b>Two-color photoassociation of ultracold calcium</b>	<b>63</b>
3.1	Theoretical description of two-color photoassociation . . . . .	64
3.2	Measurement of PA lines in $X^1\Sigma_g^+$ of $\text{Ca}_2$ . . . . .	66
3.2.1	Experiment . . . . .	66

3.2.2	Observed PA lines . . . . .	67
3.2.3	Unperturbed binding energies . . . . .	71
3.2.4	Molecular potentials . . . . .	78
3.2.5	Autler Townes Spectroscopy . . . . .	81
3.3	Consequences for BEC creation for different isotopes . . . . .	85
<b>4</b>	<b>Conclusions and outlook</b>	<b>89</b>
	<b>Appendices</b>	<b>91</b>



# Chapter 1

## Introduction

Dilute quantum gases have been the object of an intensive research in the last decades induced by the huge progress in laser cooling and trapping of neutral atoms. They have important applications in ultracold physics e.g. precise measurements by atomic clocks [Mid12, Fal14, Hun14], creation of new degenerate states like Bose-Einstein condensates (BEC) [Zwi03, Kra09, Ste09] and Bardeen-Cooper-Schrieffer superfluids [Sch08, Lim08] as well as creation of the ultracold ensembles of molecules [Com00, Reg03, Jon06], investigation of the scattering properties at ultracold temperatures and its manipulation via optical Feshbach resonances [Ciu05, Eno08, Yam10].

This progress was only conceivable thanks to the pioneering scientific contributions made in the last century. The cooling of atomic ensembles by laser radiation was proposed by Hänsch and Schawlow [Hän75] in the 1970's to reduce the atomic velocity by scattering with the laser light. Ten years later this cooling technique was successfully implemented by [Ert85, Pro85] for the deceleration of atoms and building of a three-dimensional viscous confinement via the radiation of counterpropagating laser beams in an optical molasses [Chu85]. Soon afterwards the concept of three dimensional trapping was combined with a magnetic field gradient [Raa87] in a so-called magneto-optical trap enabling the cooling of atomic ensembles to less than a millikelvin temperature with densities over  $10^{11} \text{ cm}^{-3}$ . The sub-Doppler cooling in a dark magneto-optical trap and by Sisyphus cooling subsequently improved the efficiency of laser cooling. These cooling and trapping laser techniques have been established nowadays and can be found in every laboratory working with ultracold gases. They opened a new realm for physics of ultracold quantum gases.

The earlier experiments were mostly performed with alkali atoms due to the availability of suitable lasers and due to the use of magnetic traps for evaporative cooling benefiting from the magnetic moment of the ground state of the alkali atoms [Wil95].

As more efficient and advanced lasers were developed the perspectives for research of the

alkaline-earth metals opened. The spin-forbidden intercombination  $^1S_0$ - $^3P_1$  transition is extremely narrow and allows to attain extremely low temperatures by laser cooling. However, the resulting force effected through the spontaneous decay rate of  $^3P_1$  state of  $^{40}\text{Ca}$  with 374 Hz is not large enough to support the atoms against the gravity. To solve this the quench cooling [Bin01a, Meh03] was developed whereby the lifetime of the metastable state is decreased by driving an additional transition to higher lying states that can quickly decay to the ground state again. The subsequent evaporation in an optical dipole trap finally allows one to achieve  $\mu\text{K}$  temperature and below. Nowadays the alkaline-earth atoms enjoy high scientific attention benefiting from their simple electronic structure. Alkaline-earth atoms are suitable for the investigation of the atomic and molecular physics with high accuracy [Por06, McG15c, McG15a] and for theoretical models of divalent-atom dimers. Some bosonic isotopes have no nuclear spin that simplifies the investigation of atomic and molecular collisions [Mac01, Der03, San03] at ultracold temperatures, which strongly depend on the long-range part of the interaction potential.

Their narrow intercombination transitions  $^1S_0$ - $^3P_1$  are widely used in several applications as metrological frequency standards [Mar04, Sch05, Fal14, Vog16], in geodesy for precise measurements [Lis16] or for fundamental research [Chi85, Swa11, Yan13b].

A promising application of the spin-forbidden transitions is its implementation for the control of the interaction in the atomic cloud. For alkali atoms the manipulation is already used routinely by the techniques based on the magnetic Feshbach resonances (MFR), where a molecular bound state is shifted by an external magnetic field to the continuum. At a resonance the scattering length is strongly depending on the magnetic field, which strongly influences the scattering between the atoms. At an appropriate magnetic field the scattering can even vanish. The MFR is established as a robust powerful technique to modify the scattering at ultracold temperatures e.g. to evaporate chromium atoms to a BEC [Gri05]. Unfortunately the MFR technique can not be used for the bosonic alkaline-earth atoms due to the absence of the magnetic moment in ground state.

Alternatively, the scattering and bound states of the alkaline-earth atoms can be optically coupled by a resonant laser light field leading to a so-called optical Feshbach Resonance (OFR) proposed first by [Fed96]. Here, a photoassociation resonance of the bound levels of electronically excited molecules is used instead of a magnetic hyperfine states. If the frequency of the laser light is close to such a resonance the atoms start to interact by virtual radiative transitions capable of inducing significant changes in the

scattering length.

The first OFR were observed in sodium [Fat00] and later in ytterbium [Eno08], always accompanied by huge photoassociative losses. According to the theory of photoassociation [Ciu05] the losses are inversely proportional to the square of the detuning, whereas the change of the scattering length varies only inversely to the detuning. Hence, with narrow photoassociation (PA) lines a large change in the scattering length at relative small detuning from a resonance can be achieved without producing large photoassociative losses. The intercombination lines of alkaline-earth atoms with narrow natural linewidth therefore provide good prerequisites for application of low-loss optical Feshbach resonances, especially near the intercombination transition  $^3P_1 - ^1S_0$  of  $^{40}\text{Ca}$  with a linewidth of 374 Hz, which is about 20 times narrower than the previously studied intercombination transition in  $^{88}\text{Sr}$ .

OFR have a several advantages compared to MFR. The laser light toggles the interaction much faster than magnetic field and can be focused on a small area inside an atomic cloud inducing a local change of the scattering length. For example, they can be also used for the excitation of solitons inside a BEC. Unlike MFR, where the scattering length is a function of the magnetic field  $B$ , the intensity and detuning in OFR application can be separately adjusted opening more technical possibilities for a multitude of possible realizations.

The main goals of this thesis are to explore the practical feasibility of OFR in  $^{40}\text{Ca}$  and to prove the validity of the resonant scattering theory for the description of OFR. To understand to which extent OFR are useful in calcium one needs the full knowledge of the scattering states in the ground potential and the bound molecular states in an excited potential. Six weakly bound molecular states of  $^{40}\text{Ca}$  were already measured [Kah14b] employing the one-color photoassociation spectroscopy (PAS). Using measured binding energies the long-range dispersion coefficients of the molecular excited potentials  $(a, c)1_u$  and  $c0_u^+$  near the  $^3P_1 + ^1S_0$  asymptote and the Frank-Condon density needed for calculation of the excitation rates were derived. The theory used a coupled channel model including spin-orbit coupling and rotational interaction.

The one-color PAS itself is based on the PA process, where two ground-state atoms and a photon form a molecule in an electronically excited state. The deexcitation of the excited molecule results in two atoms with high enough kinetic energies to leave the dipole trap which leads to a loss of the trapped atoms. PAS is sensitive to the bound long-range vibrational states, where the involved atoms stay at large internuclear distances. The scattering between the atoms is also connected to the comparatively large

internuclear separation at which these processes are relevant. Therefore PAS is suitable for investigation both of the intrinsic properties of the constituent atoms and of the macroscopic interaction of dilute gases. Combined with the available ultra-stable lasers developed at the Physikalisch-Technische Bundesanstalt (PTB) the determination of these properties is possible with extremely high precision.

In a first attempt PA resonances [Kah14b] are performed to describe OFR by resonant scattering theory. At low laser intensities the interaction Hamiltonian of light scales linearly with the vector potential and thus can be solved by the perturbation theory with first order correction. However the high intensity PA poses a challenge for the theoretical description. The analysis of the measured spectral lines indicated discrepancies between theory and experiment, especially the calculated linewidths and stimulated rates differed from the measured ones. In particular the measured large linewidths at high laser intensity could not be explained by the theory.

In the first part of this work the high intensity photoassociation is intensively discussed to clarify this open question. Experiments of two molecular PA resonances to different excited molecular potentials  $c0_u^+$  and  $(a, c)1_u$  performed focusing an high laser intensity are presented. The measured spectral line shapes and photoassociative losses were analysed in detail in Sect. 2.3 *High power photoassociation* from the point of view of the currently established resonant scattering theory developed by Bohn and Julienne [Boh99]. This data set leads to a better description of the molecular excited state as a necessary precondition of the application OFR.

In the Sect. 2.4 *Prospects for large modification of the scattering length* the predictions of the feasibility of low loss optical Feshbach resonance for the technical application are presented.

The knowledge of the ground potential is also important for realization of low loss OFR. In the previous experiments performed on  $^{40}\text{Ca}$  [All02, All03] a big data set of the rovibrational levels of the inner part of the ground state potential  $X^1\Sigma_g^+$  was collected, where the outer classical turning point of the last measured level is located at internuclear separation of  $R \leq 2$  nm. Until the present time the binding energy belonging to the long range part of the potential with the outer classical turning points at  $R > 2$  nm were not measured. In the second part of this work the measurement of the weakest molecular levels of the calcium dimer  $\text{Ca}_2$  in the ground state with the outer classical turning point at above 2 nm is presented. On this basis the complete description of the ground state potential  $X^1\Sigma_g^+$  was possible. This allows a more precise determination of the long-range dispersion coefficients  $C_6$ ,  $C_8$  and  $C_{10}$  describing the

dipole-dipole, dipole-quadrupole and quadrupole-quadrupole interactions, respectively. As a result, the determination of the s-wave scattering length was largely improved and allows the correct calculation of the scattering states needed for OFR.

The measurement of weak rovibrational levels of  $^{40}\text{Ca}$  in the molecular ground state demands lasers with linewidth of less than 1 kHz to resolve the spectral lines. Especially for the weakest bound state, which is lying with 1.6 MHz very close to the atomic asymptote  $^1S_0 + ^1S_0$ , use of such laser is necessary to avoid undesirable losses. In the Sect. 2.2 *Experimental set-up* the current laser system is described. The spectral lines of molecular ground state are measured by two-color PA spectroscopy in Raman configuration, where a set up of two lasers with highly stable frequencies is required. The laser driving between the scattering states in continuum and the excited bound molecular state is set to be far detuned from the intermediate bound molecular state, inducing a weak coupling of the scattering states to the intermediate bound molecular state. The second laser connects this intermediate state to a bound molecular level in the ground state. Photoassociative losses are observed when the frequency difference of the lasers is close to resonance of the ground molecular state. In the Sect. 3.2 *Measurement of PA lines in  $X^1\Sigma_g^+$  of  $\text{Ca}_2$*  the details of the measurement are presented. The analysis of the dispersion coefficients of the  $X^1\Sigma_g^+$  ground state potential showed the importance of a retardation effect at long range described in Sect. 3.2.4 *Molecular potentials*.

The Sect. 3.2.5 *Autler-Townes splitting* comprises the measurement of the PA resonances in Autler-Townes configuration, where unlike Raman configuration the second laser being resonant to the bound-bound transition between the excited and ground state forms dressed states, which are probed by the free-bound laser. Additionally the determination of the corresponding bound-bound transition matrix element is presented. The section also gives an insight into the possibility of the creation of ultracold molecules in the ground state  $X^1\Sigma_g^+$ .

The important results and future applications are summarized in Chap. 4 *Conclusions and outlook*.



## Chapter 2

# Towards low-loss optical Feshbach resonances

Photoassociation (PA) is a process, where two ground-state atoms absorb a photon to form a molecule in an electronically excited state. Based on this process, PA spectroscopy allows determination of various characteristics of atoms and molecules such as atomic and molecular states [Kah14b, Lis02, Bel12, McG15b], chemical reactions [Ulm12, Jon06], scattering lengths [Kit08, Vog07] and the interaction potentials [All03, Kah14b, Fal08]. Combined with established laser-cooling techniques the measurements are performed with very high spectral resolution at ultracold temperatures of as low as hundred nano Kelvin [McK02, Jun08]. At the moment the control of the scattering properties via Feshbach resonances are one of the hot applications of the photoassociation [Yan13a, Nic15, Jun08].

The strongly spin-forbidden transitions of the calcium dimer to the  $^3P_1+^1S_0$  asymptote are a promising research systems for investigation of the OFR due to their extreme small spontaneous natural decay rate  $2\pi \cdot 374 \text{ s}^{-1}$  and due to absence of a magnetic moment in the ground state.

## 2.1 One-color photoassociation spectroscopy

### 2.1.1 Photoassociation

The photoassociation is well described by resonant scattering theory where according to the dressed-state picture the bound state is embedded by the coupled resonant light in the continuum formed by the scattering ground states [Fan61, Tho87]. The presence of the light-field coupling influences the scattering between the atoms and allows the selective modification by tuning the laser frequency.

The subsequent considerations regarding photoassociation are applied to the excited bound molecular states to  $^3P_1+^1S_0$  measured by [Kah14b, App13]

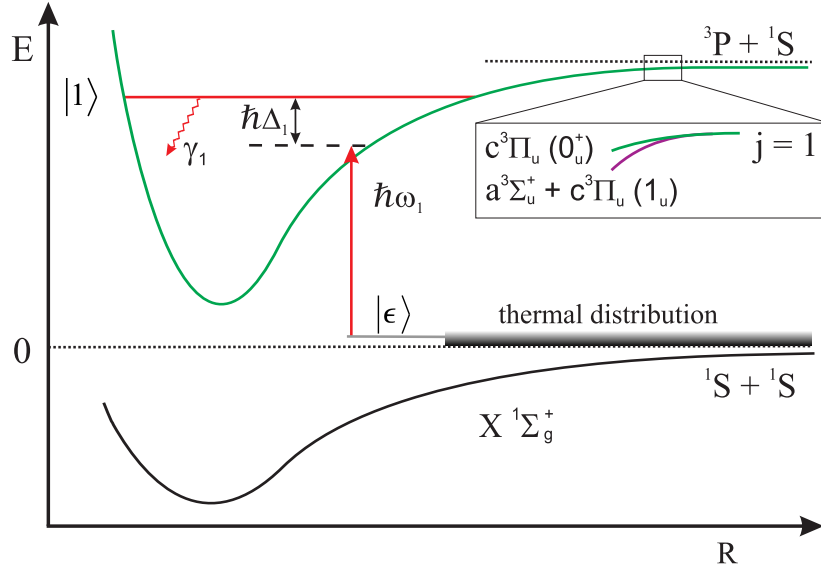


Figure 2.1: Scheme of photoassociation for  $\text{Ca}_2$  near the the  ${}^3P_1+{}^1S_0$  asymptote ( $\lambda = 657 \text{ nm}$ ) coupled by a near resonant light

The scheme of the photoassociation process is shown in Fig. 2.1. The black and green lines indicate the ground state potential in dependency of the internuclear distance  $R$ , correlating to the asymptote  ${}^1S_0 + {}^1S_0$  and excited state potential correlating to the asymptote  ${}^3P_1+{}^1S_0$ , respectively. Near the  ${}^3P_1+{}^1S_0$  asymptote the spin-orbit interaction becomes dominant and the adiabatic potentials are more accurately described by Hund's case (c) potentials  $c0_u^+$  and  $(a, c)1_u$  being a strong mixture of the two case (a) states (Fig. 2.1). The laser with frequency  $\omega_1$  couples one of scattering states  $|\epsilon\rangle$  from the thermal cloud to the molecular resonance  $|1\rangle$  detuned by  $\Delta_1$ . Total  $\gamma_1 = \gamma_{\text{mol}} + \Gamma$  indicates the decay rate of the molecular state  $|1\rangle$ , where  $\gamma_{\text{mol}}$  is the natural spontaneous decay rate and  $\Gamma$  contains additional effects leading to decay of the bound state<sup>1</sup>.

At ultracold temperatures the collisions between the calcium bosons are dominated by s-wave scattering with the scattering cross section [Ing98]

$$\sigma_{\text{s-wave}} = 8\pi a_{\text{bg}}^2, \quad (2.1)$$

where  $a_{\text{bg}}$  is the s-wave scattering length without modification. The experiments were performed at ultracold temperature of less  $3 \mu\text{K}$ , thus the calculation can be restricted to only s-wave scattering ( $l = 0$ ). The ground state of  ${}^{40}\text{Ca}$  is spinless, therefore

<sup>1</sup>For low intensity measurements I set  $\Gamma = 0$  in my calculation.



only a single nondegenerate entrance channel needs to be considered. The calculation can be reduced to a single s-wave matrix element  $S_{l,l}(k)$  represented by the complex energy-dependent phase shift  $\eta(k)$  [Qué12]

$$S_{0,0}(k) = e^{2i\eta_0(k)}, \quad (2.2)$$

where  $k = \frac{\sqrt{2\epsilon_{\text{col}}\mu}}{\hbar}$  is the de Broglie wave number and  $\mu$  is the reduced mass of two calcium atoms.

The scattering matrix element  $S_{0,0}(k)$  is related to an energy-dependent scattering length  $\alpha(k)$ , which can be expressed as

$$\alpha(k) = a(k) - ib(k) = -\frac{\tan \eta_0(k)}{k} = \frac{1}{ik} \frac{1 - S_{0,0}(k)}{1 + S_{0,0}(k)}. \quad (2.3)$$

In the limit  $k \rightarrow 0$  and  $k|\alpha| \ll 1$  the inelastic and elastic loss sections for two identical bosons can be derived from  $S_{0,0}(k)$  as

$$\sigma_{\text{el}} = \frac{2\pi}{k^2} |1 - S_{0,0}|^2 = 8\pi |\alpha(k)|^2 \quad (2.4)$$

$$\sigma_{\text{in}} = \frac{2\pi}{k^2} (1 - |S_{0,0}|^2) = \frac{8\pi}{k} b(k) \quad (2.5)$$

The corresponding elastic and inelastic collision rate coefficients can be calculated as

$$K_{\text{el}}(k) = \frac{\hbar k}{\mu} \sigma_{\text{el}} = 8\pi \frac{\hbar}{\mu} k |\alpha(k)|^2 \quad (2.6)$$

$$K_{\text{in}}(k) = \frac{\hbar k}{\mu} \sigma_{\text{in}} = 8\pi \frac{\hbar}{\mu} b(k). \quad (2.7)$$

In calcium the PA resonances of the intercombination lines are clearly separated from one another by more than 100 MHz. Thus a single spectral lines can be approximated as an isolated resonances. Thereby the matrix element  $S_{0,0}(k)$  for the isolated decaying resonance is [Nic15]

$$S_{0,0}(k, \Delta_1) = \left( 1 - \frac{i\hbar\gamma_{\text{stim}}(k)}{\Delta_1 + i\hbar\frac{\gamma_1 + \gamma_{\text{stim}}(k)}{2}} \right) e^{2i\eta_{bg}}, \quad (2.8)$$

where  $\eta_{\text{bg}} = -ka_{\text{bg}}$  for  $k \rightarrow 0$  and  $\gamma_{\text{stim}}(k)$  is the stimulated rate between the energy normalized scattering ground state  $|\epsilon\rangle$  and the excited molecular bound state  $|1\rangle$ . Using Eq. 2.8  $|S_{0,0}|^2$  is determined as

$$|S_{0,0}(k, \Delta_1)|^2 = 1 - \frac{\gamma_{\text{stim}}(k)\gamma_1}{\Delta_1^2 + \frac{(\gamma_{\text{stim}}(k) + \gamma_1)^2}{4}}. \quad (2.9)$$

Substituting Eq. 2.9 into Eq. 2.7 the inelastic coefficient  $K_{\text{in}}$  is

$$K_{\text{in}}(k, \Delta_1) = \frac{2\pi\hbar}{\mu} \frac{\gamma_{\text{stim}}(k)\gamma_1}{\Delta_1^2 + \frac{(\gamma_{\text{stim}}(k) + \gamma_1)^2}{4}}. \quad (2.10)$$

For sufficiently low laser intensity the stimulated rate  $\gamma_{\text{stim}}$  can be estimated by Fermi's golden rule with a harmonic laser interaction  $V_{\text{opt}}^1(R) \cos(\omega_1 t)$ . The optical potential  $V_{\text{opt}}^1(R) = -\mathbf{E}_1 \cdot \mathbf{d}(R)$  is related to the molecular dipole matrix element  $\mathbf{d}(R)$  and the amplitude of electrical field of laser  $\mathbf{E}_1(t) = \vec{E}_1 \cos(\omega_1 t)$  with  $|\vec{E}_1| = \sqrt{\frac{2I_1}{\epsilon_0 c}}$ .

$$\gamma_{\text{stim}}(\epsilon_{\text{col}}, I_1) \approx \frac{\pi}{2\hbar} |\langle 1 | V_{\text{opt}}^1(R) | \epsilon \rangle|^2. \quad (2.11)$$

Assuming  $\mathbf{d}(R)$  is only weak dependent on the internuclear separation  $R$  at long ranging the corresponding matrix element can be expressed based on the atomic transition dipole moment [Tie03]

$$|\langle 1 | \mathbf{d}(R) | \epsilon_{\text{col}} \rangle|^2 = |\langle 1 | \mathbf{d}_{\text{atom}} | \epsilon_2 \rangle|^2 f_{\text{ROT}} f_{\text{FCD}}(\epsilon_{\text{col}}), \quad (2.12)$$

where  $|\langle 1 | \mathbf{d}_{\text{atom}} | \epsilon_2 \rangle|^2$  is the reduced atomic matrix element,  $f_{\text{ROT}}$  contains the Hoenl-London factor combined with the influence of the polarization of the laser light and  $f_{\text{FCD}}(\epsilon_{\text{col}}) = |\langle 1 | \epsilon_{\text{col}} \rangle|^2$  is the Franck-Condon density.

The reduced atomic matrix element itself can be calculated from Einstein coefficient  $A_{\text{atom}}$ , which here is equal to  $\gamma_{\text{atom}}$  for an atomic level with total angular momentum  $j_1, m_1$

$$\gamma_{\text{atom}} = \frac{2\omega_{\text{atom}}^3}{3\epsilon_0 c^3 \hbar} |\langle 1 | \mathbf{d}_{\text{atom}} | 2 \rangle|^2 \quad (2.13)$$

$$= \frac{2\omega_{\text{atom}}^3}{3\epsilon_0 c^3 \hbar} \sum_{q=-1,0,1} \begin{pmatrix} j_1 & 1 & j_2 \\ m_1 & q & -m_1 - q \end{pmatrix}^2 |\langle 1 | \mathbf{d}_{\text{atom}} | 2 \rangle|^2 \quad (2.14)$$

where  $\omega_{\text{atom}}$  is the atomic transition frequency,  $c$  the velocity of light and  $\epsilon_0$  the vacuum permittivity. The sum over the square of the Wigner 3j symbols  $\begin{pmatrix} j_1 & 1 & j_2 \\ m_1 & q & -m_1 - q \end{pmatrix}$  considers the spontaneous atomic decay from the one of the Zeeman levels  $m_1$  over all allowed polarization channels labelled by  $q$ .

In general the sum of the square of the Wigner 3j symbols is

$$\sum_{q=-1,0,1} \begin{pmatrix} j_1 & 1 & j_2 \\ m_1 & q & -m_1 - q \end{pmatrix}^2 = \frac{1}{2j_1 + 1} \quad (2.15)$$

and thus contains the degeneracy factor of the upper state.

The  $f_{\text{FCD}}(\epsilon_{\text{col}})$  were calculated by Prof. Eberhard Tiemann applying the excited state potentials at the asymptote  ${}^3P_1 + {}^1S_0$  determined in previous work [Kah14b]. For this calculation the vibrational levels were represented by a multi-component wave function, which is described most conveniently in Hund's case (e) basis  $|{}^1S_0 + {}^3P_j, l, J\rangle$ . The first part of the basis vector describes the relevant atom pair asymptote with the total atomic angular momentum  $j$ ,  $l$  is the angular momentum of the pair rotation and  $J$  is the total angular momentum. The starting level in the present experiment is always the s-wave continuum, corresponding to  $J_\epsilon = 0$  with parity "+", only the excited levels  $J_1 = 1$  with parity "-" have to be considered. This results in only three possible basis states

$$|{}^1S_0 + {}^3P_1, 0, 1\rangle, \quad (2.16)$$

$$|{}^1S_0 + {}^3P_1, 2, 1\rangle, \quad (2.17)$$

$$\text{and } |{}^1S_0 + {}^3P_2, 2, 1\rangle. \quad (2.18)$$

Because of the electric dipole selection rule  $\Delta l = 0$  only the component  $|{}^1S_0 + {}^3P_1, 0, 1\rangle$  was needed for the calculation of the Franck-Condon densities with the continuum  $|{}^1S_0 + {}^1S_0, 0, 0\rangle$ . The Franck-Condon density  $f_{\text{FCD}}(\epsilon_{\text{col}})$  were determined as the square of the overlap-integral between the eigenfunction of the molecular state in the upper excited potential and the scattering function of the colliding atoms in a ground state with relative kinetic energy  $\epsilon_{\text{col}}$ . The wave functions are calculated with the Numerov method [Mes11].

In Fig. 2.2 the  $f_{\text{ROT}} \cdot f_{\text{FCD}}(\epsilon_{\text{col}})$  in dependency of the collision energy scaled with  $\mu\text{K}$  are shown.<sup>2</sup> The Tab. 2.1 lists the values for a collision energy  $\epsilon_{\text{col}} = k_{\text{B}} \cdot 1 \mu\text{K}$ .

---

<sup>2</sup>The values are 6 times larger than in [Kah14a]. The difference arises from a new evaluation of the rotational factors  $f_{\text{ROT}}$ .

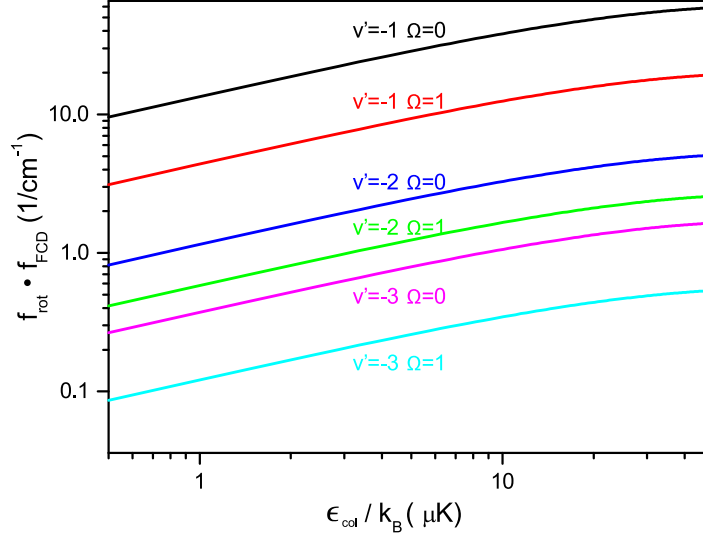


Figure 2.2:  $f_{\text{ROT}} \cdot f_{\text{FCD}}(\epsilon_{\text{col}})$  calculated for  $J_\epsilon = 0$ ,  $m_\epsilon = 0$  to  $J_1 = 1$ ,  $m_1 = 0$  of transition  $^1S_0$ - $^3P_1$  using coupled channel model for the s-wave scattering ( $l = 0$ ). Courtesy of E. Tiemann.

Assuming

$$\gamma_{\text{mol}} = 2\gamma_{\text{atom}} \quad (2.19)$$

the rotational factor is calculated as [Edm57] (Eq. 7.1.7)

$$f_{\text{ROT}} = (2J_1 + 1)(2J_\epsilon + 1) \left\{ \begin{matrix} j_1 & J_1 & l \\ J_\epsilon & j_2 & 1 \end{matrix} \right\}^2 \left( \begin{matrix} J_1 & 1 & J_\epsilon \\ -m_1 & q & -m_\epsilon \end{matrix} \right)^2 \cdot 2 \cdot (2j_1 + 1) \quad (2.20)$$

where the Wigner 6j symbol  $\left\{ \right\}$  contains the coupling of the atomic and molecular angular momenta, Wigner 3j symbol  $\left( \right)$  contains the polarisation dependency, the factor 2 originates from Eq. 2.19 and last factor is the degeneracy factor from Eq. 2.15. Thus one obtains

$$\gamma_{\text{stim}}(\epsilon_{\text{col}}, I_1) = \gamma_{\text{atom}} \frac{3}{8\pi} \frac{I_1 \lambda_{\text{atom}}^3}{c} f_{\text{ROT}} f_{\text{FCD}}(\epsilon_{\text{col}}), \quad (2.21)$$

where  $\gamma_{\text{atom}} = 2\pi \cdot 374 \text{ s}^{-1}$  is spontaneous atomic decay rate,  $\lambda_{\text{atom}} = 657 \text{ nm}$  atomic wave length of the used PA  $^1S_0$ - $^3P_1$  transition.

state	$f_{\text{ROT}} \cdot f_{\text{FCD}}(\epsilon_{\text{col}})$ ( $1/\text{cm}^{-1}$ )
$v' = -1, \Omega = 0$	13.35
$v' = -1, \Omega = 1$	4.34
$v' = -2, \Omega = 0$	1.15
$v' = -2, \Omega = 1$	0.58
$v' = -3, \Omega = 0$	0.38
$v' = -3, \Omega = 1$	0.12

Table 2.1: Estimated  $f_{\text{ROT}} \cdot f_{\text{FCD}}(\epsilon_{\text{col}})$  for a collision energy  $\epsilon_{\text{col}}/k_B = 1 \mu\text{K}$  for several excited molecular states in the potentials  $c0_u^+$  and  $(a, c)1_u$

### 2.1.2 Optical length $l_{\text{opt}}$

According to the Wigner threshold law  $f_{\text{FCD}} \propto k \propto \sqrt{\epsilon_{\text{col}}}$  at ultracold temperatures, the quantity  $\frac{\hbar\gamma_{\text{stim}}(k)}{2k} = l \cdot E_{\text{ref}}$  is independent of the wave number  $k$  with a reference energy  $E_{\text{ref}}$  [Nic15]. Therefore it is useful to define a parameter optical length  $l_{\text{opt}}$  by choosing  $E_{\text{ref}} = \hbar\gamma_1$ :

$$l_{\text{opt}} := \frac{\gamma_{\text{stim}}}{2k\gamma_{\text{mol}}} = \frac{3\lambda^3 f_{\text{ROT}} f_{\text{FCD}}(\epsilon_{\text{col}})}{16\pi ck} I. \quad (2.22)$$

The optical length  $l_{\text{opt}}$  is independent from  $k$  and thus constant for collision energies  $\epsilon_{\text{col}}$  at ultracold temperatures. It is proportional to the intensity of the PA laser, thus it is a good quantity to describe the coupling of the free-bound transition and is often used in the description of optical Feshbach resonances.

Consequently the stimulated rate can be expressed as

$$\gamma_{\text{stim}}(\epsilon_{\text{col}}) = 2l_{\text{opt}}k(\epsilon_{\text{col}})\gamma_1. \quad (2.23)$$

In the Tab. 2.2 the calculated  $\gamma_{\text{stim}}$  and  $l_{\text{opt}}$  are listed for two different intensities  $I_1$  using  $f_{\text{ROT}} \cdot f_{\text{FCD}}(\epsilon_{\text{col}}/k_B = 1 \mu\text{K}) = 13.35 \text{ 1/cm}^{-1}$  for  $v'$  in  $c0_u^+$ .

### 2.1.3 Losses and inelastic collision rate coefficient $K_{\text{in}}$

The photoassociative losses induced by decaying excited molecules are correlated to an inelastic collision rate coefficient  $K_{\text{in}}$ . The corresponding rate equation is

$I_1$ (W/cm <sup>2</sup> )	$l_{\text{opt}}$ (x10 <sup>3</sup> a <sub>0</sub> )	$\gamma_{\text{stim}}$ (kHz)
1	0.4	0.4
560	221	225

Table 2.2: Calculated  $\gamma_{\text{stim}}(\epsilon_{\text{col}})$  and  $l_{\text{opt}}$  for collision energies  $\epsilon_{\text{col}}/k_{\text{B}} = 1 \mu\text{K}$  according to Eq. 2.22 and 2.21 for two different  $I_1$

$$\dot{\rho}(t) = -2K_{\text{in}}\rho^2(t), \quad (2.24)$$

where  $\rho$  is a local density and  $K_{\text{in}}$  obtained from Eq. 2.10.

For the observed line shapes the inelastic loss coefficient is given by the thermally averaged value of the scattering matrix element over a distribution of relative velocities. Thus the complete losses of the PA resonance can be described as [Nap94, Boh96, Boh99]:

$$\langle K_{\text{in}}(l, T, \Delta_1, I_1) \rangle_{\text{T}} = \left\langle \frac{\pi v}{k^2} \sum_{l=0}^{\infty} (2l+1) |S_{0,0}(k, l, \Delta_1, I_1)| \right\rangle_{\text{T}} \quad (2.25)$$

where  $\langle \rangle_{\text{T}}$  is thermal average.

For s-wave scattering the inelastic ( $l = 0$ ) loss coefficient can be expressed by substituting the scattering matrix element Eq. 2.9 with  $\epsilon_{\text{col}} = \frac{k^2 \hbar^2}{2\mu}$  into Eq. 2.25

$$\begin{aligned} & \langle K_{\text{in}}(T, \Delta_1, l_{\text{opt}}) \rangle_{\text{T}} \\ &= \frac{1}{h Q_T} \int_0^{+\infty} \frac{\gamma_1 \gamma_{\text{stim}}(\epsilon_{\text{col}})}{(\Delta_1 - \epsilon - \delta_{\text{div}})^2 + \left( \frac{\gamma_1 + \gamma_{\text{stim}}(\epsilon_{\text{col}})}{2} \right)^2} \exp\left(-\frac{\epsilon_{\text{col}}}{k_{\text{B}}T}\right) d\epsilon_{\text{col}} \quad (2.26) \\ &= \frac{1}{h Q_T} \int_0^{\infty} \frac{2l_{\text{opt}} \frac{\sqrt{2\mu\epsilon_{\text{col}}}}{\hbar} \gamma_{\text{mol}} \gamma_1}{(\Delta_1 - \epsilon - \delta_{\text{div}}(I_1))^2 + \left( \gamma_1 + 2l_{\text{opt}} \frac{\sqrt{2\mu\epsilon_{\text{col}}}}{\hbar} \gamma_{\text{mol}} \right)^2 / 4} \exp\left(-\frac{\epsilon_{\text{col}}}{k_{\text{B}}T}\right) d\epsilon_{\text{col}} \quad (2.27) \end{aligned}$$

with the translational partition function  $Q_{\text{T}} = \left( \frac{2\pi\mu k_{\text{B}}T}{h^2} \right)^{3/2}$  and  $\delta_{\text{div}}(I_1)$  includes shifts of the PA laser.

### 2.1.4 Spectral line shape

The loss processes in a optical trap can be well described by a rate equation

$$\dot{N}(t) = -\alpha N - \beta N^2 - \gamma N^3 + \dot{N}_{DT}(t) \quad (2.28)$$

where the atomic loss coefficient  $\alpha$  corresponds to the scattering with the background atoms,  $\beta$  is the two-body loss rate coefficient and  $\gamma$  is the three-body loss rate coefficient and  $\dot{N}(t)$  is the additional term containing the internal trap dynamics.

The relative importance of the PA losses in our set-up is discussed in detail in earlier publications [Kah14a, App13]. They find the PA losses are dominated by the two-body losses and the other processes can be neglected even for a relative short irradiation pulse of less 200 ms. Therefore Eq. 2.28 of a trap can be simplified to

$$\dot{N}(t) = -\beta N^2(t) \quad (2.29)$$

with its solution

$$N(\Delta_1) = \frac{N_0}{1 + N_0 \tau \beta (\Delta_1)} \quad (2.30)$$

where  $N_0$  is the initial atom number,  $\tau$  duration of the irradiation and  $\Delta_1$  is the detuning from the PA resonance. The two-body loss coefficient  $\beta$  is independent of the atom number and irradiation duration, and is related to the atom inelastic collision rate coefficient  $K_{\text{in}}$ .

The conversion  $\beta$  to  $K_{\text{in}}$  is achieved by integration over trap volume  $V_{\text{DT}}$

$$\dot{N}(t) = \int_{V_{\text{DT}}} \rho(\dot{\mathbf{r}}) d^3 \dot{\mathbf{r}} \quad (2.31)$$

$$= - \int_{V_{\text{DT}}} 2 \langle K_{\text{in}} \rangle_{\text{T}} \rho(\mathbf{r})^2 d^3 \mathbf{r} = -\beta N^2(t) \quad (2.32)$$

The trap potential in the region of the atomic cloud can be approximated by a harmonic potential

$$U(\mathbf{r}) = \frac{1}{2} m \sum_i^{x,y,z} \omega_i^2 i^2 \quad (2.33)$$

with the characteristic frequencies  $\omega_{x,y,z}$  for calcium atoms with a mass  $m$ . During the PA irradiation the thermal equilibrium at constant temperature is assumed. The atomic density distribution in thermal equilibrium is Gaussian<sup>3</sup>

$$\rho(x, y, z) = \rho_0 \exp\left(-\frac{x^2}{2\sigma_x^2} - \frac{y^2}{2\sigma_y^2} - \frac{z^2}{2\sigma_z^2}\right) \quad (2.34)$$

where  $\sigma_{x,y,z} = \sqrt{\frac{k_B T}{m \omega_{x,y,z}^2}}$  with trap frequencies  $\omega_{x,y,z}$ .

After integration over the trap volume the atom number is

$$N(t) = \rho(t) \sqrt{2\pi}^3 \sigma_x \sigma_y \sigma_z. \quad (2.35)$$

Solving Eq. 2.32 with Eq. 2.35 one obtains the relationship between inelastic collision rate coefficient  $K_{\text{in}}$  and two-body loss rate  $\beta$  coefficients

$$\beta = 2 \langle K_{\text{in}} \rangle_{\text{T}} \frac{1}{\sqrt{4\pi}^3 \sigma_x \sigma_y \sigma_z} \quad (2.36)$$

and can be reduced to

$$\langle K_{\text{in}} \rangle_{\text{T}} = \frac{\sqrt{8}}{2} V_{\text{DT}} \beta \quad (2.37)$$

where

$$V_{\text{DT}} = \frac{1}{\omega_x \omega_y \omega_z} \left( \frac{2\pi k_B T}{m} \right)^{3/2} \quad (2.38)$$

is the trap volume.

### 2.1.5 Inhomogeneous Doppler broadening of the measured spectral lines

The relevant broadening mechanism for the one-color PA measurements is the Doppler broadening. It results from the shifted photon energy in the moving frame of the center-of-mass coordinates. The resulting line shape is the convolution of a Gaussian

---

<sup>3</sup>Applicability of the Gaussian distribution was affirmed by time-of-flight measurements.



with a temperature dependent width and of the Lorentzian of the PA line shape in Eq. 2.10. Considering the Doppler effect the thermal averaged one-color PA line shape can be expressed averaged over relative velocities of the atoms (cf. [Mes99, Ciu04, Nic15]):

$$\langle K_{\text{in}}^{\text{D}}(T, \Delta_1, l_{\text{opt}}) \rangle_{\text{T}} = \int_{-\infty}^{+\infty} dv_z \frac{1}{\sqrt{\pi} v_{\text{mp}}} \cdot e^{-\frac{v_z^2}{v_{\text{mp}}^2}} \cdot \langle K_{\text{in}}(T, \Delta_1 + k_{\text{las}} v_z, l_{\text{opt}}) \rangle_{\text{T}} \quad (2.39)$$

where  $v_{\text{mp}} = \sqrt{2k_{\text{B}}T/(2m_{40\text{Ca}})}$  is the most probable speed and

$$\Gamma_{\text{D}} = \frac{2\pi}{\lambda} \sqrt{\frac{k_{\text{B}}T}{2m_{40\text{Ca}}}} \sqrt{8 \ln(2)} \quad (2.40)$$

is the Doppler FWHM in 1/s.

It is useful to express Eq. 2.39 in the frequency domain

$$\langle K_{\text{in}}^{\text{D}}(T, \Delta_1, l_{\text{opt}}) \rangle_{\text{T}} = \int_{-\infty}^{+\infty} d\nu_z \frac{2\sqrt{\ln(2)}}{\sqrt{\pi}\Gamma_{\text{D}}} \cdot e^{-4\ln(2)\frac{\nu_z^2}{\Gamma_{\text{D}}^2}} \cdot \langle K_{\text{in}}(T, \Delta_1 + \nu_z, l_{\text{opt}}) \rangle_{\text{T}} \quad (2.41)$$

The individual spectral lines of this PA line are called Voigt profiles. The area of the Voigt profile with normalized Gaussian distribution does not change for different Gaussian widths and is scaled with the area of the Lorentzian. This was used during the analysis of the observed PA areas.

$\beta$  can be calculated from Eq. 2.37

$$\langle \beta^{\text{D}}(T, \Delta_1, l_{\text{opt}}) \rangle_{\text{T}} = \frac{2}{\sqrt{8}V_{\text{DT}}} \langle K_{\text{in}}^{\text{D}}(T, \Delta_1, l_{\text{opt}}) \rangle_{\text{T}}. \quad (2.42)$$

The Eq. 2.42 was used for all further theoretical simulation of the one-color photoassociation spectra.

### 2.1.6 Scattering length $a$

As already mentioned above the photoassociation can be interpreted as using an optical Feshbach resonance, where the scattering length is varied by the coupling through resonant light. From the energy-dependent scattering length  $\alpha(k)$  Eq. 2.3 and the scattering matrix element  $S_{0,0}$  (Eq. 2.8) the real part of  $\alpha(k)$  can be derived. This

$\text{Re}(\alpha(k))$  is corresponding to the usual scattering length  $a$  (cf. [Fed96, Boh97, Ciu05, Qué12]).

In the limit  $k \rightarrow 0$  the scattering length  $a$  can be expressed as

$$a = a_{\text{bg}} + a_{\text{opt}}(\Delta_1, l_{\text{opt}}, \epsilon_{\text{col}}) = a_{\text{bg}} + \frac{l_{\text{opt}} \gamma_1 \Delta_1}{\Delta_1^2 + \frac{(\gamma_1 + \gamma_{\text{stim}}(\epsilon_{\text{col}}))^2}{4}}. \quad (2.43)$$

The scattering length  $a$  in the presence of laser light is not constant but instead depends on the atomic properties and laser parameters. It is even possible to change the sign of scattering length [Fed96] by choosing suitable parameters. Fig. 2.3 shows qualitatively the variation of the scattering length  $a$  and the atomic loss coefficient induced by a resonant light field detuned by  $\Delta_1$  with respect to a PA resonance.

On resonance the contribution due the Feshbach resonance on the scattering length is zero and depending on the detuning - red or blue - the sign is negative or positive.

Additionally the scattering length can be separately changed by the detuning and by the intensity of the laser. Since the  $a_{\text{opt}}$  linearly depends on the intensity of the laser light, it can be easily modified. The biggest contribution occurs at the detuning  $\Delta_1 = \frac{\gamma_1 + \gamma_{\text{stim}}(\epsilon_{\text{col}})}{2}$ .

Compared to magnetic Feshbach resonances, where the strength and the detuning are coupled by the magnetic field, the independent variation of the intensity and detuning for the optical Feshbach resonances offers significant benefits for the scientific applications.

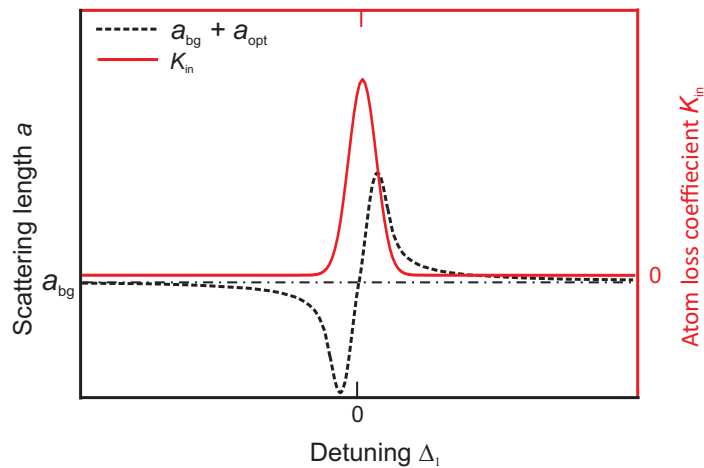


Figure 2.3: Scattering length  $a$  as a sum of the background  $a_{\text{bg}}$  and optically induced  $a_{\text{opt}}$  scattering lengths and the atom loss coefficient  $K_{\text{in}}$  vary in dependency of the detuning  $\Delta_1$  of the PA resonant laser light.

### 2.1.7 Classification of Ca resonance strength of $^1S_0$ - $^3P_1$

The theoretical description [Fed96, Boh99] of OFR and MFR show strong similarity thus by using the resonance length formalism it is possible to compare its strength by a dimensionless resonance pole strength parameter  $s_{\text{res}}$ . According to [Chi10] the strength of the optical Feshbach resonances can be classified by

$$s_{\text{res}}^{\text{OFR}} = \frac{l_{\text{opt}} \hbar \gamma_1}{\bar{a} \bar{E}}, \quad (2.44)$$

where  $\bar{a} = \frac{4\pi}{\Gamma^2(1/4)} R_{\text{vdW}}$  is mean scattering length and  $\bar{E} = \frac{\hbar^2}{2\mu\bar{a}^2}$  is the corresponding energy of the van der Waals potential with  $\Gamma$  being the gamma function and  $R_{\text{vdW}} = \frac{1}{2} \left( \frac{2\mu C_6}{\hbar^2} \right)^{1/4}$  containing the dispersion coefficient  $C_6$ . If  $s_{\text{res}}^{\text{OFR}} > 1$  the resonance is called *broad* or *open-channel dominated*. Here the bound state and scattering states have properties of the entrance channel over the large detuning range  $\Delta_1$ , therefore the scattering resonance is broad. The resonance is called *narrow* or *closed-channel dominated*, when the bound state and scattering states have the same properties of the entrance channel only over the small fraction of the width  $\gamma_1$ . In general the *broad* and *narrow* resonances label the resonances, which can or cannot be modelled by single channel model [Chi10]. In the experiments, where MFR prove beneficial, a pole strength parameter is between 1 and 100.

The ratio at the  $^3P_1 - ^1S_0$  transition of calcium with  $R_{\text{vdW}} = 56.4 a_0$  and  $\bar{E} = 24.4$  MHz

$$\frac{\hbar \gamma_1}{\bar{E}} \approx 2.4 \cdot 10^{-5} \quad (2.45)$$

indicates the strong character of the narrow OFR. To bring the system in the regime comparable to the useful MFR the strength parameter  $s_{\text{res}}^{\text{OFR}} > 1$  the laser intensity has to be dramatically increased. A laser intensity of  $5 \cdot 10^3 \text{ Wcm}^{-2}$  applied to the molecular bound state  $v' = -1$  of molecular potential  $c0_u^+$  will induce an optical length of more than  $2.2 \cdot 10^6 a_0$  which corresponds to  $s_{\text{res}}^{\text{OFR}} \approx 1$ . The experiments including the alkaline-earth metals with  $s_{\text{res}}^{\text{OFR}} > 1$  are not performed yet and are a new research field. The high power measurements described in Chap. 2.3 with the strength parameter  $s_{\text{res}}^{\text{OFR}} \approx 0.1$  are close to this new regime.

## 2.2 Experimental set-up

### 2.2.1 Preparation of ultracold calcium

The experiment is carried out in an ultrahigh vacuum (UHV) chamber with a typical pressure of  $2 \times 10^{-10}$  mbar. The oven section is connected to the main chamber through a differential pumping stage [Naz07]. The oven is filled with metallic calcium and usually operating at temperature of 570-600 °C.

A cloud of the ultracold  $^{40}\text{Ca}$  is prepared in UHV employing the established laser cooling and trapping methods by four different groups of the laser frequencies.

The broad singlet  $^1S_0 - ^1P_1$  transition resonant to the 423 nm laser is used for decelerating by a Zeeman-slower and deflecting by a 2D molasses system to the center of a magneto-optical trap (MOT) as shown in Fig. 2.4.

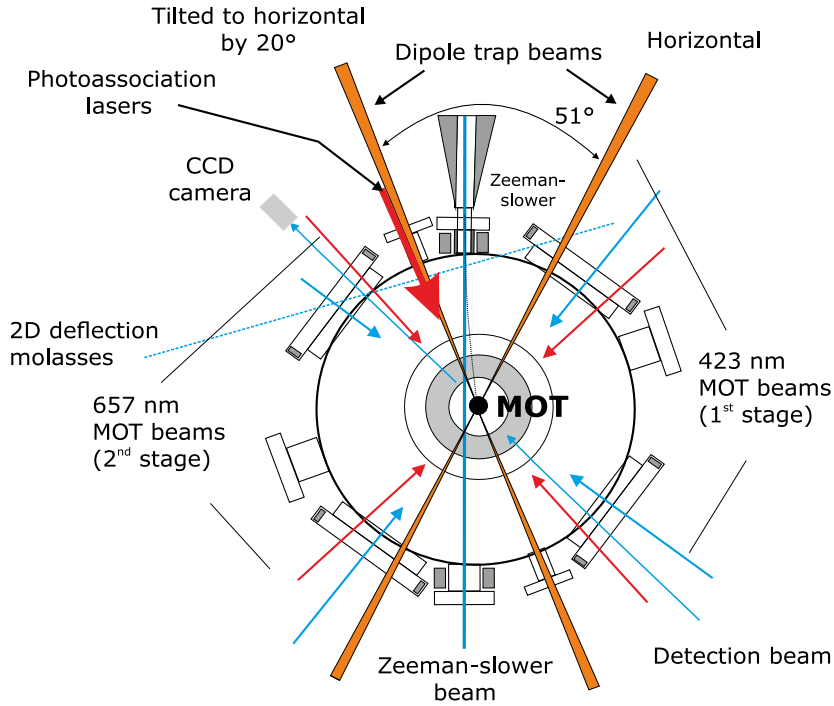


Figure 2.4: Scheme of vacuum chamber with relevant laser beams and peripheral devices

The slow atoms are trapped and cooled down to the ultracold temperature regime in two subsequent stages (see Fig. 2.5).

In the first stage the blue MOT operated by the same 423 nm laser is accompanied by a laser at 672 nm, the so-called repumper laser. The repumper closes a weak loss channel from the  $^1P_1$ -state to the  $^1D_2$ -state [Lel87, Bev89] increasing the scattering

rate of the 423 nm light. During the operation of the 423 nm MOT, the laser at 657 nm irradiates the trapped atoms, storing the cold atoms in the  $^3P_1$  state. Due to the repumper and 657 nm laser the number of the trapped atoms is increased by a factor two [Deg04a]. After one second loading the blue MOT the typical atomic numbers are  $(3 - 5) \times 10^8$  at temperatures of 1-3 mK.

To further reduce the atomic temperature the second stage of cooling is used, where the 423 nm and repumper are switched off and an additional laser the quench laser is use. The resulting force effected thouth the  $^1S_0 - ^3P_1$  transition is not large enough to support the atoms against the gravity. Hence, in the second state the so-called quenched narrow-line cooling is employed [Bin01b, Ste03] using a combination of the intercombination line  $^1S_0 - ^3P_1$  and the quench  $^3P_1 - ^1D_2$  transitions to increase artificially the scattering rate. Supported by the quench laser at 453 nm the red laser at 657 nm cools and traps up to  $5 \times 10^7$  atoms at  $10 \mu\text{K}$  within 350 ms.

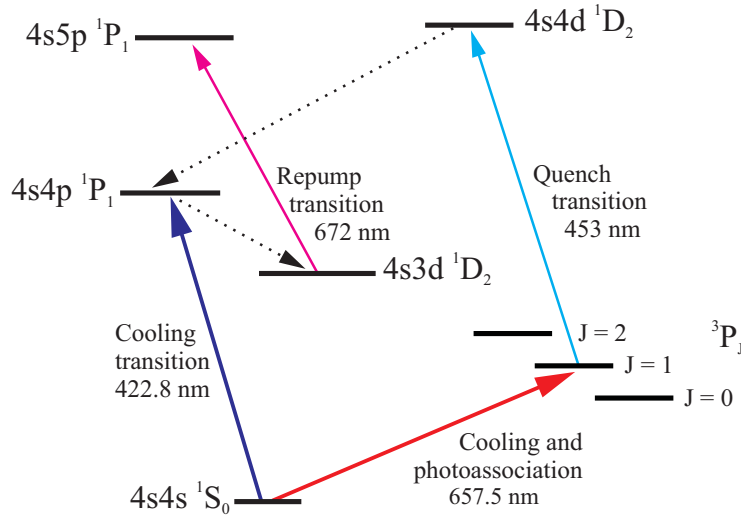


Figure 2.5: Energy level diagram of calcium atom with relevant transitions

During the MOT phases two laser beams at 1030 nm intersecting at an angle of  $54^\circ$  forming a crossed dipole trap (DT) are continuously operated [Kra09, App13]. Hence the coldest atoms attracted by the high intensity are accumulating in the crossing center of the DT. The best transfer of more than 10% into the DT is achieved when the center of the DT is located at the center of the second stage MOT. After switching off the red MOT the depth of the DT potential is subsequently ramped down. Due to this forced evaporative cooling the temperature of the cloud can be reduced further down to a few hundred nano-kelvins. Typically about  $2 \times 10^5$  atoms stay captured at a

temperature of  $1 \mu\text{K}$  with a maximal density of  $\rho \approx 10^{13} \text{ cm}^{-3}$  after 600 ms of forced evaporation. The complete cooling cycle is shown in detail in Fig. 2.6.

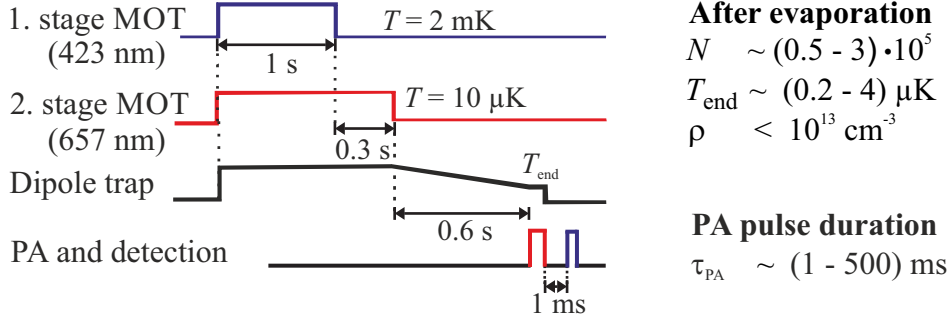


Figure 2.6: Left: ramping scheme for a cooling with followed photoassociation and detection. Right: typical experimental values achieved according to this scheme.

The PA pulse duration can be varied up to 500 ms depending on the experimental purpose. The number of atoms remaining after PA is based on absorption imaging using the  $^1S_0 - ^1P_1$  transition at 423 nm.

## 2.2.2 Laser systems

The complex laser systems have grown over long time and has been enriched by the contributions of several PhDs. Here I give a short overview of the several self-contained blocks.

The blue light at 423 nm with a power of about  $290 \text{ mW}^4$  is produced by second harmonic generation (SHG) [Deg04a]. The build-up cavity for SHG in an Lithium triborate (LBO) crystal is pumped by a commercial Titanium-Sapphire-laser *Coherent, MBR 110* and its frequency is stabilized by the Hänsch–Couillaud method [Hän80]. For the experiment the blue light is separated into several beams.

The highest power of about 160 mW is allocated for the Zeeman slower beam for decelerating the hot atoms into blue MOT with up to  $5 \times 10^8 \text{ s}^{-1}$ . The blue MOT beams use about 10 mW in total separated subsequently into six laser cooling beams. The beams intersect in the centre of the vacuum chamber creating a three dimensional MOT. The power of individual MOT beams is balanced to form a round atomic cloud in the centre of the quadrupole magnetic field created inside the vacuum chamber by internal coils with a current of 30 A. The typical life time of the blue MOT is about

<sup>4</sup>The laser light transmitting through a band-pass filter BG38 was measured at 423 nm with photodiode Thorlabs S121C 400-1000 nm

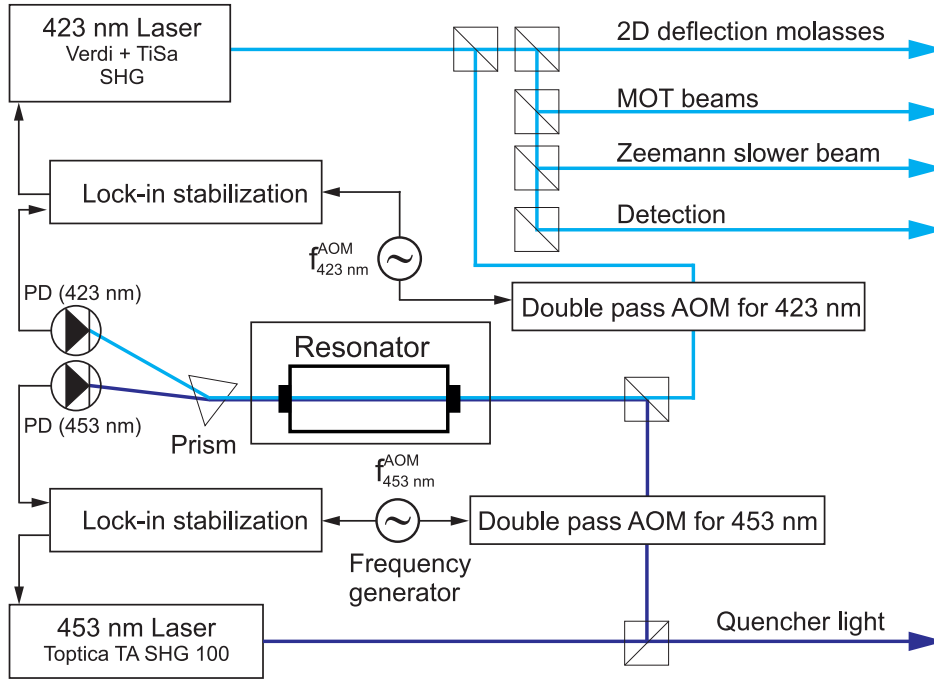


Figure 2.7: Lock-in stabilization for the 423 nm and 453 lasers to the same non-tunable reference cavity

1.3 sec. For the 2D deflection molasses 2 mW are spent. The detection laser uses less than 1 mW<sup>5</sup>. A more detailed description is documented in [Naz07].

The blue light laser at 423 nm and the quench laser system (TA-SHG 100 Toptica) at 453 nm are stabilized to the same not-tunable reference cavity with a finesse of 1000 (see Fig. 2.7). The acousto-optic modulators (AOM) in double pass configuration driven with rf frequencies  $f_{423}^{AOM}$  and  $f_{453}^{AOM}$  are used to keep the laser frequencies resonant to  $^1S_0 - ^1P_1$  and  $^3P_1 - ^1D_2$  transitions, respectively. The stabilisation and modulation are described in more detail by [Kah14a].

In contrast to the stabilization in [Kah14a] a prism was inserted behind the resonator to separate spatially the two frequencies in the transmitted laser beam into discrete beams. Thus the stabilities of the locking systems could be strongly improved by implementing individual photodiodes.

The repump light at 672 nm is produced by an extended cavity diode laser using a HL6714G-diode. The laser is lock-in stabilised to a low-finesse cavity. Typical power of the light before entering the chamber is 200 mW.

The red laser light for second-stage cooling is produced by an external cavity diode laser

<sup>5</sup>All values are measured in 1. orders of the corresponding AOMs with photodiode Thorlabs S121C 400-1000 nm.

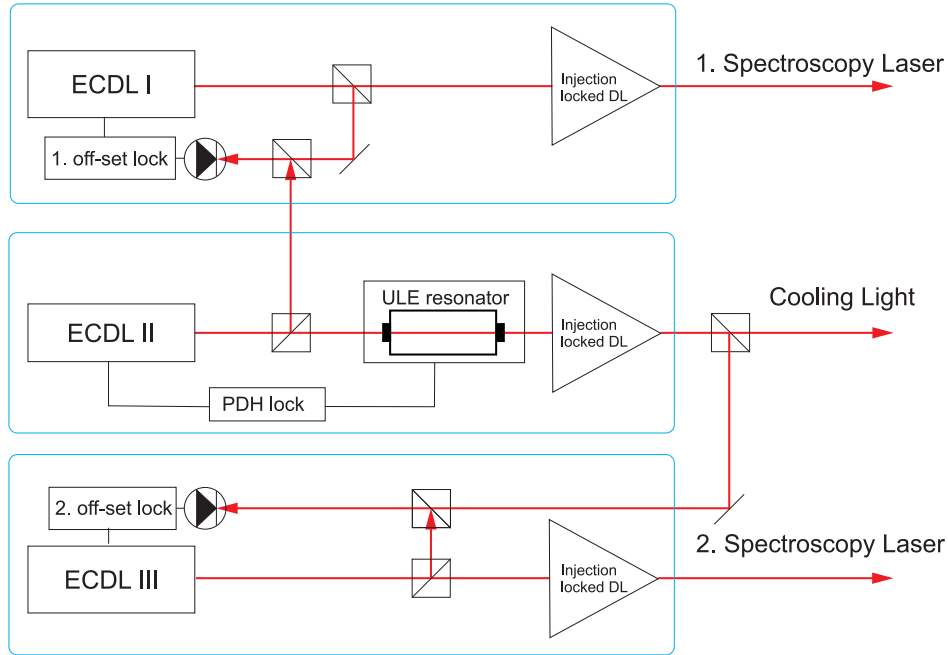


Figure 2.8: Locking scheme of the laser system at 657 nm. The blue boxes indicate the self-contained master lasers. The ultra stable ECDL II is locked to the ULE cavity by a PHD lock and is used as distributor for the stable light needed for the off-set locks of ECDL I and ECDL III and for cooling in the second stage MOT.

(ECDL). Before it is sent to the UHV chamber it is amplified by slave diode-laser. The frequency of the laser (ECDL II in Fig. 2.8) is locked to a reference resonator made of ultra-low expansion glass (ULE). On the basis of the Pound-Drever-Hall (PDH) stabilization the line width of the laser is reduced to less than 1 Hz with stability of  $3 \times 10^{-15}$  at 100 s averaging time (see also [Deg05]). Its light transmitted through the cavity is used for injection locking of a slave laser. The amplified light is sent to the experiment for the second stage MOT. The combined laser powers of the 657 nm MOT beams are 24 mW.<sup>6</sup> Two ECDL master-lasers for PA spectroscopy are offset-locked to the ECDL II with locking range of the first master up to 1.6 GHz and of the second up to 40 GHz. One of the lasers (in Fig. 2.8 indicated by ECDL I) was already used for the measurement of the photoassociation lines in the excited state potentials [Kah14b]. For two-color PA spectroscopy an improved phase comparator with the cutoff frequency of about 1.4 MHz was employed in its offset-lock in this work. Due to this improvement the whole loop bandwidth of the offset locking was increased from 100 kHz to more

<sup>6</sup>The power is measured with photodiode Thorlabs S121C 400-1000 nm, before the beams are split into six separated MOT beams.



than 1 MHz. In Fig. 2.9 a typical beat between ECDL I and ECDL II is shown. The resulting power in the carrier is about 92 %.<sup>7</sup> This value is depending on the several technical settings, e. g. on the amplification factor of the photodiode at the working frequency, and varies in a region of a few percent at the day of the measurement. To consider this technical influence, the intensities of the photoassociation lasers were corrected for the value of the power transfer to the carrier peak.

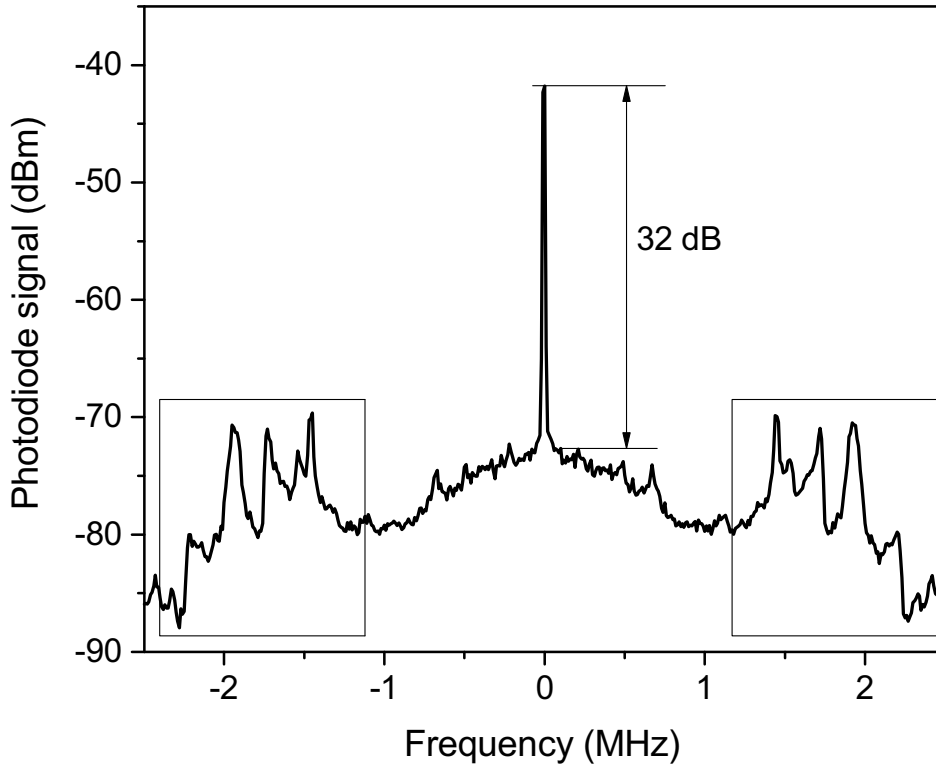


Figure 2.9: The beat between ECDL I and the ECDL II locked to the ULE cavity shows a central peak with a typical height of 32 dB and the one megahertz region of suppressed servo bands. The peaks inside the box left and right result from the ECDL II itself. The spectrum was recorded by spectrum analyser Rigol DSA 815 with RBW 1 kHz and averaged over 100 samples.

The set-up of an additional ECDL (in Fig. 2.8 indicated by ECDL III) and its implementation for two-color PA measurements was an one part of my PhD. The new laser is off-set-locked to the transmission light of the reference cavity. The transmission light is filtered by the ULE cavity, which one can see in the beat of the first offset lock (see Fig. 2.9), and has a line width of less 1 kilohertz<sup>8</sup> which is sufficient for the stabilization.

<sup>7</sup>The quality of the transfer was determined as a ratio between the area under the complete beat and a region around the carrier multiplied by 100 % (see Fig. 2.9).

<sup>8</sup>The 1 kHz width corresponds to a laser with an operating servo electronic when the trasmitted light

The ECDL III is build in a Littman configuration with a resonator length of about 10 cm. A constant of the grating inside the resonator is  $\frac{1}{1.4} \mu\text{m}$ . The laser contains the diode LD-0658-0030-AR-2, whose output face is coated with a high-quality AR coating. The laser diode and the base plate are separately temperature-stabilized by the individual Peltier elements. The base plate temperature stabilization can only heat and continuously holds the temperature at  $23.50^\circ\text{C}$ . The temperature stabilization of the laser diode in combination with its current is adjusted in such a way that the gain profile of the laser is at maximum at the operating frequency. The typical temperature varies in range of  $\pm 3^\circ\text{C}$  around  $19^\circ\text{C}$ . Depending on the temperature and wave-length settings the laser could have an output power up to 9 mW.

The light of the master laser is separated in several beams for injection locking a slave PA laser<sup>9</sup> (cf. Fig. 2.8), for beating with a ECDL II beam coming through ULE resonator and for monitoring the frequency by a wavemeter.

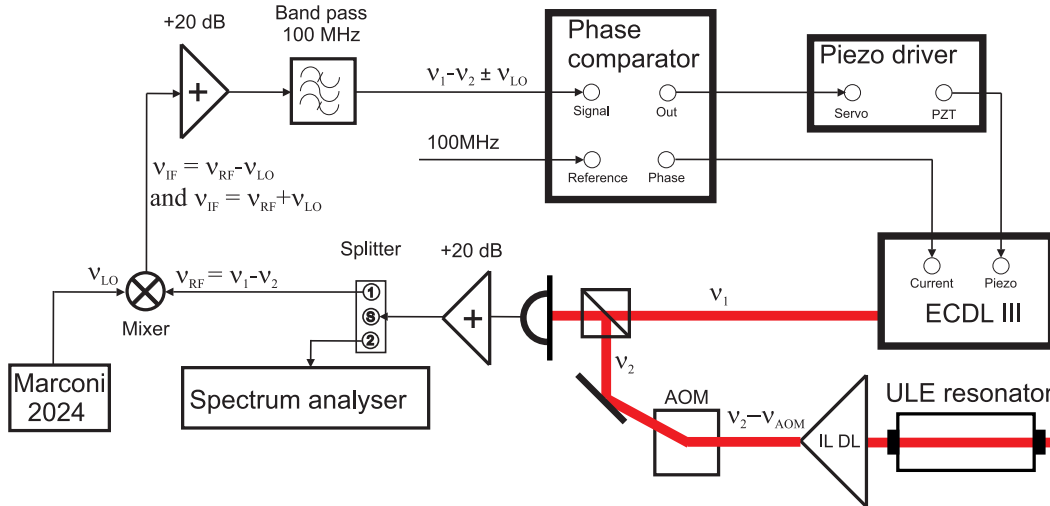


Figure 2.10: Scheme of the offset locking system of the second PA master laser (ECDL III)

For the beating the frequency of the transmitted light of the ECDL II is additionally shifted by an acousto-optic modulator (AOM) with rf-frequency  $\nu_{\text{AOM}}$  to compensate for ULE resonator shift. The complete scheme of the offset-lock is shown in Fig. 2.10. The laser beams with frequencies  $\nu_1$  and  $\nu_2$  are superimposed on a photodiode. The electric oscillation corresponding to the frequency difference is detected by the

---

was free from any kind of additional modulation around the central frequency - the cavity shows its low pass property (cf. [Naz07]).

<sup>9</sup>The end power before entering the UHV chamber in two-color configuration is up to 12 mW at 657 nm.

photodiode. With 1.5 GHz bandwidth of the photodiode the target working range of 1 GHz is well covered. The amplified (+20 dB) rf-signal is split for monitoring by a spectrum analyser and for a mixing with a local oscillator signal  $\nu_{LO}$  generated by Marconi 2024. In the mixer the sum and difference of the frequencies are produced. The frequency needed for stabilization was selected by a band pass filter at 100 MHz. The comparator produces a control signal proportional to the phase difference between the input-signal and reference frequency of 100 MHz and sends it to the next device in form of two outputs (in Fig. 2.10: out and phase). The "out" part contains the correction signal dominated by the low frequencies, typically up to 100 kHz. The amplified signal drives a piezo element, which compensates the changes in the laser frequency by shifting the mirror inside the laser. And the fast frequency (above 100 kHz<sup>10</sup>) part "phase" is connected to an additionally embedded electric network in the current driver of the laser. The function of the network is to vary the current of laser following the "phase" input signal. Thus the complete correction insures that the laser stays locked by set frequency inheriting the narrow line width being comparable to the line width of the ECDL II.

A beat spectrum between the ECDL III and light coming from ULE resonator is shown in Fig. 2.11. The central carrier peak is 32 dB high in the [-100 kHz, +100 kHz] range, 25 dB above the characteristic loop servo band peaks around  $\pm 250$  kHz. Due to the filtered cavity frequency the spectrum does not exhibit the undesirable peaks in region above 1 MHz only at 1.2 MHz coming from servo loop itself. The bandwidth of the whole servo loop stabilization is 280 kHz. The most FWHMs of the features in the spectra observed by the two-color PAS are less than 150 kHz therefore these servo loop peaks do not influence the measurements.

The important value of the efficiency of power transfer to the carrier peak is determined to about 90%. This value has always been respected by the determination of the PA beam intensity.

The dipole trap laser light of about 33 W at 1030 nm is produced by Yb:YAG disk laser pumped by diode laser JOLD-x-CAXF-6A with a maximum power of 100 W.<sup>11</sup> The dipole trap is constructed by intersecting the two beams at an angle of 54°, where one beam is tilted from the horizontal plane by 20° (details in [App13], [Vog09]). For the creation of a Bose-Einstein condensate the focus point of the tilted beam was shifted by 7 mm along its z-axis to reduce the tree-body losses [App13]. Fig. 2.12 shows a

<sup>10</sup>The bandwidth of the inserted comparator is 1.4 MHz.

<sup>11</sup>Comparad to [App13] the maximum power is increased due to replacement of the pump diode.

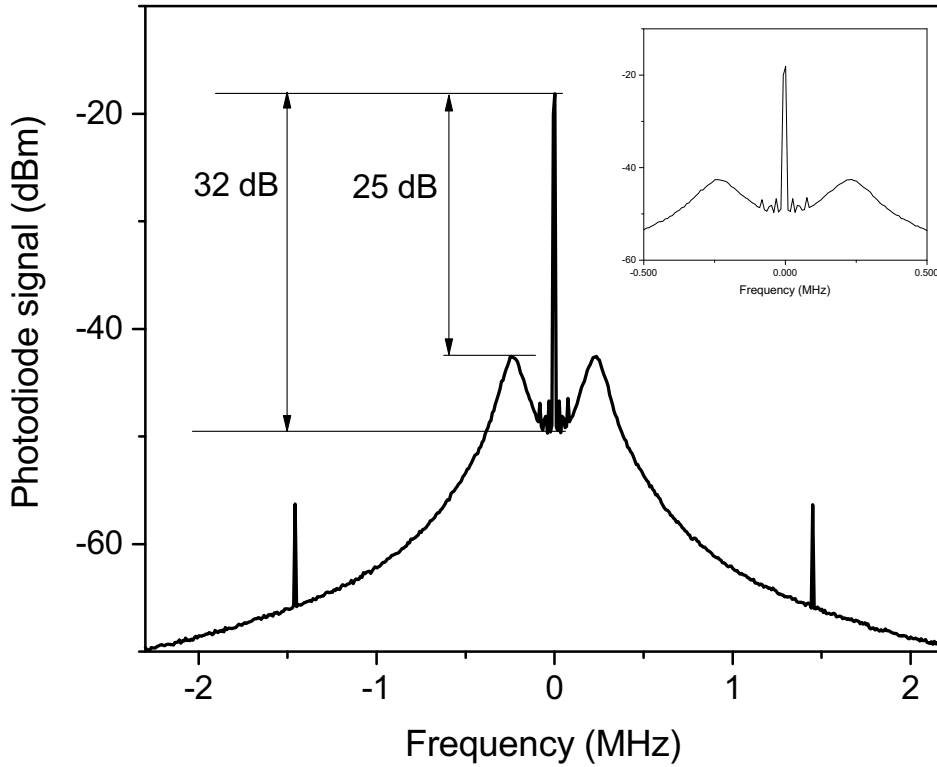


Figure 2.11: Beat signal between ECDL III and light transmitted by the ULE resonator has a central carrier peak with height of 32 dB. The inset shows the same spectrum with x-axis rescaled to  $[-0.5, 0.5]$  MHz. The spectrum is recorded by spectrum analyser Rigol DSA 815 with RBW 1 kHz and averaged over 100 samples.

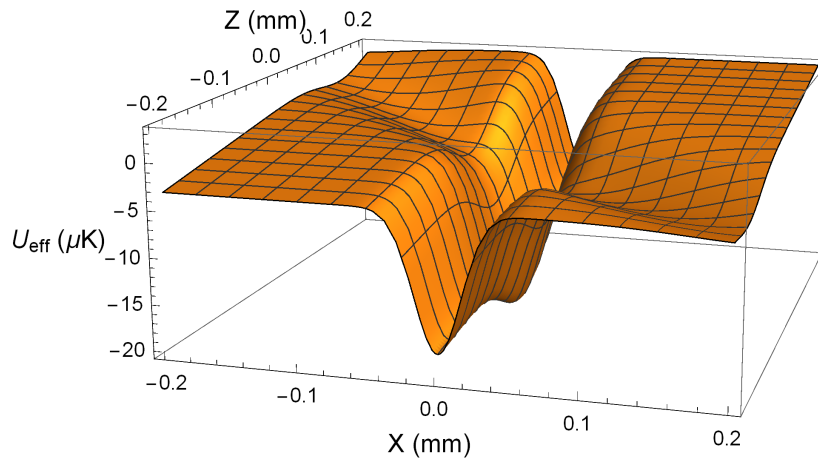


Figure 2.12: A x-z cut surface of a numeric simulation of the actual dipole trap with  $P_{\text{hor}} = 0.6$  W and  $P_t = 1.2$  W

numeric simulation of the intensity near the crossing point of the dipole trap according to the configuration used in this work. The potential shape is not symmetric and

the effective depth is also different for each axes. Therefore the simple formula for determination of trap frequencies published in [Vog09, App13] have to be extended to include the shift and angle dependence of the tilted beam. This is necessary for the accurate determination of the trap frequencies and thus the conversion of  $\beta$  to  $\langle K_{\text{in}} \rangle_{\text{T}}$ . The experimental temperature was determined from free-fall expansion of the atomic cloud in absorption images as described in [Kah14a].

### 2.2.3 Trap frequencies $\omega_{1,2,3}$

In the harmonic part of the trapping potential the atoms oscillate with characteristic eigenfrequencies.

The effective potential is

$$U_{\text{CDT}} = U_{\text{h}} + U_{\text{t}} + U_{\text{grav}} \quad (2.46)$$

with  $U_{\text{h}}$ ,  $U_{\text{t}}$  and  $U_{\text{grav}}$  the individual potentials for horizontal and tilted dipole trap beams and the gravitational potential. The gravitation deforms the trap potential, but in general its influence on the trap frequencies is not significant. Therefore it will be neglected here.

Each beam potential can be calculated as

$$U(x, y, z) = -\frac{\alpha}{2\epsilon_0 c} I(x, y, z) \quad (2.47)$$

where  $\alpha = h \cdot 47.25 \cdot 10^{-7} \text{ V}^{-2}\text{m}^2\text{Hz}$  is the polarizability of the calcium ground state atoms at a wavelength of 1031 nm [Deg04b, App13],  $\epsilon_0$  is the vacuum permittivity,  $c$  is the velocity of light and the intensity of a Gaussian beam is:

$$I(x, y, z) = I_0 \left( \frac{w_0}{w(z)} \right)^2 \exp \left[ -\frac{2(x^2 + y^2)}{w(z)^2} \right] \quad (2.48)$$

with

$$w(z) = w_0 \sqrt{1 + (z/z_{\text{R}})^2}. \quad (2.49)$$

Here  $w_0$  denotes the beam waist and  $w(z)$  the beam width at position  $z$  depending on the Rayleigh length  $z_{\text{R}} = \pi w_0^2 / \lambda$ . The waist of the horizontal and tilted beam are assumed to be  $w_0 = 32.7 \text{ } \mu\text{m}$  and  $33.3 \text{ } \mu\text{m}$ , respectively [App13].

Concerning Eqs. 2.48 and 2.47 the total potential of two Gaussian beams can be calculated by adding the horizontal beam potential rotated by  $\varphi = 54^\circ$  with the tilted beam potential shifted by  $a_z$

$$U_{\text{CDT}}(x, y, z) = \frac{\alpha}{2\epsilon_0 c} (I_h [x, (y \cos(\varphi) - z \sin(\varphi)), (z \cos(\varphi) + y \sin(\varphi))] + I_t [x, y, z - a_z]). \quad (2.50)$$

The Taylor expansion up to second order of  $U_{\text{CDT}}$  considering only quadratic and mixed terms of the potential in a matrix form can be rewritten as

$$U_{\text{CDT}}(x, y, z) = \frac{\alpha}{2\epsilon_0 c} (x, y, z) M(x, y, z)^{-1}, \quad (2.51)$$

where  $M$  is the matrix containing

$$M_{11} = \frac{2I_h}{w_h^2} + \frac{2I_t}{w_t^2} \quad (2.52)$$

$$M_{22} = \frac{2I_t}{w_t^2} + \frac{I_h \sin^2(\varphi)}{z_R^2} + \frac{2I_h \cos^2(\varphi)}{w_h^2} \quad (2.53)$$

$$M_{33} = -\frac{3I_t a_z^2 z_R^2}{(a_z^2 + z_R^2)^3} + \frac{I_t z_R^4}{(a_z^2 + z_R^2)^3} + \frac{I_h \cos^2(\varphi)}{z_R^2} + \frac{2I_h \sin^2(\varphi)}{w_h^2} \quad (2.54)$$

$$M_{23} = M_{32} = 2I_h \cos(\varphi) \sin(\varphi) \left( \frac{1}{z_R^2} - \frac{2}{w_h^2} \right). \quad (2.55)$$

The elements of higher order are neglected.

After finding the eigenvector  $v_{1,2,3}$  of  $M$  being a linear combination of  $x$ ,  $y$  and  $z$  with the corresponding eigenvalues  $\lambda_{1,2,3}$  Eq. 2.51 can be rewritten<sup>12</sup> as

$$U(v_1, v_2, v_3) = \frac{\alpha}{2\epsilon_0 c} (\lambda_1 v_1^2 + \lambda_2 v_2^2 + \lambda_3 v_3^2). \quad (2.56)$$

This kind of the potential has the same form as the harmonic potential of  $U(v_{1,2,3}) = \frac{1}{2} m \omega_{1,2,3} v_{1,2,3}^2$ .

Equated

$$\frac{1}{2} m \omega_{1,2,3} v_{1,2,3}^2 = \frac{\alpha}{2\epsilon_0 c} \lambda_{1,2,3} v_{1,2,3}^2 \quad (2.57)$$

---

<sup>12</sup>The eigenvalues can be derived by computer algebra e.g. Mathematica and are not listed here due to the large expression.

the trap frequencies frequencies can be determined to

$$\omega_{1,2,3} = \sqrt{\frac{\alpha \lambda_{1,2,3}}{\epsilon_0 c m}}. \quad (2.58)$$

The commonly used setting of 1  $\mu\text{K}$  with  $P_h = 0.6 \text{ W}$ ,  $P_t = 1.2 \text{ W}$  and shift  $a_z = 7 \text{ mm}$  for PA measurements<sup>13</sup> has resulted in the trap frequencies  $\omega_1 = 3282 \text{ s}^{-1}$ ,  $\omega_2 = 3220 \text{ s}^{-1}$ ,  $\omega_3 = 638 \text{ s}^{-1}$ .

### 2.2.4 Intensity of photoassociation laser

The knowledge of the correct intensity is very important to correctly describe the photoassociation and especially its rates. The intensity itself is a part of all calculation and is used in the analysis of all measured spectra. Therefore I allocate this section only for the description of its determination to highlight possible deviations.

The general formula for the peak intensity of a Gaussian beam with width  $w(z)$  along z-axis is

$$I(z) = \frac{2P}{\pi w^2(z)}, \quad (2.59)$$

where  $P$  is the maximum peak power of the laser beam.

As mentioned in the earlier section it has to be reduced by factor  $m$  resulting from spectral components that do not contribute to PA due to the limited performance of the electronic phase-lock-loop

$$I(z) = m \frac{2P}{\pi w^2(z)}. \quad (2.60)$$

For the determination of the waist  $w_0$  the radii of the photoassociation laser beams  $w(z)$  were measured as shown in Fig. 2.13. The individual  $\frac{1}{e^2}$  radii  $w(z)$  were determined from the beam profiles recorded by the CCD camera with pixel size of  $6.45 \mu\text{m}$ . The waist  $w_0$  is derived by fit with function according to Eq. 2.49, where  $z$  is propagation direction of the PA beam and  $z_R = \pi w_0^2 / \lambda$  Rayleigh length of light with  $\lambda = 657 \text{ nm}$ . The waists of the horizontal and vertical parts were determined to  $52 \mu\text{m}$  and  $47 \mu\text{m}$  and the waist positions differed by  $2.9 \text{ mm}$ . I assume the average waist to  $(50 \pm 4) \mu\text{m}$ , which covers the position difference with its Rayleigh length of  $3.3 \text{ mm}$ .

---

<sup>13</sup>For the calculation of the trap frequencies the powers of the beams have been corrected by the factor 0.86 which contains the absorption of the optics before entering the UHV chamber.

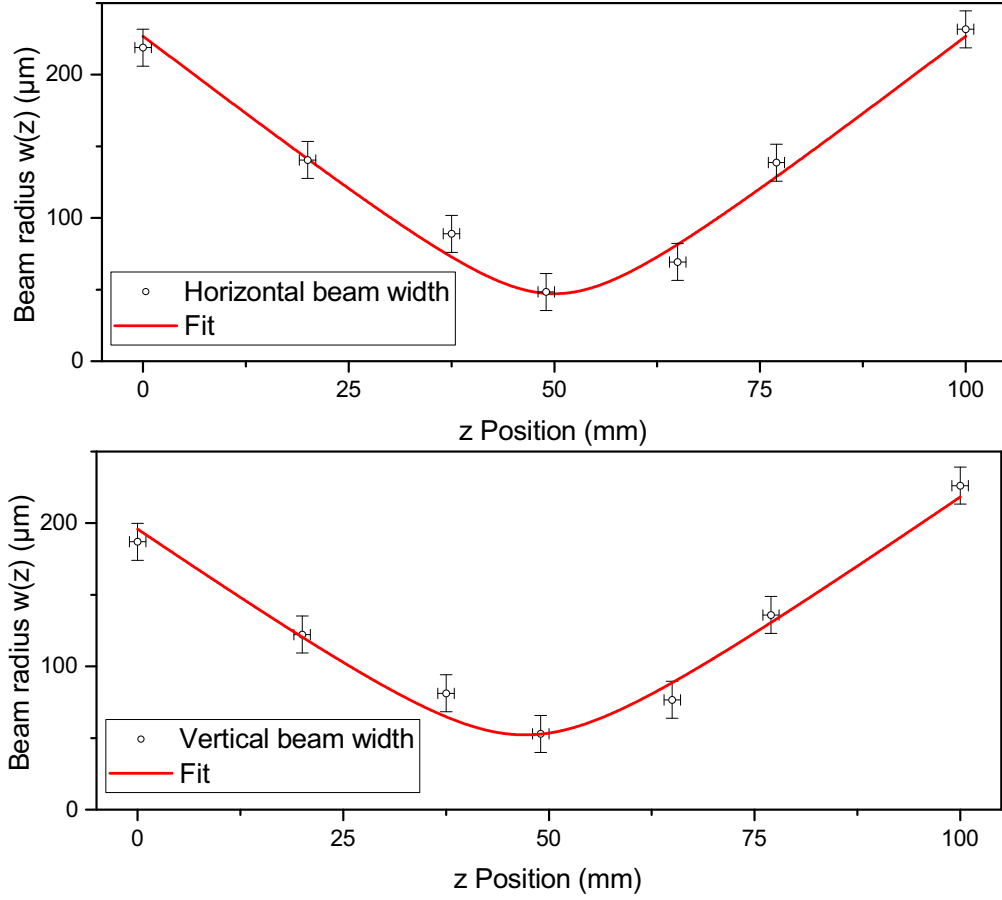


Figure 2.13: Measured beam radii of the photoassociation laser.

The typical average radius of the atomic cloud can be calculated from Eq. 2.38 using the dipole trap frequencies and is about  $10 \mu\text{m}$  at temperature of  $1 \mu\text{K}$ . Due to the size it is important to correctly focus the PA laser beam into the atomic cloud to achieve the largest intensities. Special care was taken to ensure that the focus of the PA laser beam is located at the position of the atomic cloud. To this purpose the PA laser is set to be resonant to atomic transition  $^1S_0\text{-}^3P_1$  and the number of atoms in the trap is monitored. The beam is slightly moved over the atomic cloud inducing losses from heating the atoms in the trap. The largest losses have been observed when the waist of the PA laser beam passes the centre of the atomic cloud. Due to the high sensitivity to atomic loss the focus can be accurately positioned. The beam focus is moved along the propagation beam axis by moving the focusing lens with a micrometer screw, therefore the position is almost perfect. To find the position perpendicular to propagation the same focusing lens was moved along x- and y- axis of the propagation beam. Due to rough steps of the mechanics it is more difficult to locate the focus at the atomic cloud



position, therefore this procedure was subsequently repeated, until the atomic number could not more be minimized. Due to the inaccuracy of this procedure I assume that the intensity of the PA beam at the atomic cloud position could vary up to 15 %.

Additionally, from the numeric calculation of the dipole trap for different low intensities including the gravitation force it was determined that the position of the maximal intensity is also moved up to 5  $\mu\text{m}$  away from the position of the highest power of dipole trap. Assuming that the atomic cloud moved into the region of maximal intensity of the dipole trap and the large difference of laser end powers the trap position can be moved by several micrometers between the settings for final temperatures 0.25  $\mu\text{K}$  and 1  $\mu\text{K}$  reducing the intensity by as much as 10 %.

In the analysis of the measured PA lines I assume the laser intensity according to Eq. 2.60 and its uncertainty to 20% mostly results from the above described optimization.

## 2.3 High power photoassociation

As already mentioned in Sect. 2.1.7 high power photoassociation measurements with  $s_{\text{res}}^{\text{OFR}} \gtrsim 1$  have not yet been performed on the intercombination line  $^3P_1 - ^1S_0$  of alkaline-earth metals. Due to the required high intensity it is technically difficult to achieve the required power to operate in this regime. In this section measurements are presented with a maximum intensity of about 600  $\text{W}/\text{cm}^2$  corresponding to  $s_{\text{res}}^{\text{OFR}} \approx 0.1$ , which is very close to new unexploited regime of PA. The first attempt to measure high power photoassociation spectra was already done by M. Kahmann [Kah14a]. Here I present new measurements at higher intensities with a more detailed analysis.

To verify the assumption of  $\alpha = 0$  and  $\gamma = 0$  taken for Eq. 2.28 the PA spectra were recorded at different irradiation times  $\tau$ . The upper Fig. 2.14 shows the typical photoassociation trap loss spectra of the molecular bound state  $v' = -1$  of the excited state potential  $(a, c)1_u$  measured with different irradiation durations  $\tau$  at a temperature of 1  $\mu\text{K}$ . As expected, the atom loss increases when irradiation time increases: the relative atom number loss at  $\tau = 50$  ms indicated by a green line increases by almost 50 % compared to the  $\tau = 18$  ms spectrum. The change of the atom number is in good agreement with Eq. 2.30. The lower part of Fig. 2.14 presents the corresponding atom loss coefficients  $\beta$ . Their shapes are almost identical for different  $\tau$  confirming the assumption taken for Eq. 2.28.

The corresponding inelastic collision rate coefficient  $\langle K_{\text{in}}^{\text{D}} \rangle_{\text{T}}$  indicated on the right axis is estimated according to Eq. 2.37, where the trap frequencies  $\omega_{x,y,z} = (2181 \text{ s}^{-1}, 2103 \text{ s}^{-1},$

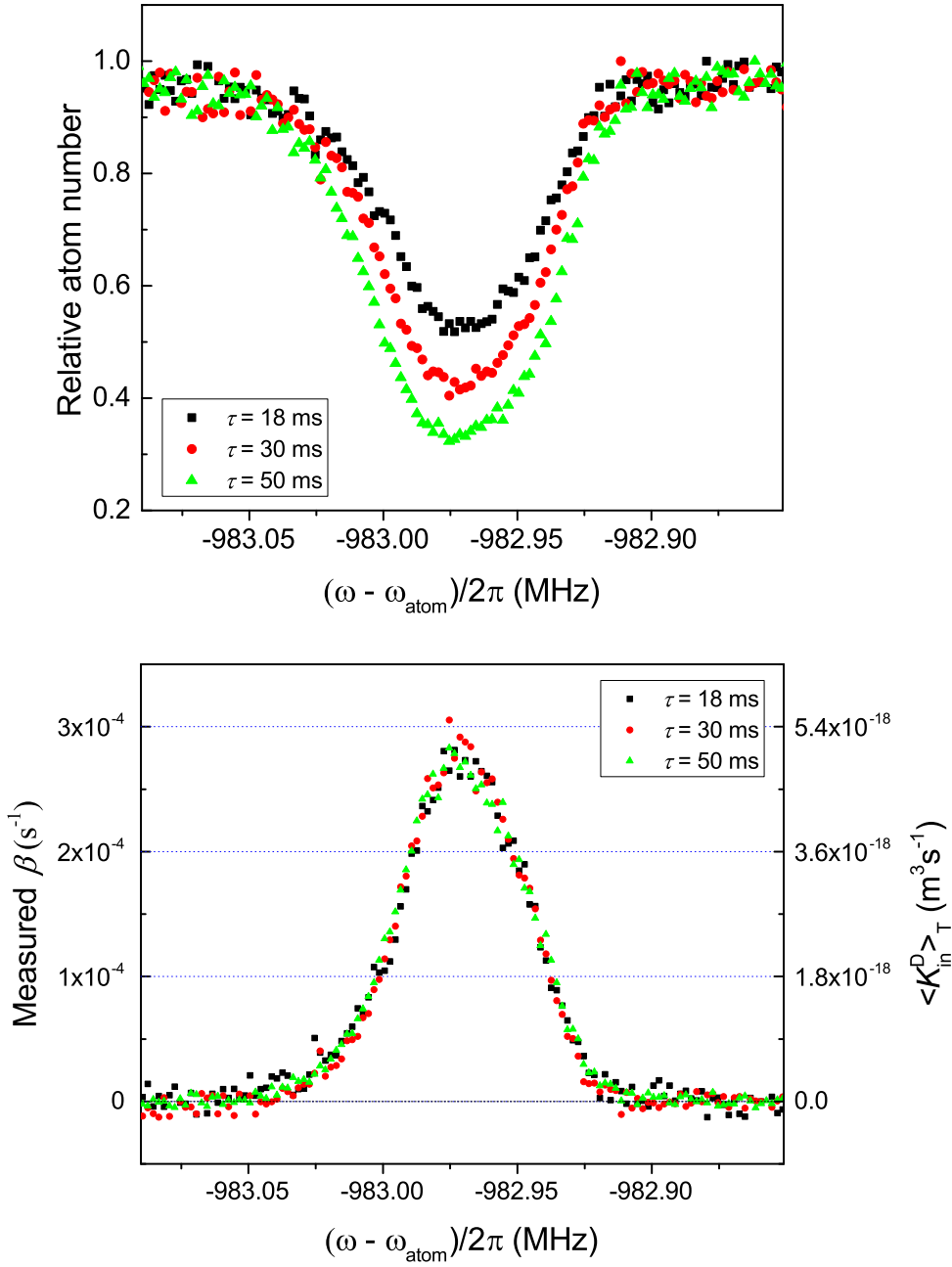


Figure 2.14: Top: measured trap loss spectra of  $v' = -1$  state of the excited state potential  $(a, c)1_u$  in dependency of the detuning from the atomic resonance with different irradiation durations  $\tau = [18 \text{ ms (black rectangles), } 30 \text{ ms (red dots), } 50 \text{ ms (green squares)}]$  and laser intensity of  $10.9 \text{ Wcm}^{-2}$  at the temperature of  $0.8 \text{ } \mu\text{K}$ . Bottom: The corresponding two body loss coefficients  $\beta$  with calculated loss rates  $\langle K_{in}^D \rangle_T$ .

$576 \text{ s}^{-1}$ ) are calculated from Eq. 2.58 and the dipole trap volume  $V_{DT} = 1.26 \cdot 10^{-14} \text{ m}^3$  with the power at the end of the ramping cycle  $P_{DT} = (P_h, P_t) = (0.25 \text{ W}, 1 \text{ W})$

according to Eq. 2.38.

The two-body loss coefficient  $\beta$  directly derived from the spectra is independent of the radiation duration  $\tau$  and the atom number  $N$ . Using Eq. 2.37 it can be converted to the inelastic loss rate  $\langle K_{\text{in}}^{\text{D}} \rangle_{\text{T}}$  connecting experiment with theory. Hence  $\beta$  is the suitable magnitude to compare the spectra for different PA intensities. In the following section its dependency on the intensity will be discussed.

### 2.3.1 Measurement of the power broadened PA lines

The presented high power measurements are performed on the bound molecular states  $v' = -1$  of the excited state potential  $c0_u^+$  and  $v' = -1$  of the excited state potential  $(a, c)1_u$ . In the experiments the cloud of ultracold calcium atoms prepared at different temperatures up to  $3.5 \mu\text{K}$  is irradiated by the linearly polarized laser light with successively increased intensities of up to  $560 \text{ Wcm}^{-2}$ . During the irradiation an external magnetic field of  $(263 \pm 10) \mu\text{T}$  parallel to the polarization of the PA laser light is applied. The value of the magnetic field was verified by spectroscopy of the Zeemann splitting of the atomic transition. To guarantee linear polarization of the PA laser light the beam passes through a polarizing beam splitter before entering the UHV chamber.

### 2.3.2 Full width at half maximum (FWHM) of the measured PA lines

The PA lines of the molecular bound states  $v' = -1$  in  $c0_u^+$  and  $v' = -1$  in  $(a, c)1_u$  in dependency of the laser light intensity were measured. The Figs. 2.15 show the FWHM of the measured  $\beta$ . These widths are broadened by different physical effects such as the Doppler effect, thermal broadening and power broadening.

Additional simplifications are discussed to point these physical phenomena in the measured spectra.

The dotted line represents the FWHM of a line  $\langle \beta(\Delta_1) \rangle_{\text{T}}^{\text{calc}}$  which resulted only from the Boltzmann distribution, where the individual spectral line is processed as a Dirac delta function. This FWHM can be derived from

$$\langle \beta(\Delta_1) \rangle_{\text{T}}^{\text{calc}} = \int_0^{\infty} \frac{2}{(k_{\text{B}}T)^3} \sqrt{\frac{\epsilon}{\pi}} \exp\left(-\frac{\epsilon}{k_{\text{B}}T}\right) \delta_{\text{Dirac}}(\Delta_1 - \epsilon) d\epsilon \quad (2.61)$$

In the top and bottom spectra the experimental temperatures are  $1.08 \mu\text{K}$  and  $0.80$

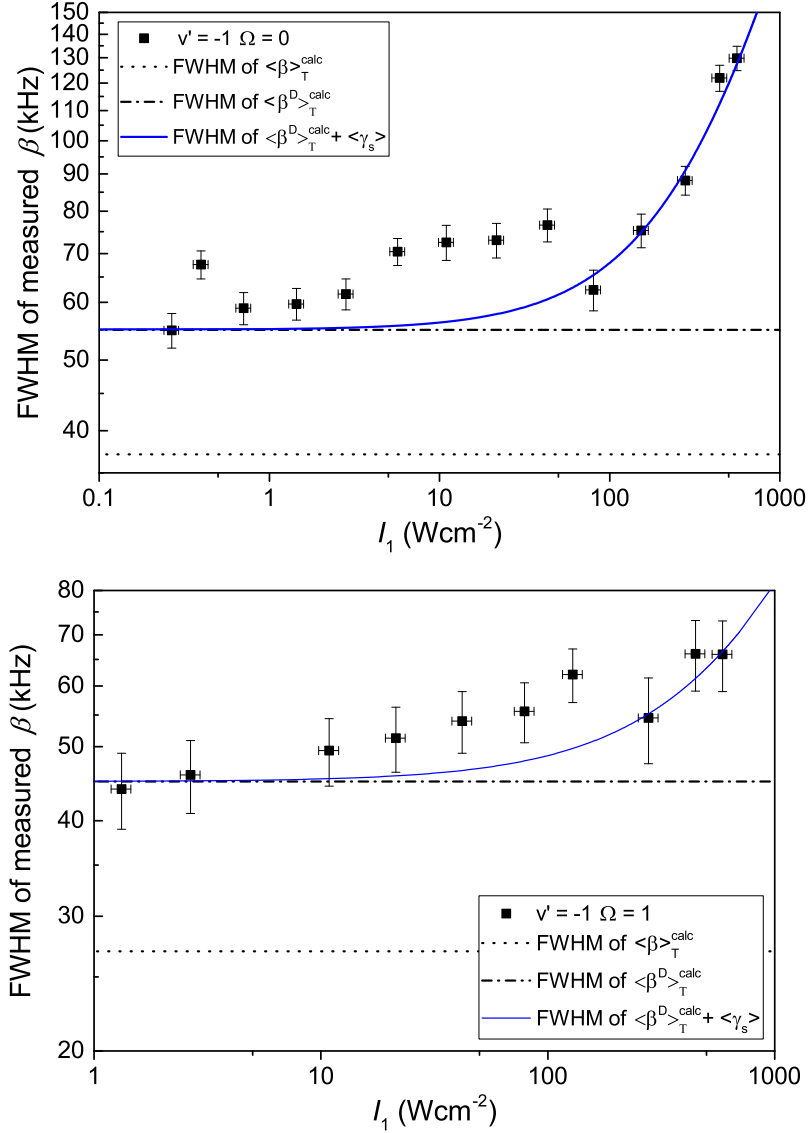


Figure 2.15: Observed FWHM of observed  $\beta$  to the  $v' = -1$  in  $c0_u^+$  and  $v' = -1$  in  $(a, c)1_u$  in dependency of the PA laser intensity  $I_1$ . The dotted line indicates the width of only the Boltzmann distribution (see Eq. 2.61). The dot-dashed line indicates the FWHM of the convolution of the thermal and the Doppler broadening (see Eq. 2.62). The blue line indicates the additional broadening from  $\langle \gamma_{stim} \rangle$  induced by the coupling to the laser field.  $\langle \gamma_{stim} \rangle$  is a thermal average over the collision energy dependent stimulated rates (see Eq. 2.63).

$\mu\text{K}$ , respectively. Using Eq. 2.61 the thermal widths result in about 37 kHz and 27 kHz, respectively.

The next approximation for the FWHM is the convolution  $\langle \beta^{\text{D}}(\Delta_1) \rangle_{\text{T}}$  between the thermal distribution and a Gaussian with FWHM  $\Gamma_{\text{D}}$  according to 2.40. This line

shape is typical for the low intensity excitation and is a good approximation, where the power broadening is much smaller compared to the Doppler broadening. Here  $\Gamma_D = 37.8$  kHz at  $T = 1.08$   $\mu$ K and  $\Gamma_D = 32.5$  kHz at  $T = 0.8$   $\mu$ K, which is large compared to the natural width of the  $^1S_0$ - $^3P_1$  transitions:

$$\langle \beta^D(\Delta_1) \rangle_T = \int_0^\infty \frac{2}{(k_B T)^3} \sqrt{\frac{\epsilon}{\pi}} \exp\left(-\frac{\epsilon}{k_B T}\right) \exp\left[-4 \ln(2) \left(\frac{\Delta_1 - \epsilon}{\Gamma_D}\right)^2\right]^2 d\epsilon. \quad (2.62)$$

For the top spectrum this convolution yields a FWHM of  $\langle \beta^D \rangle_T \approx 55$  kHz and for the bottom spectrum 45 kHz.

The observed FWHM of the measured spectra in both measurements stay nearly constant in the low intensity range of less than 5  $\text{Wcm}^{-2}$  and are in good agreement with the calculated FWHM of  $\langle \beta^D \rangle_T$  according to Eq. 2.62. This behaviour indicates that the Doppler effect and thermal broadening is the dominating broadening mechanism in the low intensity region.

As the intensity of the laser increases the FWHM of the measured  $\beta$  also increase. This behaviour is observed by  $v' = -1$  in  $c0_u^+$  in the high intensity region over 100  $\text{Wcm}^{-2}$ . This increase of the line widths indicates that the power broadening can no longer be neglected. The power broadening mechanism can be estimated by the stimulated rate  $\gamma_{\text{stim}}$  discussed in Sect. 2.1.1. According to Wigner threshold law [Wig48] the stimulated rate  $\gamma_{\text{stim}}$  depends on the collision energies  $\epsilon_{\text{col}}$  inside the thermal cloud. In order to effectively compare the measurements it is reasonable to introduce the thermally averaged stimulated rate  $\langle \gamma_{\text{stim}} \rangle^{14}$  to estimate a combined influence on the line broadening:

$$\langle \gamma_{\text{stim}} \rangle = \langle \gamma_{\text{stim}} \rangle_T = \sqrt{\pi} l_{\text{opt}} \frac{\sqrt{2\mu k_B T}}{\hbar} 2\gamma_{\text{atom}} \propto I_1. \quad (2.63)$$

The stimulated width is linearly proportional to the optical length, hence it is proportional to the intensity of the PA laser. Therefore in the high intensity range the line widths of the measured resonances should also increase linearly with the intensity, while the Doppler and thermal broadening contribution stays constant.

The blue line indicates an additional contribution of  $\langle \gamma_{\text{stim}} \rangle$  (see Eq. 2.63) to the FWHM of the PA lines broadened by the Doppler effect and thermal contribution. In the high intensity region over 100  $\text{Wcm}^{-2}$  the measured FWHM coincide with the blue line in

---

<sup>14</sup>The complete derivation of the thermal averaged stimulated rate  $\langle \gamma_{\text{stim}} \rangle$  is described in appendix 4

terms of measurement accuracy in both measurements. From this behaviour I conclude that the calculated and measured stimulated rates  $\gamma_{\text{stim}}$  are in good agreement. Hence, the Franck-Condon densities  $f_{\text{FCD}}(\epsilon_{\text{col}})$  discussed in Sect. 2.1.1 correctly describe the coupling between the bound molecular and the scattering states.

In the intensity region between 5 and 100  $\text{Wcm}^{-2}$  the measured line widths deviate slightly from  $\langle\beta^{\text{D}}\rangle_{\text{T}}$ , large enough. This increase can not be explained by the here described three broadening mechanisms and indicates for additional broadening mechanisms.

### 2.3.3 Results from Voigt fits

To shed more light on the increase of the PA line widths a quantitative analysis of the individual lines was performed. As explained in the Sect. 2.1.5 the PA resonance can be described by the thermal averaged spectral lines, where the individual lines are broadened through the Doppler effect. Such resonances can be calculated by using Eq. 2.41.

Due to the complexity of this description and the mutual influence of the variables I use a simplified approximation for a fit of the observed PA spectra.

Firstly, the individual lines in such a resonance, described by the inelastic collision rate coefficient  $K_{\text{in}}$  according to Eq. 2.10, are Lorentzian with the line width  $\gamma_{\text{L}} = \gamma_1 + \gamma_{\text{stim}}(k)$ . To implement  $K_{\text{in}}$  into the fit routine I did some additional approximations concerning the stimulated rate  $\gamma_{\text{stim}}$ . To reduce the coupling between the fit parameters in the denominator I used a constant width  $\gamma_{\text{stim}}$  for all collision energies  $\epsilon_i$ <sup>15</sup>, which can be interpreted as the thermally averaged stimulated rate  $\langle\gamma_{\text{stim}}\rangle$ . The  $\sqrt{\epsilon_{\text{col}}}$  dependency arising from the Wigner threshold law in  $\gamma_{\text{stim}}$  for the low temperatures is still considered in the numerator. The simplified result is

$$f_1 = \frac{2A}{\pi} \frac{\gamma_{\text{L}}}{4(x - x_c)^2 + \gamma_{\text{L}}^2} \quad (2.64)$$

where the  $x$  is the detuning and  $x_c$  is the resonance position of the rovibrational level. Secondly, the individual lines  $K_{\text{in}}$  are broadened by the Doppler effect. Its influence can be approximated by the convolution of the above Lorentzian with a Gaussian with line width  $\Gamma_{\text{D}} = \gamma_{\text{G}}$  resulting from Doppler broadening as discussed in Sect. 2.3.2.

---

<sup>15</sup>This restriction of the constant widths turned out to be necessary to achieve convergence of the fit routine after a reasonable time.

This convolution is also contained in Eq. 2.41 and is the well-known Voigt profil. The function  $f_2$  is an area normalized Gaussian

$$f_2(x) = \sqrt{\frac{4\ln(2)}{\pi}} \frac{e^{-\frac{4\ln(2)}{\gamma_G^2} \cdot x^2}}{\gamma_G}. \quad (2.65)$$

For the convolution I used the fitting routine for a Voigt function called 'voigt5.fdf' of the program "Origin", which is defined as

$$\begin{aligned} nlf\_voigt(x, y_0, x_c, A, \gamma_G, \gamma_L) &= y_0 + (f_1 * f_2)(x) \\ &= y_0 + A \frac{2\ln(2)}{\pi^{3/2}} \frac{\gamma_L}{\gamma_G^2} \int_{-\infty}^{+\infty} \frac{e^{-t^2}}{\left(\sqrt{\ln(2)} \frac{\gamma_L}{\gamma_G}\right)^2 + \left(\sqrt{4\ln(2)} \frac{x-x_c}{\gamma_G} - t\right)^2} dt, \end{aligned} \quad (2.66)$$

where  $A$  is the area under the Voigt profile and  $y_0$  is an offset corresponding to the initial  $\beta$ .

Thirdly, to consider the thermal distribution coming from the integration over all thermal velocities contained in  $\langle K_{in} \rangle_T$  (Eq. 2.27) the integral is approximated by a discrete sum with step size  $\delta\epsilon$  to enable the usage of the complete fit function in the program "Origin".

The final simplified fit function of the sum instead of an integral over the individual Voigt profiles weighted with Boltzmann factors according to the thermal distribution is

$$\begin{aligned} \langle \beta^D(\Delta_c, \Delta_1, I_1, T) \rangle_T &\propto \beta \sum^D (\Delta, \Delta_c, T, B, \gamma_L, \gamma_G) = \\ &B \sum_n \delta\epsilon \sqrt{n \cdot \delta\epsilon} \exp\left(-\frac{n \cdot \delta\epsilon}{k_B T}\right) nlf\_voigt(\Delta_1 + n \cdot \delta\epsilon, y_0, \Delta_c, 1, \gamma_G, \gamma_L), \end{aligned} \quad (2.67)$$

where the  $\sqrt{n \cdot \delta\epsilon}$  factor stems from the Wigner threshold law,  $\Delta_c$  is the resonance position,  $\gamma_L$  is contribution of the FWHM of the Lorentzian line and  $\gamma_G$  is the FWHM of the Gaussian part of the Voigt profile.

The observed PA spectra were fitted with this fit routine and the fit temperatures were compared. In general the fit temperatures are consistent between each other and differed less than 10 % of all measurements. Compared to the fit temperatures the measured TOF temperatures differ generally by 20 %. Due to this relative good agreement of the temperatures I kept the fit temperatures at a fixed value to avoid

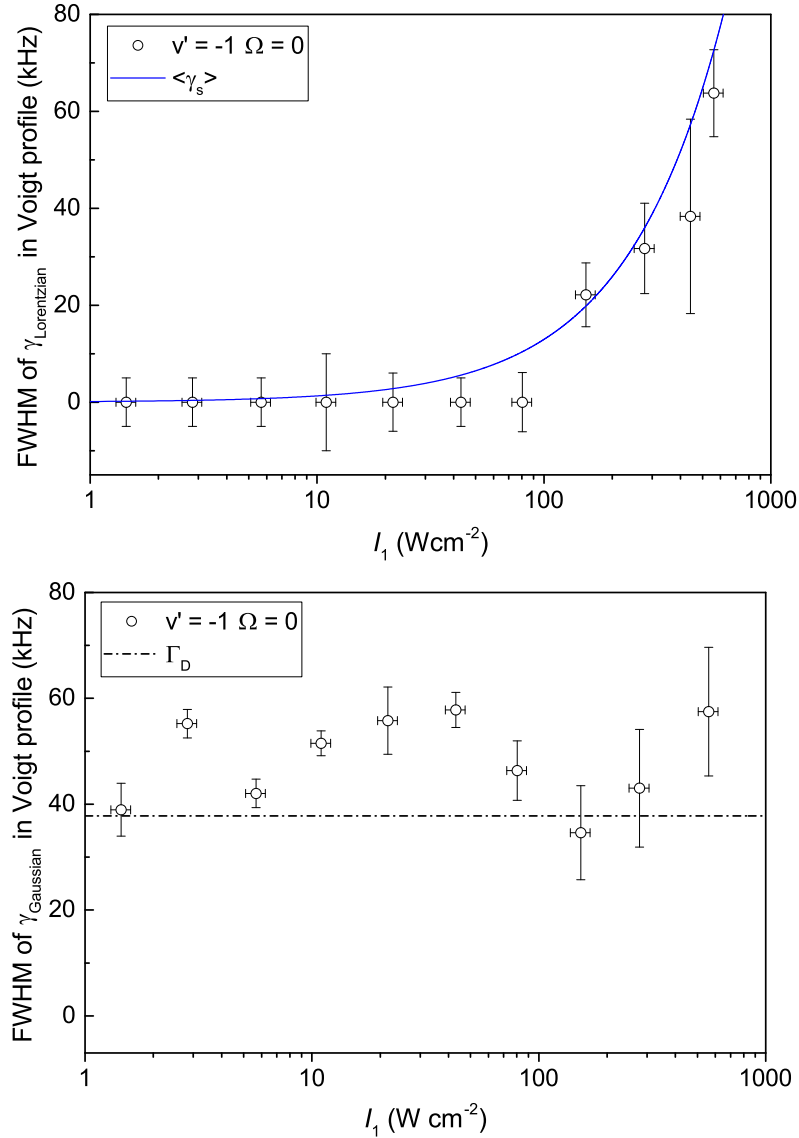


Figure 2.16: The  $\gamma_{\text{Lorentzian}}$  and the  $\gamma_{\text{Gaussian}}$  of the Voigt profiles for the molecular bound state  $v' = -1$  in  $c0_u^+$  in dependency of the PA laser intensity are shown in the top and bottom figures, respectively. The black empty dots are the derived widths with the error bars adapted from the fitting routine. The blue line represents the widths of the thermal averaged stimulated rate  $\langle \gamma_s \rangle$  calculated using the FCD from Tab. 2.1. The black dash-dotted line indicates the Doppler width  $\Gamma_D$  at temperature  $1.08 \mu\text{K}$ .

additional coupling between the fit parameters. In the analysis is  $T_{\text{fit}} = 1.08 \mu\text{K}$  for the  $v' = -1$  in  $c0_u^+$  and  $T_{\text{fit}} = 0.8 \mu\text{K}$  for the  $v' = -1$  in  $(a, c)1_u$ .

The observed  $\gamma_L$  and  $\gamma_D$  of the Voigt profiles for the excited molecular bound vibrational state  $v' = -1$  in  $c0_u^+$  and  $v' = -1$  in  $(a, c)1_u$  in dependency of the PA laser intensity  $I_1$  are shown in Fig. 2.16 and Fig. 2.17, respectively.



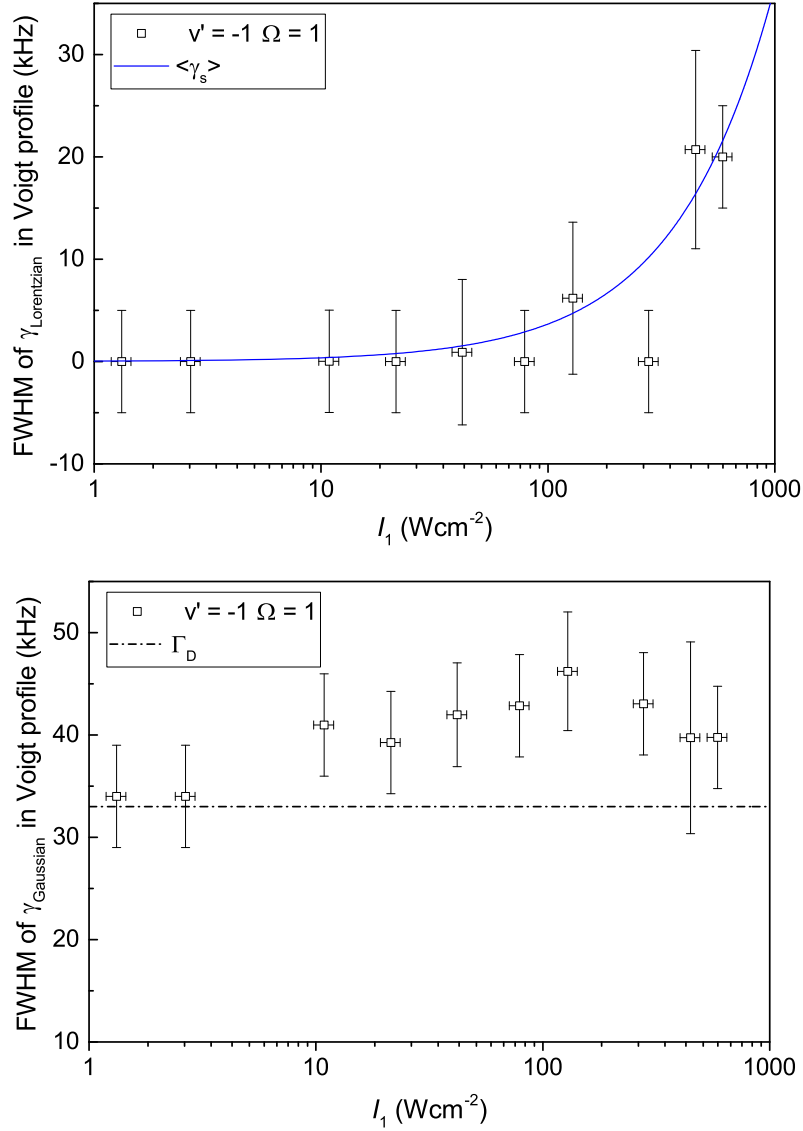


Figure 2.17: The  $\gamma_{\text{Lorentzian}}$  and the  $\gamma_{\text{Gaussian}}$  widths of the Voigt profiles to the molecular bound state  $v' = -1$  in  $(a, c)1_u$  in dependency of the PA laser intensity are shown in top and bottom figures, respectively. The black empty squares are the derived widths with the error bars adapted from the fitting routine. The blue line represents the widths of the thermal averaged stimulated rate  $\langle \gamma_s \rangle$  calculated using the FCD from Tab. 2.1 and the dash-dotted line indicates the Doppler width  $\Gamma_D$  of the temperature  $0.8 \mu\text{K}$ .

The advantage of the fitting routine is the relative strong separation of the influence of the temperature/Doppler effect, which is reflected in the FWHM of the Gaussian of the Voigt profile, and the combined influence of the intensity and several effects shortening the life time of the bound state, which is reflected in the FWHM of the Lorentzian of the Voigt profile.  $\gamma_G$  corresponds directly to the Doppler width  $\Gamma_D$  allowing a direct

comparison with the calculated Doppler width.  $\gamma_L$  corresponds to the line width of the measured state and can be understood as  $\gamma_L = \gamma_1 + \langle \gamma_{\text{stim}} \rangle$ .

The observed Lorentzian line widths both for the  $v' = -1$  in  $c0_u^+$  and for  $v' = -1$  in  $(a, c)1_u$  stay small in the low laser intensity range less than  $5 \text{ Wcm}^{-2}$ . Even in the crossover region between 5 and  $100 \text{ Wcm}^{-2}$  the values change insignificantly. In the high intensity region over  $100 \text{ Wcm}^{-2}$  the measured Lorentzian widths increase with intensity in both measurements. This behaviour supports the theoretical prediction for the stimulated rate widths  $\langle \gamma_{\text{stim}} \rangle$  and the calculated values of  $\langle \gamma_{\text{stim}} \rangle$  agree inside the error bars. This indicates that the Franck-Condon densities (see Tab. 2.1) used in the calculation are correct, even in the investigated high intensity region.

The Gaussian widths in both measurements tend to be larger than the calculated Doppler width  $\Gamma_D$ . They stay roughly constant in contrast to the Lorentzian width for all intensities. In the crossover intensity region the increasing FWHM of the measured  $\beta$  correlates with the simultaneously increase of the Gaussian widths. Since the Gaussian correlate with the Doppler and temperature effects, the relative change of 25% of the widths in the crossover region could be interpreted as the temperature variation due to elastic collision during the PA.

### 2.3.4 Inelastic collision rate coefficient $K_{in}$

The two body loss rate coefficient  $\beta$  derived from the measured spectra was compared with the theoretical inelastic collision rate coefficient  $\langle K_{in}^D \rangle_T$  to investigate the validity of the influence of theoretical description of the high intensity laser light on the inelastic scattering rate in the dipole trap.

For the comparison the experimental inelastic collision rate coefficient  $\langle K_{in}^D \rangle_T$  were derived from the observed two body loss rate coefficient  $\beta$  using Eq. 2.42 by considering the geometry of the dipole trap contained in the effective volume Eq. 2.38. The effective volume was derived individually for every dipole trap depth at the day of the measurement.

In Tab. 2.3 the calculated  $V_{DT}$  are given for the measurements of the PA lines  $v' = -1$  in  $c0_u^+$  and  $v' = -1$  in  $(a, c)1_u$ . As already mentioned above, the TOF temperatures and the fit temperatures differed by up to 20 %. To consider this discrepancy I compare PA spectra at low intensity with the same TOF temperature with the temperatures derived by the fit routine (see Eq. 2.67), while the fit temperature was not fixed. This is a regime, where only Doppler and temperature broadening are relevant and other

	$v' = -1$ in $(a, c)1_u$			$v' = -1$ in $c0_u^+$	
$T$ ( $\mu\text{K}$ )	0.4 (0.45)	0.8 (1.0)	1.8 (2.2)	1.08(1.08)	3.35(3.35)
$(P_h, P_t)$ (W)	(0.15, 0.5)	(0.25, 1.0)	(0.5, 2.0)	(0.6, 1.2)	(1.2, 2.0)
$\sqrt[3]{\omega_x\omega_y\omega_z}$ ( $\text{s}^{-1}$ )	1036	1383	1955	1890	2589
$V_{DT}$ ( $\times 10^{-15} \text{ m}^3$ )	10.2	12.6	15.1	7.8	16.5

Table 2.3: Calculated effective volume  $V_{DT}$  for different geometries at the day of measurements of  $v' = -1$  in  $c0_u^+$  and  $v' = -1$  in  $(a, c)1_u$ . Temperatures  $T$  and the TOF temperatures in brackets are listed in second line.  $T$  were used to calculate  $V_{DT}$ . The mean trap frequencies with corresponding end powers  $P_h$  and  $P_t$  in the horizontal and tilted beams of the dipole trap at the end of the ramping cycle are listed in third and second lines, respectively.

broadening do not contribute to the total line width. Considering the power of the dipole trap at the end of the ramping cycle the used temperature was estimated.

For example in the measurement of the  $v' = -1$  in  $c0_u^+$  the mean value of the fit temperatures for the measurements with  $T_{\text{TOF}} = 1.08 \mu\text{K}$  is also  $1.08 \mu\text{K}$  in the low intensity PA spectra. In contrast, the mean value of the fit temperatures for the measurement of  $v' = -1$  in  $(a, c)1_u$  with  $T_{\text{TOF}} = 1.0 \mu\text{K}$  is only  $0.6 \mu\text{K}$  in the low intensity PA spectra. Additionally the corresponding power of dipole trap is lower indicating the effective temperature lower than  $1.0 \mu\text{K}$ . Therefore I used for the determination of  $V_{DT}$  the averaged temperature  $T = 0.8 \mu\text{K}$ . All used temperatures were estimated by this consideration.

The maxima of the two body loss coefficients  $\beta$  from the measurements of  $v' = -1$  in  $c0_u^+$  and  $v'$  in  $(a, c)1_u$  are shown in the left y-axis in the top and bottom Figs. 2.18, respectively. The corresponding derived values of the inelastic collision rate coefficient  $\langle K_{\text{in}}^{\text{D}} \rangle_{\text{T}}$  calculated using conversion Eq. 2.38 are shown in the right y-axis.

The theoretical  $\langle K_{\text{in}}^{\text{D}} \rangle_{\text{T}}$  calculated according to Eq. 2.41 with corresponding  $\langle \beta^{\text{D}} \rangle_{\text{T}}$  converted by Eq. 2.38 using the parameters derived experimentally are indicated by the red lines.

The measured  $\beta$  linearly increase with PA laser intensity in both measurements. Only the PA line  $v' = -1$  in  $c0_u^+$  potential shows a saturation behaviour in the high intensity region.

Comparable to the measured  $\beta$  the corresponding theoretical  $\beta$  represented by the red lines increase linearly in the low intensity range of less than  $10 \text{ Wcm}^{-2}$ , but are significantly larger by the factor of 16 in both measurements. In the range of the

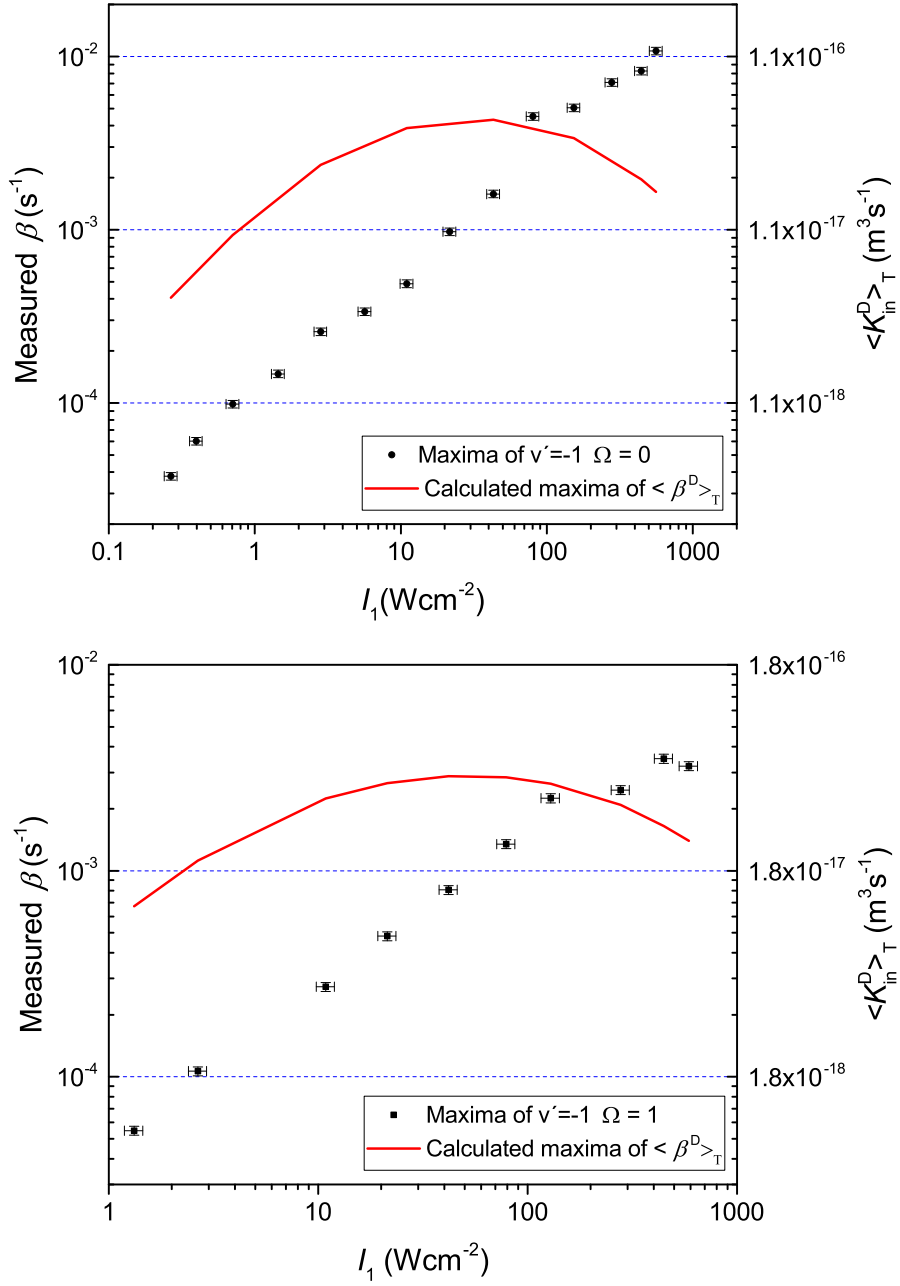


Figure 2.18: The observed two body loss coefficients  $\beta$  with the corresponding inelastic collision rate coefficient  $\langle K_{\text{in}}^{\text{D}} \rangle_{\text{T}}$  for the measurements of the  $v' = -1$  in  $c0_u^+$  and  $v' = -1$  in  $(a, c)1_u$  in the dependency of the PA laser intensity  $I_1$  are shown in top and bottom figures, respectively. The red lines indicate  $\beta$ 's calculated using Eq. 2.42 and theoretical values of  $\langle K_{\text{in}}^{\text{D}} \rangle_{\text{T}}$  Eq. according to 2.41.

intermediate intensities they saturate and at the high intensities even decrease. This behaviour of the calculated values in the low intensity range show that the theoretical formalism overestimates the experimental losses. At intermediate and high intensities the theory does not correctly describe the experimental photoassociative losses.

### 2.3.5 Spectral line areas

The observed two-body loss coefficients  $\beta$  are affected by the Doppler effect thereby complicating the analysis. An alternative approach tries to exclude the influence of the Doppler effect by analysis of the spectral area under the measured  $\beta$ . The principle is based on the constancy of the spectral areas. The Doppler effect broadens the PA resonances, but the area under the resonance does not change [Mes99]. This feature is also contained in the Voigt profile used for description of the Doppler broadened spectral lines, where the Gaussian only changes the shape of the complete Voigt profile leaving the area unaltered. For example for the used Voigt profile in Eq. 2.66 the function  $f_2$  is a normalized Gaussian with the spectral area of 1 and the parameter  $A$  of the function  $f_1$  is equal to the area of the Voigt profile, which at the same time scales with the Lorentzian area only. This property is contained also in the Gaussian of Eq. 2.41, the area under the Doppler Gaussian is always constant. Therefore the change of the spectral area at a constant temperature  $T$  is affected only from the changes of the Lorentzian in Eq. 2.41, which is proportional to the changes of the  $\langle K_{\text{in}} \rangle_T$  in Eq. 2.41. The top and bottom Figs. 2.19 show the observed spectral areas for  $v' = -1$  of  $c0_u^+$  and  $v' = -1$  in  $(a, c)1_u$ , respectively, indicated by the black dots in dependency of the PA laser intensity.

Instead of Eq. 2.42, which can be used to determine the complete PA lines shape and their area, the spectral areas were derived by the fitting function `nlf_voigt` of "Origin" to reduce the analysis to a reasonable time.

The calculated areas indicated by the red solid line in Fig. 2.19 were derived according to Eq. 4.18 as  $Area(\beta) = \frac{2}{\sqrt{8} V_{DT}} Area_2(\langle K_{\text{in}}^D \rangle_T)$  (see Appendix 4).

The values of the observed areas linearly increase in the low and intermediate intensity region in both measurements. At high intensities the area of  $v' = -1$  in  $(a, c)1_u$  saturates.

Comparable to the measured areas the calculated values linearly increase and are larger by the factor 16 in the low intensity region in both measurements. In contrast to the experimental areas they saturate already in the middle intensity range. Therefore I

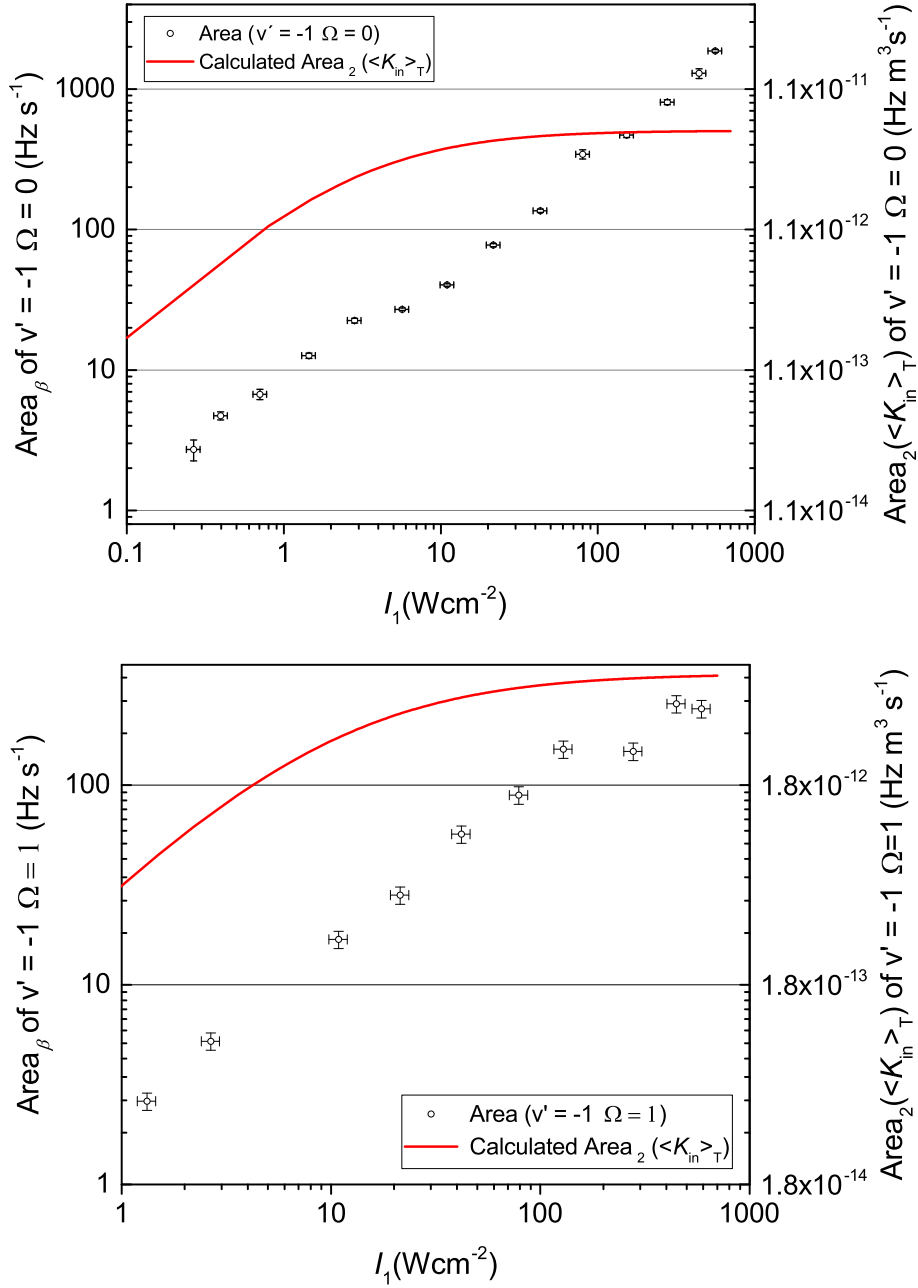


Figure 2.19: Areas under the measured lines of  $v' = -1$  in  $c0_u^+$  (top),  $v' = -1$  in  $(a, c)1_u$  (bottom) are shown in dependency of the PA laser intensity. The spectral areas are represented by two scales, one in (Hz/s) directly derived from the measured  $\beta$  spectra and the corresponding  $\langle K_{in}^D \rangle_T$  (Hz m $^3$  s $^{-1}$ ) scale converted by considering the dipole trap geometry. The red solid lines represent the calculated areas.

conclude that even when excluding the Doppler effect the resonant scattering theory is not reproducing the measured rates, especially in the high intensity region.

### 2.3.6 FWHM and $\beta$ at different temperatures

Furthermore, the dependency of the two-body loss rate  $\beta$  of the temperature of the atomic cloud was investigated for PA to the bound molecular state  $v' = -1$  in  $(a, c)1_u$ . The top part of Fig. 2.20 shows the measured spectra at different temperatures. These measured spectra were recorded at low intensity of about  $11 \text{ Wcm}^{-2}$  to prevent additional high-power effects.

As expected the thermal broadening increases the width proportional to  $T$  according to the Boltzmann distribution. Also the maxima of the spectra decrease as the temperature increases. This behaviour results from the Voigt profile of individual lines, where the area under an individual spectral line stays constant. This behaviour is expected for the spectral areas at low intensities for the different temperatures (see Eqs. 4.15 and 4.18). This is confirmed by the areas in Tab. 2.4.

$T$ ( $\mu\text{K}$ )	0.2	0.4	0.8	1.8	2.5
Area ( $\text{s}^{-1}\text{Hz}$ )	16(3)	19(3)	16(3)	12(3)	15(3)

Table 2.4: Derived areas of  $v' = -1$  in  $(a, c)1_u$  for different temperatures irradiated with  $I_1 = 11 \text{ Wcm}^{-2}$

In addition the measured spectral lines were fitted by a single Gaussian to investigate the line shape. The Gaussian fits can not consider the slightly asymmetrical shape typical for the thermal broadened spectral lines. This asymmetry is clearly visible in the high temperature spectra, where the right wings at low collision energies at the right hand side can not fitted by the single Gaussian.

In the bottom Fig. 2.20 the derived maximal coefficients  $\beta$  are shown for low and high intensities of the  $11 \text{ Wcm}^{-2}$  (black squares) and  $588 \text{ Wcm}^{-2}$  (circles), respectively. As expected, the observed  $\beta$  decrease approximately linearly with increasing temperature. The corresponding green and red lines are calculated according to Eq. 2.42 for the low and high intensities. The slopes of the calculated lines reproduce the slope of the measured  $\beta$  in both measurements indicating a correct dependency between the temperature and the measured losses  $\beta$ . However the absolute values again show a deviation of a factor of 16. The obvious matching at high intensities is probably fortuitous when the decrease of the theoretical value of the maxima in Fig. 2.18 at high intensity is taken in account. The behaviour of the calculated two-body loss rate coefficients  $\langle \beta^D \rangle_T$  for the temperature dependency reproduce the behaviour of the maxima and the areas discussed in Secs. 2.3.4 and 2.3.5, where the losses at low

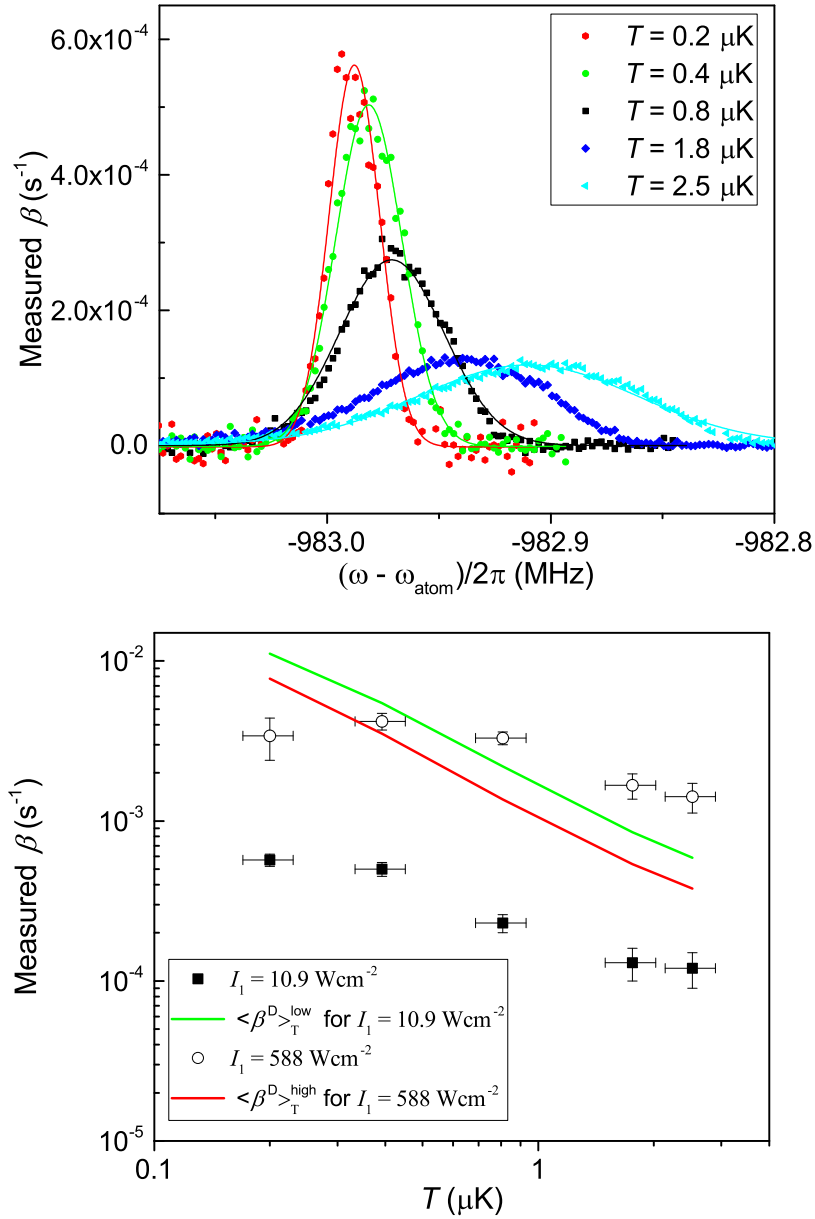


Figure 2.20: Top: the observed spectra of bound molecular state  $v' = -1$  in  $(a, c)1_u$  with the single Gaussian fits (solid lines) irradiated with intensity of about  $11 \text{ Wcm}^{-2}$  at different temperatures. The spectra are not corrected for the ac-Stark shift of the DT laser. Bottom:  $\beta$  for intensities of  $11 \text{ Wcm}^{-2}$  (squares) and  $588 \text{ Wcm}^{-2}$  (circles) in dependency of the temperature. The green and red lines indicate calculated values according Eq. 2.42 for  $11 \text{ Wcm}^{-2}$  and the red line for  $588 \text{ Wcm}^{-2}$ , respectively.

intensities are larger by a factor of 16.

Additionally the PA line FWHM of the molecular bound states  $v' = -1$  in  $c0_u^+$  and  $v' = -1$  in  $(a, c)1_u$  in dependency of the temperature were evaluated (2.21).



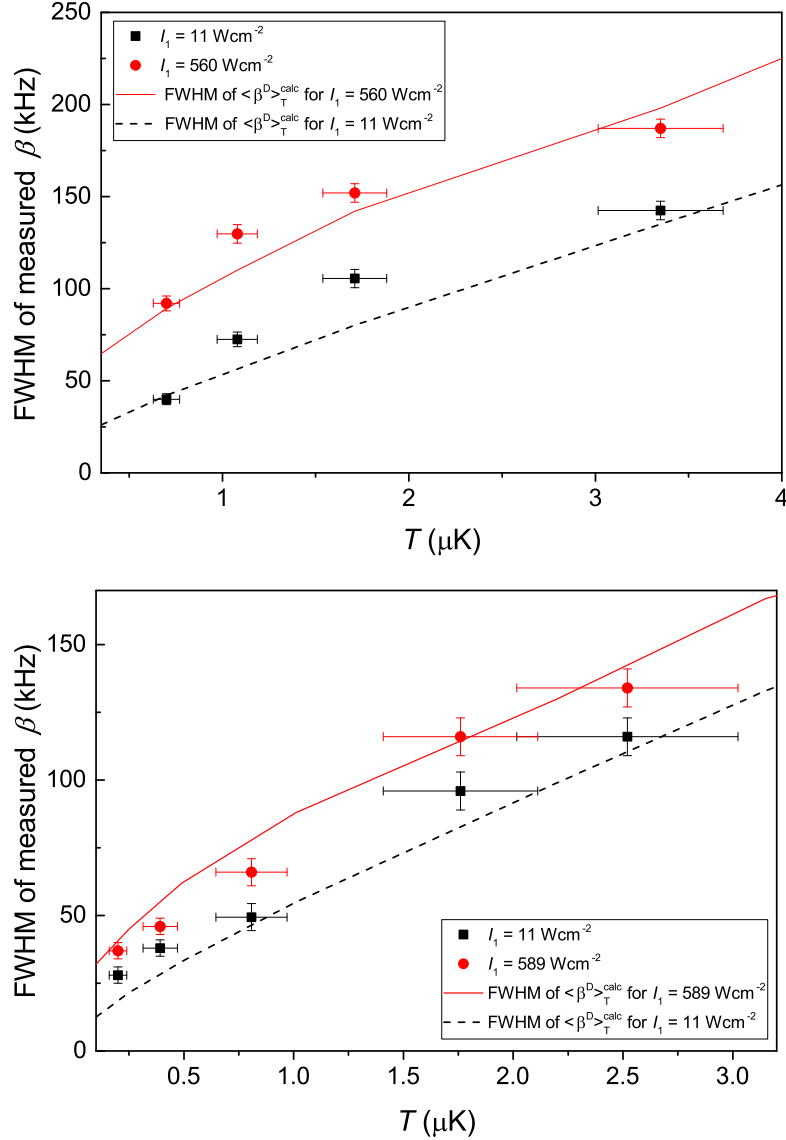


Figure 2.21: Observed PA line widths of the molecular bound states of the  $v' = -1$  of  $c0_u^+$  (top) and  $v' = -1$  in  $(a, c)1_u$  (bottom) irradiated by two intensities of about  $11 \text{ Wcm}^{-2}$  (black squares) and  $560 \text{ Wcm}^{-2}$  and  $589 \text{ Wcm}^{-2}$  (red dots) in dependency of the atomic cloud temperature.  $\langle\beta^D\rangle_T$  is the typical FWHM of the Doppler broadened PA line calculated according to Eq. 2.62 for low laser intensity. The red line  $\langle\beta^D\rangle_T$  for the high intensity is calculated according to the Eq. 2.42

The black squares indicate the FWHM observed at low intensity of about  $11 \text{ Wcm}^{-2}$ , where the shape of observed PA line is dominated by the Doppler and thermal broadening. The corresponding theoretical FWHM calculated according to Eq. 2.62 are indicated by the black dashed lines. In both measurements the calculated FWHM of the Doppler broadened PA lines reproduce the slope of the observed FWHM and the

absolute values.

The FWHM measured in the high intensity regime are indicated by the red dots. The red lines are the corresponding theoretical values calculated using Eq. 2.42.

The calculated line widths follow the measured spectral widths. Therefore I assert that the temperature dependency of the line widths at high intensities is also correctly considered.

The upper analysis shows clearly that the temperature influence, which corresponds to the Doppler and thermal broadening, is correctly described by the used resonant scattering theory even at high intensities.

## 2.4 Prospects for large modification of the scattering length $a$

Many applications of cold quantum gases can benefit from a modification of the scattering properties (see [Gri05]). Photoassociation can be used to modify the interaction properties by coupling to near resonant light. These optically induced changes of the scattering length for an isolated resonance can be calculated from scattering matrix element  $S_{0,0}$  as in Eq. 2.43

$$a(\Delta_1, l_{opt}, \epsilon) = a_{bg} + a_{opt}(\Delta_1, l_{opt}) = a_{bg} + \frac{l_{opt}\gamma_1\Delta_1}{\Delta_1^2 + \frac{(\gamma_1 + \gamma_s(\epsilon))^2}{4}}. \quad (2.68)$$

The biggest changes occur at the detuning  $\Delta_1 = \frac{\gamma_1 + \gamma_{stim}(\epsilon)}{2}$ . Unfortunately at this detuning the losses are still substantial (see Fig. 2.22).

For large detuning, the photoassociative losses are inversely proportional to the square of the detuning, at the same time the change of the scattering length is only inversely proportional to the detuning. Hence a large change in scattering length can be induced at relatively small detuning with respect to a rovibrational resonance without producing large photoassociative losses.

The alkali elements have in general broad PA lines, therefore it is not possible to detune from one PA line without approaching other resonances. The molecular intercombination lines of Sr are about 14 kHz wide, but they lie very close to each others. Thus the theoretical description of the isolated resonance would be not valid here. In contrast to them, the calcium intercombination lines of 748 Hz are very narrow and lie several

MHz from each other, therefore it should be possible to detune sufficiently far away from one resonance and still remain far detuned from all other lines. I use this fact to estimate useful setting for the induced significant large  $a_{\text{opt}}$  without considerable losses.

As shown in earlier sections, even at high intensities the stimulated rate  $\gamma_{\text{stim}}$  and the corresponding optical lengths are correctly described by the calculated Franck-Condon densities given in the Tab. 2.1. Therefore they can be used to estimate the scattering length changes induced by the PA laser.

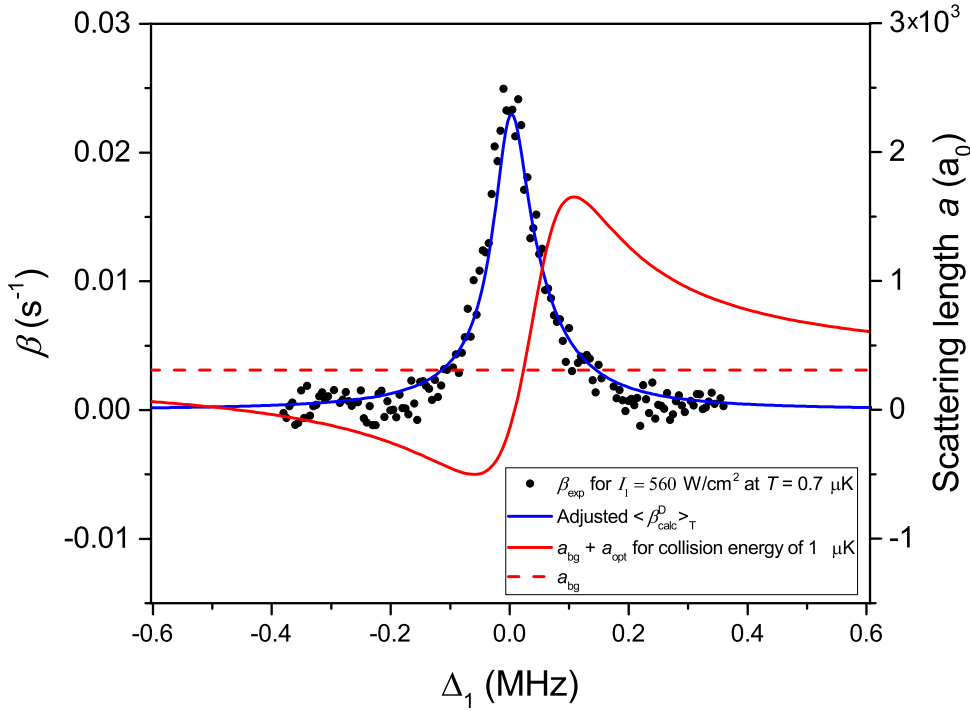


Figure 2.22: Measured  $\beta$  of  $v' = -1$  of  $c0_u^+$  irradiated by  $560 \text{ Wcm}^{-2}$  in dependency of the detuning  $\Delta_1$  (black dots) and calculated scattering length  $a$  for collision energy  $\epsilon_{\text{col}}/k_B = 1 \text{ } \mu\text{K}$  (red solid line). The red dashed line is the s-wave scattering length  $a_{\text{bg}} = 308.5 a_0$ . The blue solid line is the calculated two body loss coefficient  $\langle \beta_{\text{calc}}^D \rangle_T$  according to Eq. 2.42 with height adjusted to the experimental  $\beta$ .

Fig. 2.22 shows a measured PA spectrum of  $v' = -1$  in  $c0_u^+$  taken at a temperature of  $0.7 \text{ } \mu\text{K}$  with a PA laser intensity of  $560 \text{ W/cm}^2$  together with the corresponding calculated  $\langle \beta^D \rangle_T$  and scattering length  $a$ .

As already shown in the earlier section the experimental  $\beta$  at the low intensities are

$\Delta_1$ (MHz)		-1	-0.8	-0.5	-0.25	0.3	0.5	0.8	1
$a_{\text{opt}}$ ( $a_0$ )	$\epsilon/k_B = 0.5 \mu\text{K}$	-161	-200	-313	-585	572	340	211	168
	$\epsilon/k_B = 1 \mu\text{K}$	-158	-194	-298	-521	590	351	215	171
	$\epsilon/k_B = 2 \mu\text{K}$	-150	-183	-270	-423	626	371	225	177
$3x\langle K_{\text{in}}^{\text{D}} \rangle_{\text{T}}$ ( $\times 10^{-18} \text{ m}^3 \text{ s}^{-1}$ )		0.4	0.6	1.40	4.98	4.64	1.66	0.64	0.4

Table 2.5: Calculated induced scattering length  $a_{\text{opt}}$  for collision energies  $\epsilon/k_B = (0.5, 1, 2) \mu\text{K}$  according to Eq. 2.42 for  $I_1 = 560 \text{ Wcm}^{-2}$  with  $\langle K_{\text{in}}^{\text{D}} \rangle_{\text{T}}$  increased by a factor 3 from Fig. 2.22.

smaller than the theoretical values by the factor 16. In contrast at the high intensities (in Fig. 2.18) the observed  $\beta$  are large compared to the theoretical ones. At the intensity of  $560 \text{ Wcm}^{-2}$  the theoretical value need to be increased by the factor 3. In the Fig. 2.22 the blue solid line indicates the calculated spectral line  $\langle \beta_{\text{calc}}^{\text{D}} \rangle_{\text{T}}$  using Eq. 2.42 and increased by the factor 3 fitting the measured  $\beta$ .

The red solid line indicates the corresponding calculated scattering length for a collision energy  $\epsilon/k_B$  of  $1 \mu\text{K}$  according to Eq. 2.43. The red dashed line indicates the background scattering length of  $308 a_0$ . In the interesting detuning ranges of low losses  $\Delta_1 < -250 \text{ kHz}$  and  $\Delta_1 > 300 \text{ kHz}$  the scattering length  $a = a_{\text{bg}} + a_{\text{opt}}$  reaches large values up to  $800 a_0$  and goes down to  $-200 a_0$ . At  $\Delta_1 \approx 0.5 \text{ MHz}$  it becomes zero.

Comparable values for the induced optical contribution  $a_{\text{opt}}$  is calculated for collision energies of  $0.5$  and  $2 \mu\text{K}$ . In Tab. 2.5 the  $a_{\text{opt}}$  for reasonable detuning values are listed. The calculated values are comparable at the identical detuning  $\Delta_1$  in the range over  $500 \text{ kHz}$ . This indicates the similar influence of the near resonant laser light on the individual collision energies, which could be advantageous for the further application. Additionally  $\langle K_{\text{in}}^{\text{D}} \rangle_{\text{T}}$  is derived from the  $\langle \beta_{\text{calc}}^{\text{D}} \rangle_{\text{T}}$  by using  $V_{\text{DT}} = 4.05 \cdot 10^{-15} \text{ m}^3$ .

To understand the influence of the irradiation duration  $\tau$  the relative atom number calculated for different  $\tau$  using Eq. 2.32 with adjusted  $\langle \beta_{\text{calc}}^{\text{D}} \rangle_{\text{T}}$  are shown in Fig. 2.23. This calculation shows that it is already technically possible to modify the scattering length in the relative large range from  $-200 a_0$  to  $800 a_0$ , but the irradiation duration  $\tau$  needs to be less than  $50 \text{ ms}$  to preserve more than  $50 \%$  of the atoms after PA. To reduce the losses it is useful to reduce the temperature of the atomic cloud (see Figs. 2.20 and 2.21).

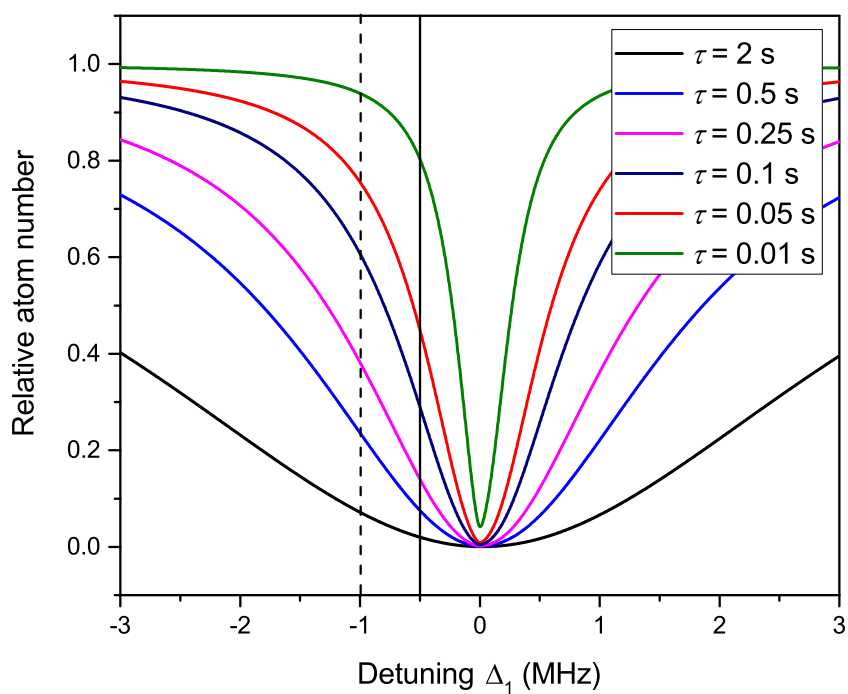


Figure 2.23: Calculated relative atom number in dependency of the irradiation time  $\tau$  using the adjusted  $\langle \beta_{\text{calc}}^{\text{D}} \rangle_{\text{T}}$  from Fig. 2.22. The dashed and solid lines indicate the position at the -1 MHz and -0.5 MHz, respectively.



## Chapter 3

# Two-color photoassociation of ultracold calcium

Several molecular properties of  $^{40}\text{Ca}$  [Kah14b, Tie15] like the binding energies of the excited potential, its dispersion coefficients  $C_6$ ,  $C_8$  and molecular  $g$  factors are already estimated, by the one-color photoassociation. They lead to an understanding of interaction between the ultracold calcium atoms in the excited states. In comparison to one-color PA, the two-color PA via an excited molecular state allows to probe the interaction between the atoms in their electronic ground state. Two-color PA has been already used for the investigation of binding energies and scattering lengths of the alkaline atoms Li [Abr97], Na [vA99], K [Wan00], Rb [Tsa97], Cs [Van04], and more recently for systems with two valence electrons  $\text{He}^*$  [Kim04], Sr [MdE08] and Yb [Kit08].

In this chapter the detailed results of the publication [Pac17] are presented submitted recently to Physical Review A. This is the collective effort of the Ca group at Physikalisch-Technische Bundesanstalt (PTB) and Prof. Eberhard Tiemann, who made all required calculation for the determination of the molecular potentials and the optical transition rates.

The measurement of the four least bound molecular states in the ground potential  $X^1\Sigma_g^+$  is presented. This measurement complements the short range ground-state potential determined by molecular spectroscopy [All03] that provided information about the interaction potential up to 2 nm internuclear separations.

The newly observed levels with binding energies up to 8.2 GHz with respect to the  $^1S_0 + ^1S_0$  asymptote were used for precise determination of the long range behavior of the interaction and for estimation of the s-wave scattering length  $a$  that plays a key role for the elastic scattering properties of  $^{40}\text{Ca}$  at ultralow temperatures [Kra09].

In a complementary measurement the molecular dipole matrix element for a particular

transition between vibrational states in the electronically excited and the ground state potential is determined from the Autler-Townes splitting created by coupling of these states with a resonant laser field.

### 3.1 Theoretical description of two-color photoassociation

The PA-spectra are evaluated using the theoretical model developed by Bohn and Julienne [Boh96, Boh99]. It considers a pair of colliding atoms with a kinetic energy  $\epsilon$  of relative motion in the presence of two light fields with frequency  $\omega_1$  and  $\omega_2$ . The Fig. 3.1 shows the scheme of the two-color PA used in the measurement. The green and black lines indicate the excited and ground state potentials. The grey rectangle indicates the thermal energies of colliding atoms.

The frequency  $\omega_1$  of the first laser is tuned closely to a bound molecular resonance used as an intermediate state to induce the coupling between an excited rovibrational state  $|1\rangle$  to the scattering state  $|\epsilon\rangle$ . The detuning from this intermediate state is  $\Delta_1$ , i.e. for  $\Delta_1 = 0$  the light field is in resonance with the free-bound transition for collision energy  $\epsilon = 0$ .

The second laser with frequency  $\omega_2$  drives the bound-bound transition between states  $|1\rangle$  and  $|2\rangle$ . The combined two-color-detuning with respect to the ground state bound level located  $\hbar \cdot \Delta_b < 0$  below the ground state asymptote is given by  $\Delta_2 = \Delta_b - (\omega_1 - \omega_2)$ . Hence the two-color resonance at  $\epsilon = 0$  corresponds to  $\Delta_2 = 0$ .

According to the resonant scattering theory [Boh99] the calculation of the two-color transition splits into three channels with scattering matrix elements  $S_{\epsilon\epsilon}$ ,  $S_{\epsilon 1}$  and  $S_{\epsilon 2}$ , which can be interpreted as elastic scattering between the neutral atoms themselves ( $S_{\epsilon\epsilon}$ ), with losses from an excited state  $|1\rangle$  ( $S_{\epsilon 1}$ ) and losses from the bound molecular state  $|2\rangle$  ( $S_{\epsilon 2}$ ), respectively. Considering the Raman configuration employed in this work and assuming an infinite life time of the bound molecular state in ground potential the matrix element  $S_{\epsilon 2}$  can be neglected.

Thus on the two-color resonance, the main loss mechanism results from excitation to the intermediate state  $|1\rangle$ , from where the photoassociated molecules decay spontaneously and produce atoms with high enough energy, which could escape from the dipole trap. For samples at  $\mu\text{K}$  temperatures only s-wave scattering is important, and the probability for a two-color PA loss from the input scattering channel  $|\epsilon\rangle$  to the excited state



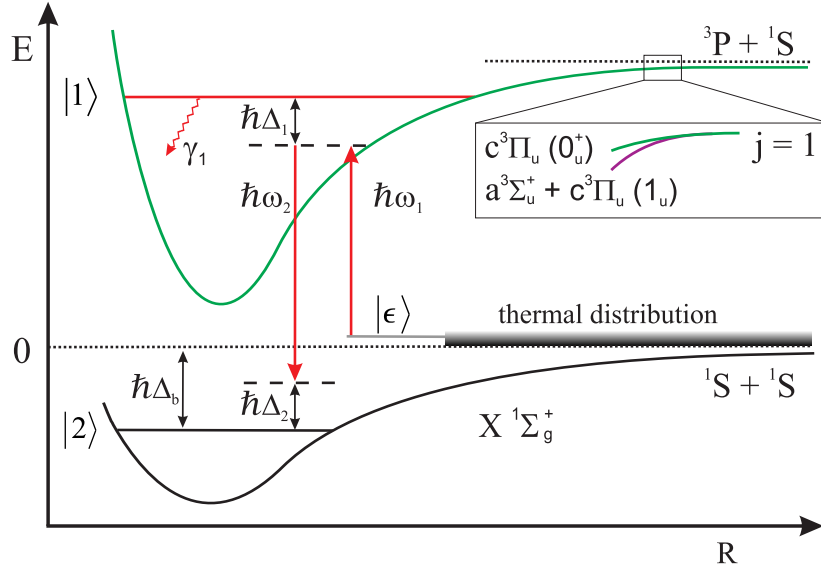


Figure 3.1: Schematic overview of the two-color PA process featuring the involved molecular potentials of  $\text{Ca}_2$ , using intermediate states near the  $^1S_0 + ^3P_1$  asymptote ( $\lambda = 657 \text{ nm}$ ).

$|1\rangle$  is given by the squared scattering matrix element  $|S_{\epsilon 1}|^2$  [Boh99]:

$$|S_{\epsilon 1}|^2 = \frac{\gamma_1 \gamma_{\text{stim}} \Delta_2'^2}{(\Delta_1' \Delta_2' - \Omega_{12}^2)^2 + ((\gamma_1 + \gamma_{\text{stim}}) \Delta_2' / 2)^2} \quad (3.1)$$

with  $\Delta_2' = \Delta_2 - \epsilon_{\text{col}} / \hbar$  and  $\Delta_1' = \Delta_1 - \epsilon_{\text{col}} / \hbar + \delta_1$ . Here  $\gamma_1$  denotes the decay rate of the upper molecular state for all possible decay channels,  $\delta_1 \cdot \hbar$  corresponds to the light shift of the molecular level  $|1\rangle$  induced by laser 1, the stimulated rate  $\gamma_{\text{stim}}$  is described in detail in the theoretical part of the one-color PA, and

$$\Omega_{12} = \frac{1}{\hbar} \langle 1 | V_{\text{opt}}^{(2)} | 2 \rangle \quad (3.2)$$

is the molecular Rabi frequency between states  $|1\rangle$  and  $|2\rangle$  by laser 2, with  $V_{\text{opt}}^{(i)} \cos(\omega_i t) = -\mathbf{d}(R) \cdot \mathbf{E}_i(t)$ , where  $\mathbf{d}(R)$  denotes the molecular transition dipole operator and  $E_i = \sqrt{2I_i / \epsilon_0 c}$  the amplitude of the electric field of the laser ( $i$ ):  $\mathbf{E}_i(t) = E_i \cos(\omega_i t)$ . The experimental measurement of the Rabi frequency is described in Sect. 3.2.5.

The inelastic loss rate coefficient  $K_{\text{in}}$  for a thermal atomic cloud can be calculated on the basis of this scattering matrix element  $S_{\epsilon 1}$  by integration over all individual spectral lines weighted by the Boltzmann distribution as follow [Boh99]:

$$\langle K_{\text{in}}(\Delta_1, \Delta_2) \rangle_{\text{T}} = \frac{1}{hQ} \int_{\epsilon_{\text{col}}=0}^{\infty} d\epsilon |S_{\epsilon 1}|^2 \exp\left(-\frac{\epsilon_{\text{col}}}{k_{\text{B}}T}\right) \quad (3.3)$$

where  $Q_T = \left(\frac{2\pi\mu kT}{h^2}\right)^{3/2}$  is the partition function for the atomic cloud at temperature  $T$  and  $\mu$  is the reduced mass of the molecule.

In contrast to the one-color PA the Doppler broadening of the individual two-color PA-lines is less than 1 Hz and thus completely negligible. In the experiment the PA beams are coming from the same direction cancelling Doppler shifts due to the difference from the absorption and emitting of the two photons. Therefore no Doppler effect is included in the calculated PA lines.

Thus, assume that all molecules photoassociated to state  $|1\rangle$  will decay to unbound atom pairs with enough energy to leave the dipole trap, comparable to the one-color PA. The total loss of atoms can be described by the differential equation

$$\dot{\rho} = -\alpha\rho - 2\langle K_{\text{in}} \rangle_{\text{T}}\rho^2, \quad (3.4)$$

where  $\rho$  denotes the local density of atoms inside the trap,  $\alpha$  the loss rate from collisions with background gas and  $K$  the loss rate for PA-induced losses. In our experiment only short irradiation times  $\tau$  compared to the unperturbed trap lifetime  $\alpha^{-1}$  were used, thus inelastic scattering with background gas can be neglected i.e.  $\alpha \approx 0$ . Comparable to one-color PA the theoretical two-body loss coefficient  $\beta$  can be calculated from  $\langle K_{\text{in}} \rangle_{\text{T}}$  by the same conversion Eq. 2.37.

## 3.2 Measurement of PA lines in $X^1\Sigma_{\text{g}}^+$ of $\text{Ca}_2$

### 3.2.1 Experiment

The ultracold calcium atomic cloud is prepared at a temperature of about  $1 \mu\text{K}$  in UHV of about  $2 \cdot 10^{-10}$  mbar following the cooling scheme described in Sec. 2.2. The calcium atoms conserved in the DT are irradiated by two linear polarized laser beams coming from same single-mode optical fibre to guarantee that the beams stay well overlapped and that they come from the same direction.

To specify the quantisation axis of the transition a magnetic field  $B = 0.263$  mT is applied parallel to the polarization of the PA lasers light. Due to the Zeemann

splitting of the intermediate state this condition additionally ensures that only the desired transition to  $M=0$  component are induced.

The irradiation durations of 200 ms were typically used for the PA spectroscopy in Raman configuration.

The two-color PA spectra of the four least bound rovibrational states ( $v, J$ ) in the potential  $X^1\Sigma_g^+$  are observed. Depending on the better transition rate the bound states  $v' = -1$  in  $(a, c)1_u$  or  $v' = -1$  in  $c0_u^+$  were used as the intermediate states. The precise positions of these intermediate states were taken from [Kah14b]. During the measurement the laser 1 was detuned by either  $\Delta_1 \approx +1$  MHz or  $-1$  MHz from the intermediate state (see Tab. 3.2).

### 3.2.2 Observed PA lines

To reduce the analysis time of the measured PA spectra the theoretical line profile was approximated according to Eq. 3.3 for the Raman scheme.

The matrix element  $|S_{e1}|^2$  has two extrema: a minimum at  $\Delta'_2 = 0$  and a maximum at  $\Delta'_2 = \frac{\Omega_{12}^2}{\Delta_1}$ , where the individual spectral line for a collision energy  $\epsilon$  is located. Expressing Eq.3.3 in terms of the detuning from this maximum, i.e.  $\Delta''_2 = \Delta'_2 - \frac{\Omega_{12}^2}{\Delta_1}$  and assuming to stay in the vicinity of the maximum far away from the minimum ( $\Delta''_2 \ll \frac{\Omega_{12}^2}{\Delta_1}$ ), the individual line shapes for a fixed collision energies can be approximated by a Lorentzian:

$$|S_{e1}(\Delta_2)|^2 \approx \frac{A}{(\Delta_2 - \delta_{\text{shift}})^2 + (\Gamma_L/2)^2} \quad (3.5)$$

with parameters  $A$ ,  $\delta_{\text{shift}}$ ,  $\Gamma_L$  that can be related to the experimental parameters:

$$\Gamma_L = \frac{\Omega_{12}^2(\gamma_{\text{stim}} + \gamma_1)}{4(\Delta_1 - \epsilon_{\text{col}}/\hbar + \delta_1)^2}, \quad (3.6)$$

$$\delta_{\text{shift}} = \epsilon_{\text{col}}/\hbar - \frac{\Omega_{12}^2}{4(\Delta_1 - \epsilon_{\text{col}}/\hbar + \delta_1)}, \quad (3.7)$$

$$A = \frac{\gamma_{\text{stim}}\gamma_1\Omega_{12}^4}{16(\Delta_1 - \epsilon_{\text{col}}/\hbar + \delta_1)^4}. \quad (3.8)$$

According to the Wigner threshold law the stimulated width is depending on  $\epsilon_{\text{col}}$  as  $\gamma_{\text{stim}} = 2l_{\text{opt}}\gamma_1k \propto \sqrt{\epsilon_{\text{col}}}$  [Wig48]. Under the experimental conditions, where  $\Delta_1$  is

much larger than  $\gamma_1, \gamma_{\text{stim}}$  and  $\Omega_{12}$ , the deviation between the Lorentzian and the true individual line shape is only marginal and thus can be neglected when performing the thermal averaging over collision energies  $\epsilon_{\text{col}}$ . Furthermore, in the fit the shift connected with the collision energy  $\epsilon_{\text{col}}$  of Eqs. 3.6, 3.7, 3.8 is neglected in the denominator, because its contribution is small compared to  $\Delta_1 + \delta_1$ .

These approximations allow an efficient modeling of the thermally broadened measured spectra. Similar to one-color PA [Jon99], during the fit routine the integral of the thermal average (Eq. 3.3) is approximated by a sum of spectral lines evenly spaced by  $\delta\epsilon \approx h\Gamma_L/3$ :

$$\langle K_{\text{in}} \rangle_{\text{T}} \approx \sum_{i=0}^n e^{-i \cdot \delta\epsilon_{\text{col}}/k_{\text{B}}T} |S_{\epsilon 1}|^2 \delta\epsilon_{\text{col}} \quad (3.9)$$

and leads to the thermal averaged two-body loss coefficient

$$\langle \beta \rangle_{\text{T}} = A^{\text{eff}} \sum_{i=0}^n e^{-i \cdot \delta\epsilon_{\text{col}}/k_{\text{B}}T} \frac{\sqrt{i \cdot \delta\epsilon_{\text{col}}}}{(\Delta_2 - i \cdot \delta\epsilon_{\text{col}} - \nu_0)^2 + \left(\frac{\Gamma_L}{2}\right)^2} \delta\epsilon_{\text{col}}. \quad (3.10)$$

The number  $n$  of individual lines  $i$  was chosen to be large enough to cover the entire line profile. The parameter  $A^{\text{eff}}$  in the Eq. 3.10 describes combined scaling of the theoretical profiles to the recorded spectra and correlates with parameter  $A$  in Eq. 3.8,  $\nu_0$  is the resonance position inclusive laser light shifts.

During the fitting the  $\sqrt{\epsilon}$  dependency of the  $\gamma_{\text{stim}} = 2l_{\text{opt}}\gamma_1 \frac{\sqrt{2\mu\epsilon}}{\hbar}$  with  $\gamma_1 = 2\gamma_a$  in the Eq. 3.6 leads to non-physical values of the fit parameter  $\{l_{\text{opt}}, T, \Omega_{12}\}$ , thus the energy independent  $\Gamma_L$  was used. With the energy independent  $\Gamma_L$  it was possible to fit the measured PA line much better. This behaviour points towards a larger width of the excited state  $\gamma_1$ . A similar effect of enlarged molecular decay rates has been reported for PA spectra of  $^{88}\text{Sr}$  [Zel06]. Therefore the energy independent  $\Gamma_L$  was taken into account.

Three spectra of the most weakly bound state  $v = 40; J = 0$  in  $X^1\Sigma_g^+$ , where  $J$  denotes the total angular momentum of the state, for different experimental parameters and their respective fitted lines shapes are shown in the top of Fig. 3.2. All spectra were taken at a temperature of  $T = 1.15 \mu\text{K}$  determined from time-of-flight measurements. The level  $v = -1; \Omega = 0$  has been used as the intermediate level in the Raman configuration with the large detuning  $\Delta_1 \approx +1 \text{ MHz}$ . The observed spectral lines

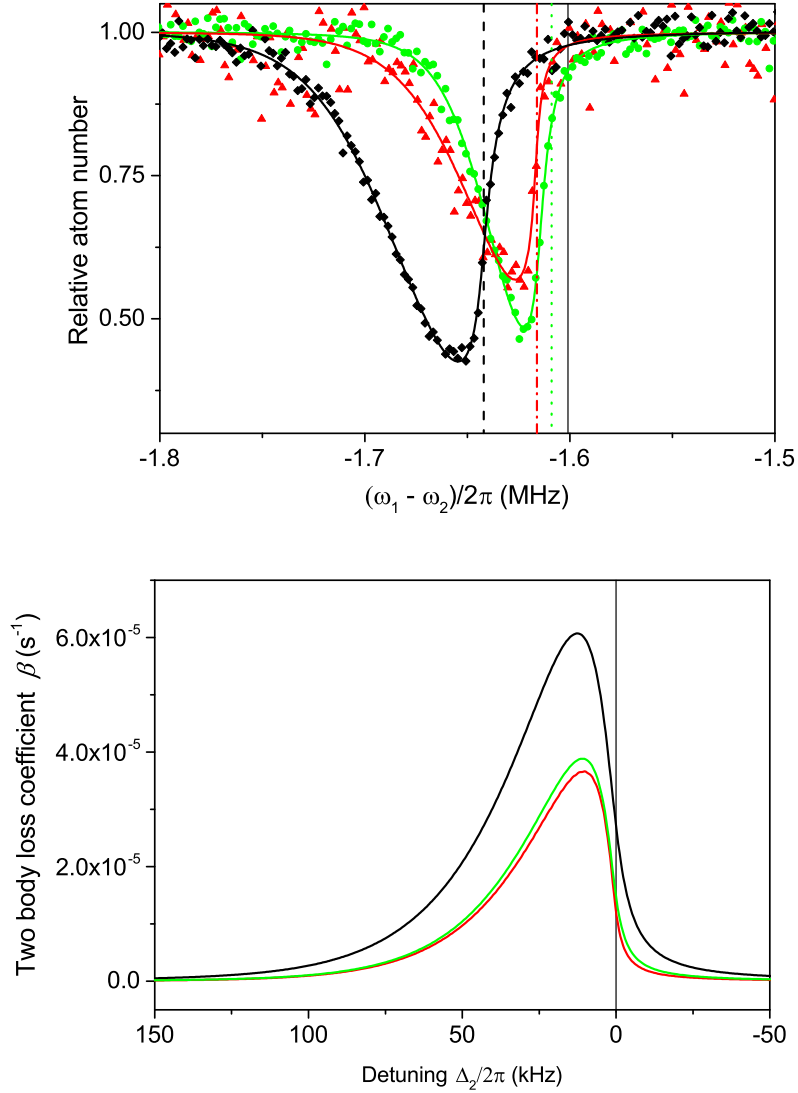


Figure 3.2: Top: atom loss from the crossed dipole trap due to two-color PA as a function of the difference of the two laser frequencies for the most weakly bound molecular state in the ground state potential  $X^1\Sigma_g^+$   $v = 40$ ;  $J = 0$  using  $v' = -1$ ;  $\Omega = 0$  as the intermediate level. Spectra for three different PA-intensities are shown together with their respective fit curves and their derived resonance positions indicated by vertical lines. The green dots, black diamonds, red triangles correspond to  $I_1 = (45, 118, 45) \text{ Wcm}^{-2}$ ,  $I_2 = (18, 18, 14) \text{ Wcm}^{-2}$  and the dotted, dashed, and dash-dotted lines, respectively. The solid line at -1.601 MHz indicates the unperturbed binding energy. All measurements were performed at a temperature  $T$  of  $\approx 1 \mu\text{K}$ . The bottom Fig. shows the spectra of the corresponding loss coefficients  $\beta$  as a function of the detuning  $\Delta_2$  calculated according to Eq. 3.10

$I_1$ (Wcm $^{-2}$ ), $I_2$ (Wcm $^{-2}$ )	$\nu_0$ (kHz)	$\Gamma_L$ (kHz)	$A^{\text{eff}}$ ( $\frac{m^3}{10^{60} \text{J}^{3/2} \text{s}}$ )	T ( $\mu\text{K}$ )	$\Gamma^{\text{calc}}L$ (kHz)
45, 18 (green curve)	-1609	6.0	1.7	0.81	3.4
118, 18 (black curve)	-1642	9.3	4.8	0.87	8.8
45, 14 (red curve)	-1616	4.6	1.0	0.83	2.6

Table 3.1: The fit parameters to the measured PA spectra shown in Fig. 3.2 and  $\Gamma^{\text{calc}}L$  calculated for  $\epsilon_{\text{col}}/k_B = 1 \mu\text{K}$  according to 3.6 assuming  $\delta_1 = 0$ .

show the typical asymmetric thermal broadening that is a characteristic feature of photoassociation spectra, when the Doppler broadening is much lower than the thermal broadening.

The influences of the laser intensities on the individual spectral lines can be observed from the corresponding loss coefficients  $\beta$  in the dependency of the detuning  $\Delta_2$  (see 3.2).

The black (diamonds, dashed line) and green (circles, two dot dashed line) spectra were obtained by two different intensities  $I_1$  of the free-bound transition laser. The higher free-bound PA intensity during the measurement of the black curve leads to the change of the position  $\nu_0$  corresponding to the ac-Stark shift resulting from the laser 1, which is contained in  $\Delta'_1$  in the Eq. 3.7. The corresponding fitted linewidths  $\Gamma_L$  (see Tab. 3.1) increase from 6.0 kHz to 9.3 kHz while the fit temperature remains nearly constant. The change of the fit widths  $\Gamma_L$  can be explained by the increasing of the stimulated rate  $\gamma_{\text{stim}}$  from 13 kHz to 34 kHz due to the increasing of intensity  $I_1$ . The behaviour is confirmed with the variation described in Eq. 3.6, where the increasing of  $\gamma_{\text{stim}}$  leads to the larger  $\Gamma_L$ . In the same way the  $A^{\text{eff}}$  increases by a factor about  $\frac{4.8}{1.7} \approx 2.8$  though the increase of  $\gamma_{\text{stim}}$  by  $\frac{34}{17} \approx 2.0$ , this is connected to the linearity of the  $\gamma_{\text{stim}}$  in Eq. 3.8.

In the same way a decrease of bound-bound laser intensity  $I_2$ , which is connected with the Rabi frequency  $\Omega_{12}$ , leads to the lowering of the  $\Gamma_L$  from 6.0 kHz to 4.6 kHz. This behaviour is reproduced by decreasing of  $\Omega_{12}$  from 525 kHz to 464 kHz in the Eq. 3.6. The parameter  $A^{\text{eff}}$  decreased by  $\frac{1}{1.7} \approx 0.59$  is comparable to the factor  $(\frac{464}{525})^4 \approx 0.61$  calculated from the  $\Omega_{12}$ . This fact reflects, that the  $B$  loss parameter increases with the forth power of  $\Omega_{12}$  as shown in Eq. 3.8.

Generally the fit parameters reproduce the theoretical behaviour for individual PA linewidth and PA rates. The width  $\Gamma_L$  of individual lines for fixed energy  $\epsilon$  are comparable to the theoretical model Eq. 3.6 with the values extracted from fitting the

spectra.

The sample temperature determined by the fit is always underestimated by about 20%. Fortunately, the resonance position determined by the fit is very robust against changes in the fit parameters  $\Gamma_L, \delta, B, T$  and is mostly determined by the steep edge, that is only a few kHz wide (see Fig. 3.2). Thus the  $\nu_0$  resonance position of the molecular level is determined with high reliability. To use the fitted resonance positions  $\nu_0$  for the zero-intensity extrapolation their uncertainties were estimated by the following procedure. One after another the fitting parameters were individually set constant. To these values the fitting routine estimated the maximal corresponding shifts of the resonance position  $\nu_0$ . The parameter was varied until its realistic individual uncertainty was determined. Subsequently the total uncertainty of every resonances  $\nu_0$  was estimated as sum of all shifts induced by the fitting parameters.

### 3.2.3 Unperturbed binding energies

To determine the binding energy  $\Delta_b^{\text{exp}}$  of the unperturbed states the measured PA spectra were corrected for the thermal shift and the shifts due to the ac-Stark effect of all involved lasers: free-bound laser, bound-bound laser and dipole trap laser. The shifts were independently derived from the measurements of the resonance positions  $\nu_0$  by usage of the above described fitting routine at different intensities. These shifts were subsequently extrapolated to zero intensity as shown in Figs. 3.3-3.6.

The PA laser intensities used in the measurement were determined as described in the Sect. 2.2.4 according to Eq. 2.60.

In Figs. 3.3-3.6 the experimentally measured resonance positions indicated as the black circles were weighted with the uncertainties derived using the above described procedure. The zero-intensity position  $\nu_{0,n}$  and the shift  $b_n$  were derived from the linear regression

$$\nu_n(I_n) = \nu_{0,n} + b_n \cdot I_n \quad (3.11)$$

indicated by the red lines, where  $n$  is laser 1, 2 or DT, and  $I_n$  and  $b_n$  are the intensity and the slope for the ac-Stark shift of the corresponding laser  $n$ , respectively. The corresponding  $1-\sigma$  region along the extrapolation is calculated from the covariance matrix of the fit [GUM08]:

$$\sigma_\nu^2(I_n) = \sigma_{\nu_{0,n}}^2 + I_n^2 \cdot \sigma_{b_n}^2 + 2 \cdot I_n \cdot \text{Cov}(\nu_{0,n}, b_n). \quad (3.12)$$

The zero-intensities positions  $\nu_{0,n}$  and corresponding slopes  $b_n$  were used to calculate the position  ${}^1\nu_0$  of the unperturbed state as follows:

$${}^1\nu_0 = \nu_{0,1} + b_2 I_2 + b_{\text{DT}} I_{\text{DT}}. \quad (3.13)$$

From the data, the extrapolation to zero intensity of the lasers can be performed in different orders:

$$1. \quad {}^1\nu_0 = \nu_{0,1} + b_2 I_2 + b_{\text{DT}} I_{\text{DT}} \quad (3.14)$$

$$2. \quad {}^2\nu_0 = \nu_{0,2} + b_1 I_1 + b_{\text{DT}} I_{\text{DT}} \quad (3.15)$$

$$3. \quad {}^3\nu_0 = \nu_{0,\text{DT}} + b_1 I_1 + b_2 I_2. \quad (3.16)$$

Therefore the final position  $\Delta_b$  of one line was taken as the arithmetic mean value

$$\Delta_b = \frac{{}^1\nu_0 + {}^2\nu_0 + {}^3\nu_0}{3}. \quad (3.17)$$

and the final uncertainty  $\sigma_{\text{total}}$  of the state as

$$\sigma_b = \sqrt{{}^1\sigma_{\nu_{0,1}}^2 + {}^2\sigma_{\nu_{0,1}}^2 + {}^{\text{DT}}\sigma_{\nu_{0,1}}^2} \quad (3.18)$$

from the uncertainties  $\sigma_a$  determined from the linear regressions.

The final position  $\Delta_b$  of the  $v = 38$   $J = 2$  and  $v = 40$   $J = 0$  were determined using a single set of measurements (see Tab. 3.2)

The final positions of  $v = 39$   $J = 0$  and  $v = 39$   $J = 2$  were measured several times. Therefore these final positions  ${}^n\Delta_b$  were additionally averaged weighted regarding their uncertainties  $\sigma_{b,n}$ :

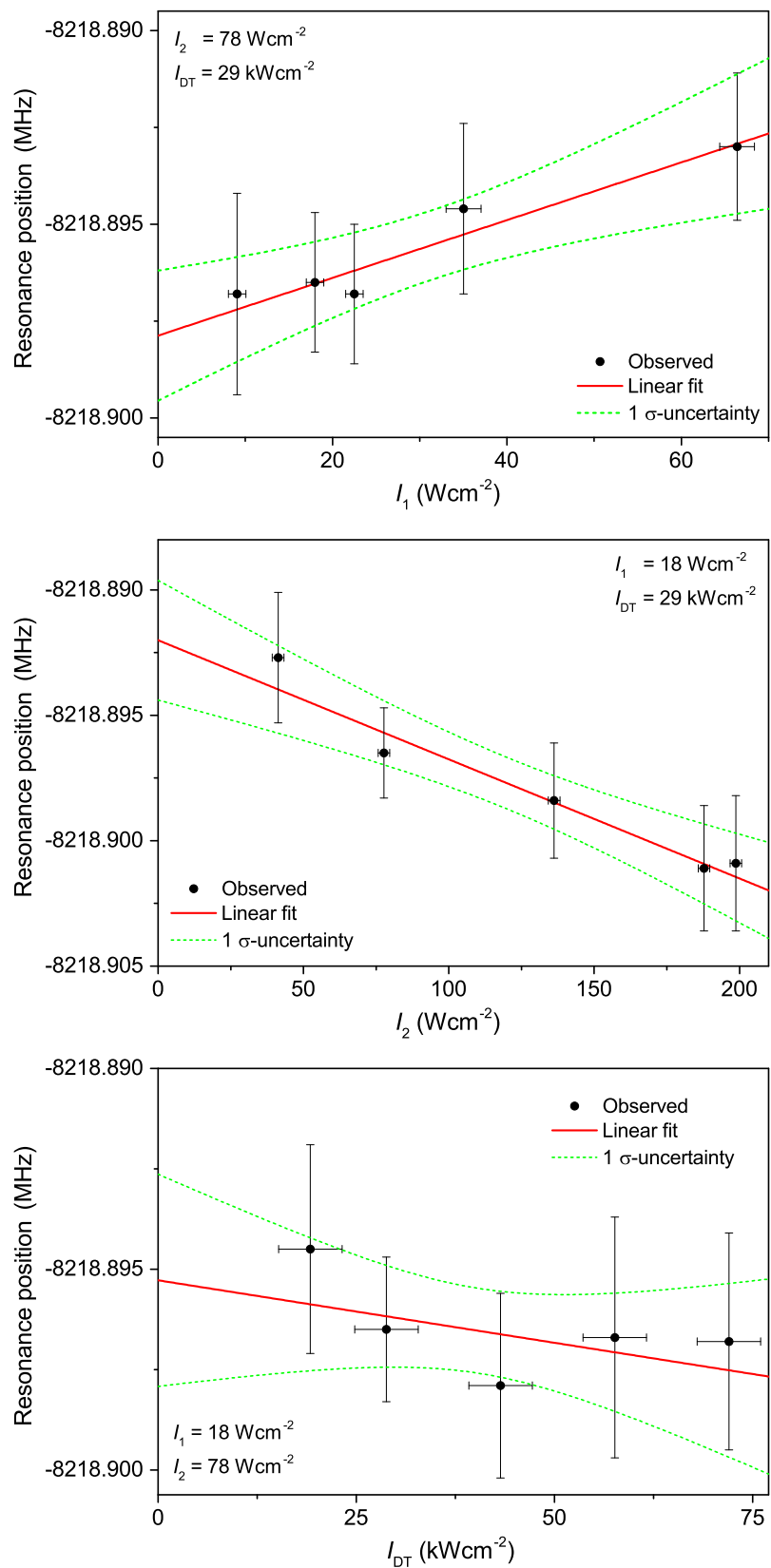
$$\Delta_b = \frac{\sum_n {}^n\Delta_b / \sigma_{b,n}^2}{\sum_n 1 / \sigma_{b,n}^2} \quad (3.19)$$

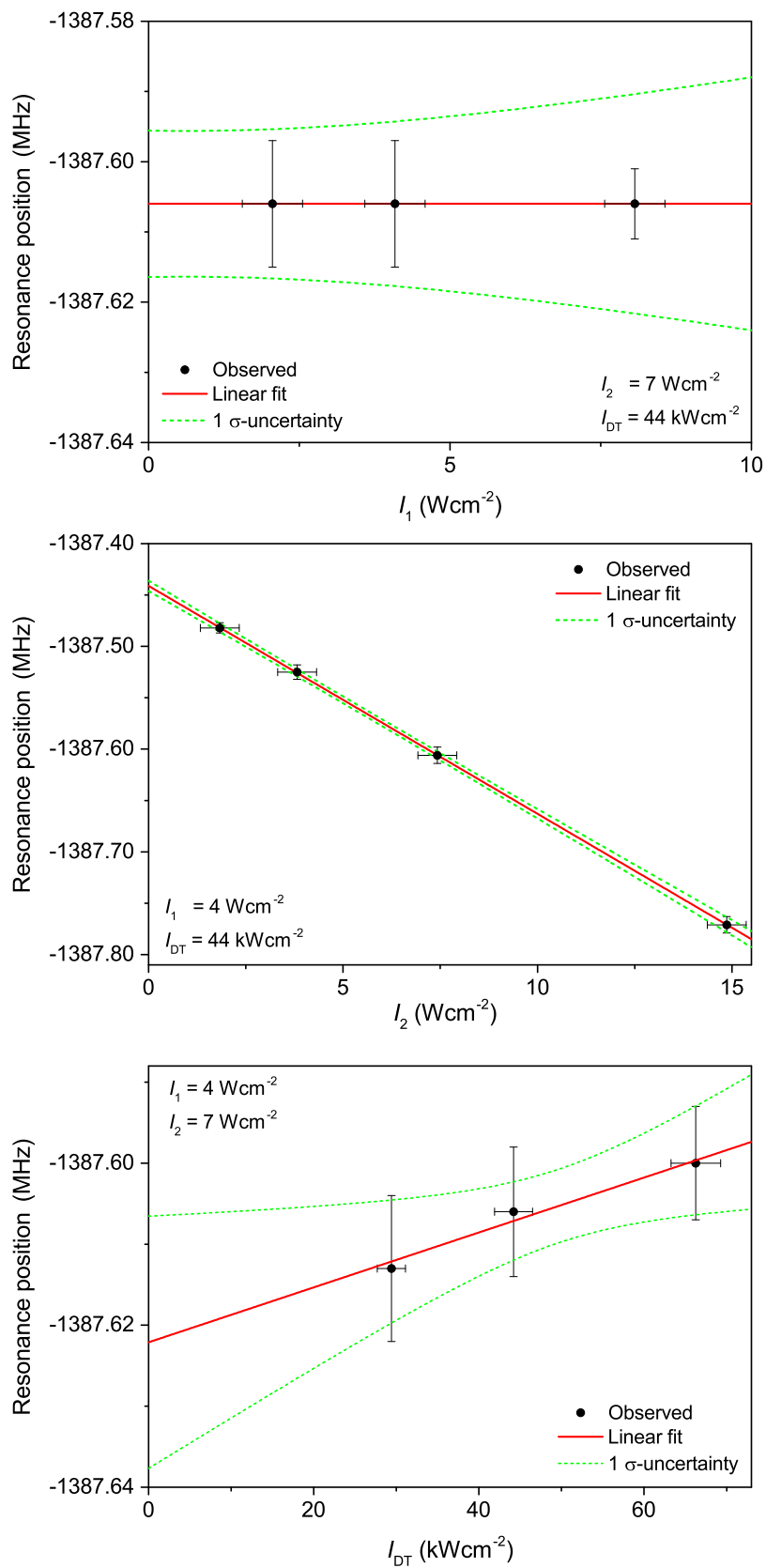
$$\sigma_b = \left( \sqrt{\sum_n 1 / \sigma_{b,n}^2} \right)^{-1} \quad (3.20)$$

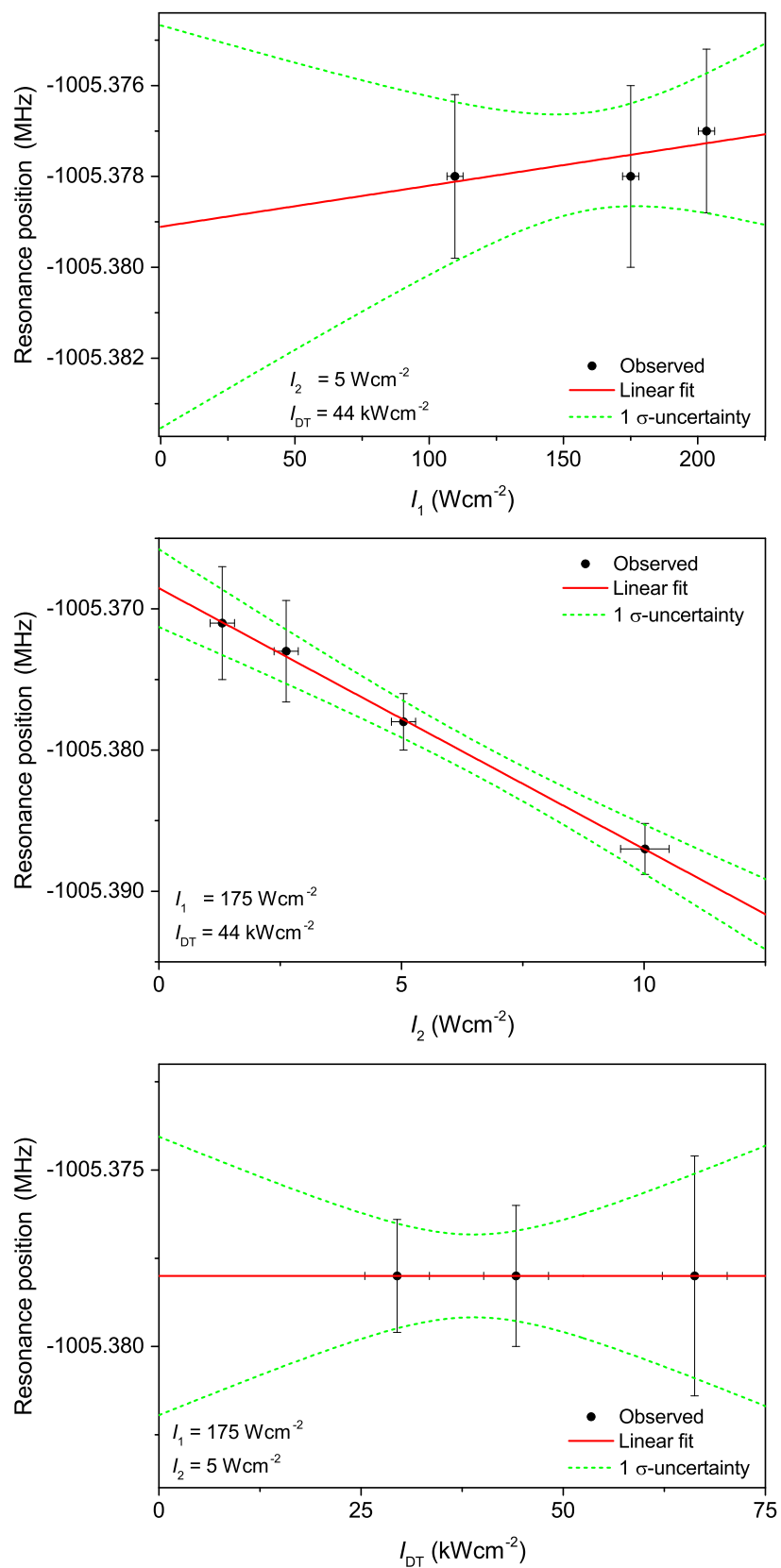


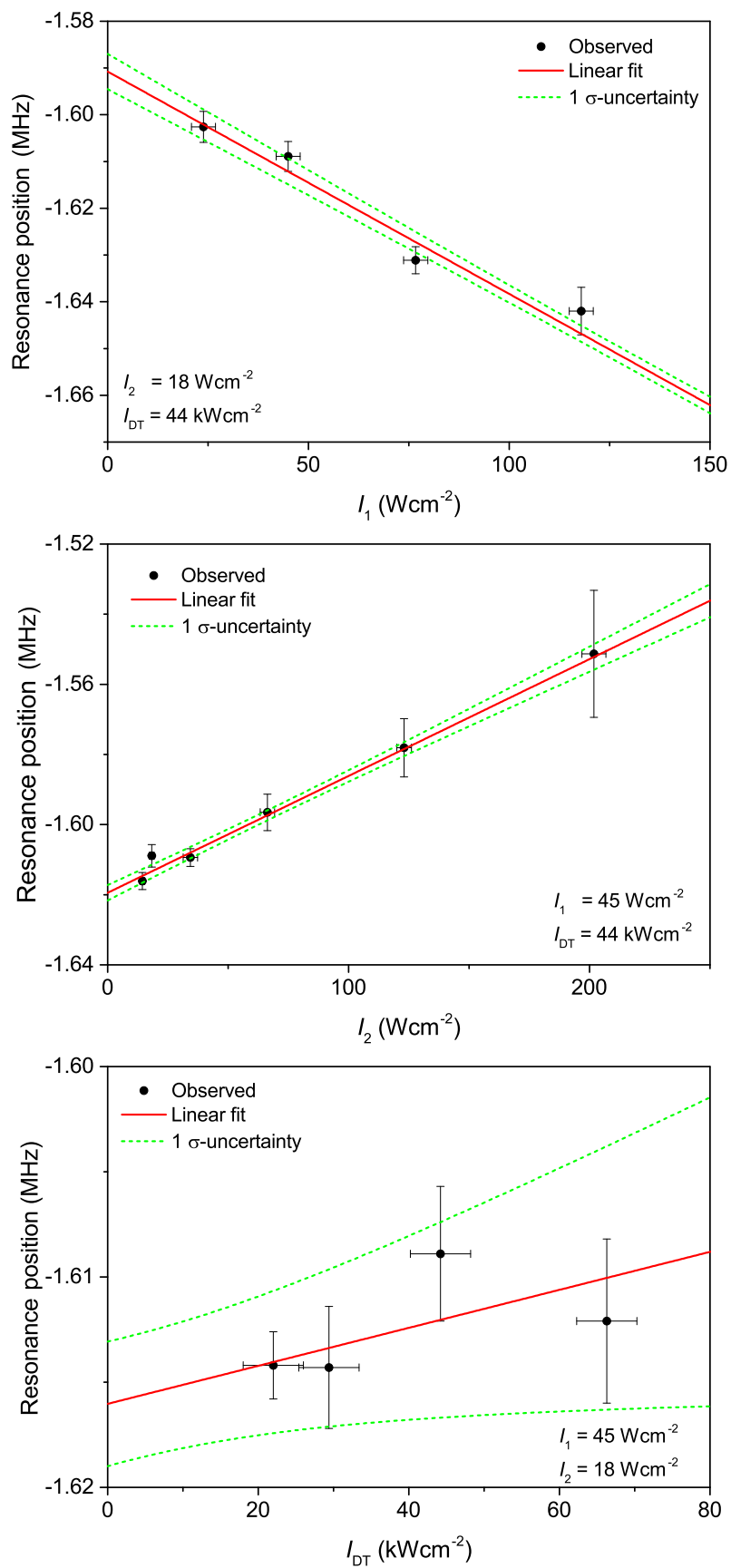
bound level	$v = 38 J = 2$	$v = 39 J = 0$		$v = 39 J = 2$			$v = 40 J = 0$
FCD $_{\epsilon 1}$ ( $1/\text{cm}^{-1}$ )	13.38	4.38		4.38			13.38
FCF $_{12}$ (dimensionless)	0.008	0.54		0.15			0.019
intermediate state	$v'=-1 \Omega=0$	$v'=-1 \Omega=1$	$v'=-1 \Omega=1$	$v'=-1 \Omega=1$	$v'=-1 \Omega=1$	$v'=-1 \Omega=1$	$v'=-1 \Omega=0$
detuning $\Delta_1(2\pi)^{-1}$	-1 101(10)	-1 001(10)	1 016(10)	-1 001(10)	-924(10)	+900(10)	+978(10)
ac Stark free-bound laser	-1(4)	0(10)	-1(6)	-2(3)	0(5)	-24(24)	22(4)
ac Stark bound-bound laser	4(2)	165(5)	-242(5)	9(3)	15(3)	-10(2)	-6(2)
ac Stark dipole trap	1(3)	-17(17)	-5(4)	0(4)	0(6)	0(6)	-3(3)
extrapolated position	-8 218 897(4)	-1 387 457(20)	-1 387 439(9)	-1 005 369(6)	-1 005 361(7)	-1 005 379(24)	-1 601(6)
weighted average	-8 218 897(4)	-1 387 442(8)		-1 005 366(5)			-1 601(6)
discrepancy of temperatures	0(2)	0(2)		0(2)			0(2)
power measurements	0.0(7)	0.0(7)		0.0(7)			0.0(7)
detuning $\Delta_1$	0(1)	0(1)		0(1)			0(1)
unperturbed energy $\Delta_b^{\text{exp}}(2\pi)^{-1}$	-8 218 897(5)	-1 387 442(9)		-1 005 366(6)			-1 601(7)
calc. energy $\Delta_{\text{calc}}(2\pi)^{-1}$	-8 218 896	-1 387 437		-1 005 372			-1 599

Table 3.2: Weighted averages with their statistical uncertainties are obtained by extrapolations of ac Stark shifts of free-bound (fb), bound-bound (bb) and dipole trap (DT) lasers to zero intensity at detuning  $\Delta_1$  to intermediate state. The important additional systematics are listed under the averages. The unperturbed binding energies  $\hbar\Delta_b^{\text{exp}}$  including statistic and systematic uncertainties close the table. These values are in kHz. Additionally the Franck-Condon density (FCD $_{\epsilon 1}$  ( $\epsilon_{\text{col}}/k_B = 1 \mu\text{K}$ )) of the used intermediate state and Franck-Condon factor (FCF $_{12}$ ) between the intermediate state in the excited potential and bound states in the ground potential are listed.

Figure 3.3:  $v = 38 \ J = 2$

Figure 3.4:  $v = 39, J = 0$

Figure 3.5:  $v = 39, J = 2$

Figure 3.6:  $v = 40 J = 0$

The ac Stark shift by laser 2 according to Eq. 3.7 depends on the detuning  $\Delta_1$  from the intermediate state. For the measurement of the resonance in ground state  $X^1\Sigma_g^+$  the  $\Delta_1$  was taken more than 750 kHz to minimize its influence on the resonance position. In the multiple measurements  $\Delta_1(2\pi)^{-1}$  was in the range  $\pm(400-1000)$  kHz leading to an additional uncertainty of 1 kHz.

As mentioned above, the temperatures determined by the fit routine are smaller compared to the measured TOF temperatures and in general the differences are in the range of 20 %. The uncertainty considered with this deviation was estimated as  $0.1 \cdot \epsilon_{\text{col}}/\hbar \approx 2$  kHz.

Additional uncertainty contributed by sources of technical nature is estimated to 3 kHz. Among these are the nonlinearities of the atom number estimation from the absorption imaging, variations of dipole trap power and the ramp procedure for the evaporation cooling, residual contributions of unwanted frequencies stemming from the offset-locking of the spectroscopy lasers and residual magnetic fields.

The Franck-Condon densities and the Franck-Condon factors listed in second and third row of Tab. 3.2 correspond to coupling strengths of the free-bound and bound-bound transitions. The large Franck-Condon density of the transition from continuum to  $v' = -1$  in  $c0_u^+$  used in the measurements of  $v = 38$   $J = 2$  and  $v = 40$   $J = 0$  correlates with the large ac Stark shifts of free-bound laser. The large FCF of transition  $v' = -1$  in  $(a, c)1_u$  to  $v = 39$   $J = 0$  of  $X^1\Sigma_g^+$  correlates with the large shifts of bound-bound laser.

### 3.2.4 Molecular potentials

The calculations of the molecular potentials needed for the prediction of binding energies, calculating Franck-Condon densities (FCD) in Eq. 2.21, and modeling bound-bound transitions with appropriate Franck-Condon factors (FCF) were performed by Prof. Eberhard Tiemann.

As described in Sect. 2.1.1 the vibrational levels are represented by a multi-component wave function described by the Hund's case (e) basis  $|^1S_0 + ^3P_j, l, J\rangle$ , with the total atomic angular momentum  $j$ ,  $l$  the angular momentum of the pair rotation and  $J$  the total angular momentum.

$$|{}^1S_0 + {}^3P_1, 0, 1\rangle, \quad (3.21)$$

$$|{}^1S_0 + {}^3P_1, 2, 1\rangle, \quad (3.22)$$

$$\text{and } |{}^1S_0 + {}^3P_2, 2, 1\rangle. \quad (3.23)$$

Because of the electric dipole selection rule  $\Delta l = 0$  from these basis states only the component  $|{}^1S_0 + {}^3P_1, 0, 1\rangle$  is needed for the calculation of the Franck-Condon densities with the continuum  $|{}^1S_0 + {}^1S_0, 0, 0\rangle$  and the two first components for the Franck-Condon factors with the bound levels  $|{}^1S_0 + {}^1S_0, 0, 0\rangle$  or  $|{}^1S_0 + {}^1S_0, 2, 2\rangle$ .

The molecular ground state potential X<sup>1</sup>Σ<sub>g</sub><sup>+</sup> is based on spectroscopic measurements by [All03] for the short range part and on the new data for the long range branch as described by the conventional power expansion in  $1/R$

$$V_X = -f_6(R) \frac{C_6}{R^6} - \frac{C_8}{R^8} - \frac{C_{10}}{R^{10}}. \quad (3.24)$$

By the function  $f_6(R)$  the retardation correction as calculated by Moszynski *et al.* [Mos03] is applied, which turned out to be essential for describing the asymptotic levels within their experimental uncertainty. This correction is only significant to the first term in the equation due to the very long range nature of the van der Waals interaction. An additional exchange term is regularly used in the mathematical representation of the long range potential. Such term is not needed for the description in this case, due to the van der Waals term being large compared to a possible exchange energy in the range  $R > 1.1$  nm in which Eq. 3.24 is applied.

In a least squares fit of all known data for the ground state (in total 3586 data points) the long range parameters were varied including as additional condition the theoretical coefficients  $C_i$  for  $i = 6, 8, 10$  [Por02, Por06, Mit08, Ciu04] applying their estimated uncertainties from the calculation as weights in the fit. The fit reveals in total a normalized standard deviation  $\sigma = 0.76$ , a good fit should result to values close to one, if the applied uncertainties are well justified and the theoretical model is appropriate. Thus this is a very satisfactory result. In detail, the spectroscopic data from [All03] are represented within their respective experimental uncertainty, and the binding energies of the asymptotic levels in the last line of Tab. 3.2 are within their assumed uncertainties, only level  $v = 39, J = 2$  touches the upper edge. The derived long range parameters are shown in Tab. 3.3 and are compared with earlier results from experiment and theory. With this improved potential representation the uncertainty

ref.	$C_6$	$C_8$	$C_{10}$
	$10^7 \text{ cm}^{-1} \text{ \AA}^6$	$10^8 \text{ cm}^{-1} \text{ \AA}^8$	$10^9 \text{ cm}^{-1} \text{ \AA}^{10}$
[All03]	1.0023	3.808	5.06
[Ciu04]	1.003		
[Por06]	1.022	3.010	8.057
[Mit08]	1.055	3.060	8.344
this work	1.0348	2.997	10.88

Table 3.3: Comparison of long range parameters at the asymptote  $^1S_0 + ^1S_0$  derived in this work with experimental results from Allard *et al.* [All03] and theoretical results from Ciuryło *et al.* [Ciu04], Porsev *et al.* [Por06] and Mitroy and Zhang [Mit08]

Method	$a/a_0$
molecular spectroscopy [All03]	200 - 800
$^1S_0 + ^1P_1$ photoassociation [Vog07]	340 - 700
BEC mean field [Kra09]	$\approx 440$
this work	308.5 (50)

Table 3.4:  $^1S_0 + ^1S_0$  scattering length  $a$  of  $^{40}\text{Ca}$  in comparison with experimental results,  $a_0 \approx 53 \text{ pm}$  denotes the Bohr radius

of the calculated scattering length  $a = 308.5(50)a_0$  decreases by more than a factor of 10 compared to former results (Tab. 3.4). The remaining uncertainty originates to a significant part from the correlation between the long range parameters  $C_6, C_8, C_{10}$ . A much denser set of eigenvalues at the ground state asymptote would be required to break this correlation. Because the last bound state is very close to the asymptote, namely -1.6 MHz, one could try to estimate the scattering length  $a$  from a simple relation between binding energy and scattering length [Gri93]

$$a = \bar{a} + \frac{\hbar}{\sqrt{2\mu E_b}}, \quad (3.25)$$

where  $\bar{a}$  is the background scattering length,  $\mu$  the molecular reduced mass and  $E_b$  the binding energy.  $\bar{a}$  depends on the long range form of the potential, namely  $C_6$  and if the value  $\bar{a}$  is small compared to the expected scattering length, i.e. the binding energy is sufficiently small, the scattering length can be directly determined by the binding energy with good approximation. Using the  $C_6$  value from Tab. 3.4 one calculates



$\bar{a} = 53.4 a_0$ , which does not justify to only apply the second part of Eq. 3.25. The full equation results in  $a = 291 a_0$  and comes close to the value obtained from the full potential. The difference indicates that the higher order terms in the long range function cannot be neglected.

From mass scaling [Fal07] the scattering length of other natural isotopes of calcium as shown in Tab. 3.5 can be calculated using the full potential of  $X^1\Sigma_g^+$ .

Isotope	$a/a_0$
$^{40}\text{Ca}$	308.5(50)
$^{42}\text{Ca}$	297 (6)
$^{43}\text{Ca}$	43.7 (10)
$^{44}\text{Ca}$	399 (7)
$^{46}\text{Ca}$	1970 (20)
$^{48}\text{Ca}$	-281 (10)

Table 3.5: Scattering length  $a$  of homonuclear pairs for different natural isotopes of calcium,  $a_0 \approx 53$  pm Bohr radius

The newly determined potential was applied to calculate the desired FCD and FCF (see Tab. 3.6) for evaluation of the spectroscopic observations as detailed in Sects. 2.1.1 and 3.1 and the following paragraph.

### 3.2.5 Autler Townes Spectroscopy

For the Autler Townes spectroscopy the bound-bound laser is hold resonant to the bound-bound transition between the excited and ground states. The resonance configuration is achieved when the detuning  $\Delta_2 - \Delta_1 = 0$ . The free-bound laser probes the excited states by tuning across the resonances. Coupled by the resonant laser light the bound states form dressed states, which leads to two PA resonances. They are also called Autler Townes doublet [Aut55] (see Fig. 3.7). Comparable to Eq. 2.12, assuming the molecular dipole matrix element is only weakly depended on the internuclear separation, the bound-bound transition transition matrix element can be calculated

$$|\langle 1|\mathbf{d}(R)|2\rangle|^2 = |\langle 1|\mathbf{d}_{\text{atom}}|2\rangle|^2 f_{\text{ROT}} f_{\text{FC}}, \quad (3.26)$$

The coupling strength between the dressed states is the molecular Rabi frequency, which can be calculated from Eq. 3.2 by using Eq. 3.26 as followed

	$\Omega$	0	1	0	1	0	1
$J_2$	$v_2 \setminus v_1$	-1	-1	-2	-2	-3	-3
0	40	0.02	$< 10^{-2}$	$< 10^{-3}$	$< 10^{-2}$	$< 10^{-3}$	$< 10^{-3}$
2	39	0.38	0.15	0.25	0.04	0.03	0.02
0	39	0.06	0.54	0.12	0.15	0.01	0.04
2	38	$< 10^{-2}$	$< 10^{-4}$	0.23	0.12	0.40	0.13
0	38	$< 10^{-2}$	$< 10^{-2}$	0.07	0.29	0.17	0.33
2	37	$< 10^{-3}$	$< 10^{-6}$	$< 10^{-2}$	$< 10^{-3}$	0.13	0.06
0	37	$< 10^{-3}$	$< 10^{-3}$	$< 10^{-2}$	$< 10^{-2}$	0.05	0.13
cont.		0.53	0.30	0.31	0.39	0.17	0.27

Table 3.6: Calculated Franck-Condon factors  $f_{\text{FCF}}$  for transitions from bound levels ( $v_1, J_1 = 1$ ) of the states  $\Omega = 1_u$  and  $0_u^+$  of the coupled system  $a^3\Sigma_u^+$  and  $c^3\Pi_u$  to bound levels ( $v_2, J_2 = 0, 2$ ) of the ground state  $X^1\Sigma_g^+$ . The last line gives the fraction of excited molecules decaying back to continuum states near the ground state asymptote with  $J = 0, 2$

$$\Omega_{12} = \sqrt{f_{\text{ROT}}}\sqrt{f_{\text{FC}}}\sqrt{\gamma_{\text{atom}}}\sqrt{\frac{I_2}{2\frac{\pi\hbar c}{3\lambda^3}}}, \quad (3.27)$$

where  $\gamma_{\text{atom}}$  is atomic decay rate,  $f_{\text{FCF}} = |\langle 1|2\rangle|^2$  is the Franck-Condon factor giving a measure for the strength of molecular transitions is related to the overlap integral of the wave functions of the bound states using the selection rule for electric dipole transitions to choose the proper component of the multi-component wavefunctions.

For the coupling  $J = 1 - 0$  are

$$\begin{aligned} |1\rangle &= |^1S_0 + ^3P_1, 0, 1\rangle \\ |2\rangle &= |^1S_0 + ^1S_0, 0, 0\rangle \end{aligned}$$

and for the coupling  $J = 1 - 2$  are

$$\begin{aligned} |1\rangle &= |^1S_0 + ^3P_1, 2, 1\rangle \\ |2\rangle &= |^1S_0 + ^1S_0, 2, 2\rangle. \end{aligned}$$

The factor  $f_{\text{ROT}}$  is calculated in the Hund's case (e) basis. With conventional angular momentum algebra [Edm57] for a transition  $|j_1, l_1, J_1, M_1\rangle$  to  $|j_2, l_2, J_2, M_2\rangle$  applying

the decoupling of  $l_{1,2}$  because the electric dipole operator does not act in the rotational space the rotational factor is:

$$f_{\text{ROT}} = (2J_1 + 1)(2J_2 + 1) \begin{Bmatrix} j_1 & J_1 & l_1 \\ J_2 & j_2 & 1 \end{Bmatrix}^2 \begin{pmatrix} J_1 & 1 & J_2 \\ -m_1 & q & -m_2 \end{pmatrix}^2 \cdot 2 \cdot (2j_1 + 1) \cdot \delta(l_1, l_2), \quad (3.28)$$

where  $q = 0, \pm 1$  indicates the polarization of the light field,  $()$  and  $\{\}$  are the conventional Wigner 3j and Wigner 6j symbols, respectively.

For the used two cases with  $\pi$  polarized light and  $M_1 = M_2 = 0$ :

for the coupling  $J = 1 - 0$  is  $f_{\text{FC}} = 2$ ,

and for the coupling  $J = 1 - 2$  is  $f_{\text{FC}} = 4/5$ .

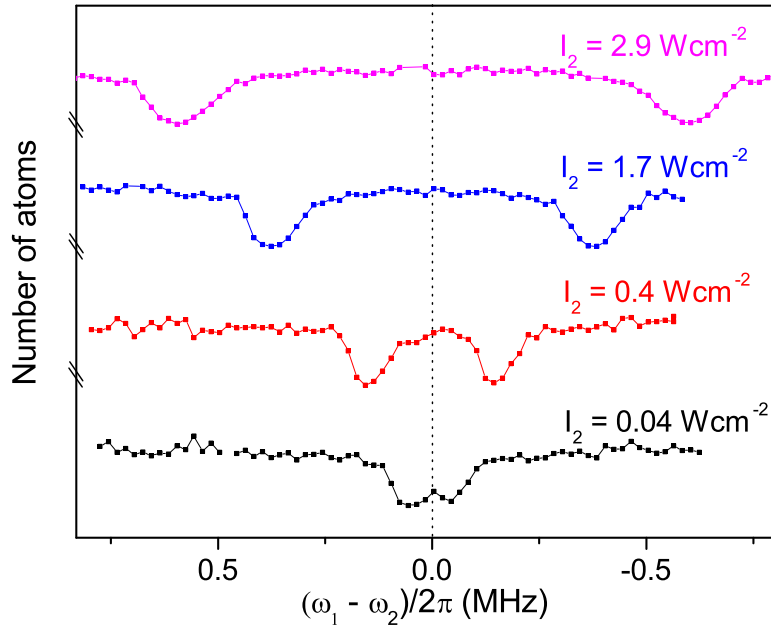


Figure 3.7: Atomic loss spectra when scanning the free-bound PA laser across the  $v' = -1$ ,  $\Omega = 1$  molecular resonance in Autler-Townes configuration for different bound-bound PA laser intensity  $I_2$ . The bound-bound laser was set to be resonant between  $v = 39$ ,  $J = 0$  and the before mentioned excited state.

The recorded spectra are shown in Fig. 3.7. The resonance curves show two features of almost identical amplitude indicating that the second PA-laser was indeed tuned closely to the bound-bound transition, i.e. the detuning was  $\Delta_1 - \Delta_2 \approx 0$  [Boh99].

From the measured splitting we determined the Rabi frequencies for different PA laser intensities, which are plotted as a function of laser intensity  $I_2$  in Fig. 3.8. They are consistent with the fitted square-root behaviour (red solid line). From the experimental

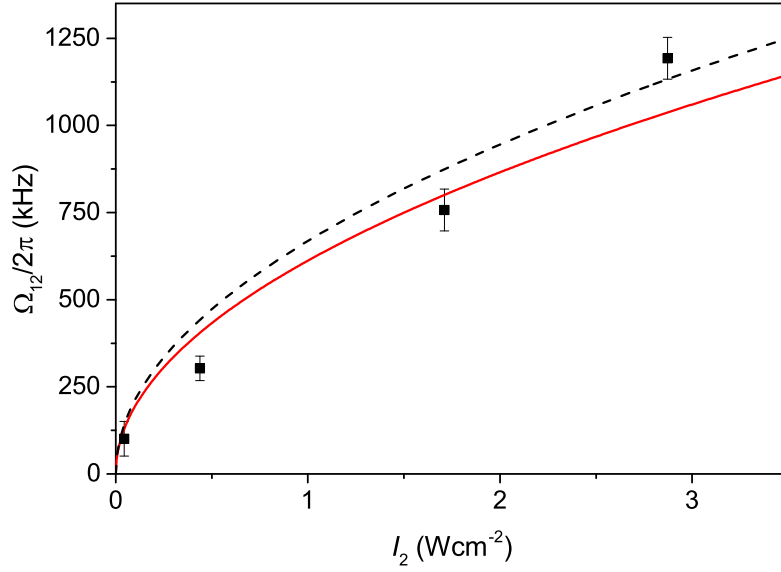


Figure 3.8: Measured molecular Rabi frequencies  $\Omega_{12}$  from Autler-Townes spectra (dots) of the  $v' = -1$  in  $(a, c)1_u$  molecular resonance in dependence of the bound-bound laser intensities  $I_2$ . The black dashed line indicates theoretical expectation following Eq. 3.27 assuming  $f_{\text{fcf, theo}} = 0.54$  determined from molecular potentials while the solid red line is a fit to the data.

values the Franck-Condon factor was determined for a transition from the level  $v_1 = -1$  in  $(a, c)1_u$  to the level  $v_2 = 39$   $J = 0$ . A fit of Eq. 3.28 to the data yields  $f_{\text{FCF, exp}} = 0.45(9)$ , which is in fair agreement with the theoretical prediction  $f_{\text{FCF, theo}} = 0.54$  (see Tab. 3.6). The black dotted line in Fig. 3.8 shows the theoretical values. Both values agree with their combined uncertainties. The deviation could be explained by an additional uncertainty of the absolute intensity of the bound-bound PA laser at the position of the ultracold atoms due to uncertainty from the beam waist measurement and the alignment of dipole trap and focus of the PA-beam or alternatively the assumed molecular transition dipole moment deviates slightly from being  $\sqrt{2}$  times the atomic dipole moment.

The splitting of the Autler-Townes doublet was measured for different intensities  $I_2$  to validate the approximation that the atomic dipole moment governs the molecular transition between these long range levels. From the good agreement between theory and experiment (see Fig. 3.8) I conclude, that other transition probabilities calculated from the new potential are accurate (see Tab. 3.6).

The molecular potentials determined from the ground state binding energies measured in Raman configuration PA and the excited state potentials [Kah14b] can be used for calculating  $f_{\text{FCF, theo}}$  for arbitrary transitions between states close to the excited state

asymptote  ${}^3P_1+{}^1S_0$  and rovibrational states in the ground state potential  $X^1\Sigma_g^+$ . Tab. 3.6 shows a set of calculated values of  $f_{\text{FCF}}$  for those excited states with an appreciable Franck-Condon density  $f_{\text{FCD}}$  between the ground state continuum and the respective excited state, which would be desirable for easy PA spectroscopy. To calculate the transition rates to final states with  $J_2 = 0, 2$  using the values given in Tab. 3.6 the rotational factor  $f_{\text{ROT}}$  has to be considered. The molecular radiation decay rates for the present case with atomic angular momenta 1 and 0 need to be summed over the polarization  $q$ , i.e.  $\gamma_{1\rightarrow 2} = \gamma_{\text{atom}} f_{\text{FCF}} \sum_q f_{\text{ROT}}$  and with the its rotational factor  $f_{\text{ROT}} = 2$ , a spontaneous decay rate from the state  $v_1 = -1$  in  $(a, c)1_u$  to  $v_2 = 39$   $J_2 = 0$  is  $\gamma_{1\rightarrow 2} = 0.54 \cdot 2 \cdot \gamma_{\text{atom}}$  and to  $v_2 = 39$   $J_2 = 2$  with its rotational factors  $f_{\text{ROT}} = \left(\frac{3}{5}, \frac{4}{5}, \frac{3}{5}\right)$  is  $\gamma_{1\rightarrow 2} = 0.15 \cdot \left(\frac{3}{5} + \frac{4}{5} + \frac{3}{5}\right) \cdot \gamma_{\text{atom}}$ . Therefore the efficient creation of the molecule in the ground state by the spontaneous decay is strongly depended on the combination of the Franck-Condon factor  $f_{\text{FCF}}$  and rotational factor  $f_{\text{ROT}}$ .

Tab. 3.6 gives also in the last line the remaining continuum contribution. The sum of all Franck-Condon factors of a single excited state differs slightly from one, because it only represents the part for electric dipole transitions while the spin-orbit mixing for the excited state results in a small component with total atomic angular momentum  $j = 2$ , which will not decay by electric dipole radiation to the ground state with  $j = 0$ .

### 3.3 Consequences for BEC creation for different isotopes

In a Bose-Einstein condensate the bosonic particles occupy the same state. The interaction between the particles can not be neglected and needs to be included into the Schrödinger equation. Theoretically this can be described by a mean-field approximation. In the effective single-particle non-linear Schrödinger equation, the so-called Gross-Pitaevskii equation [Dal96], a term  $U_{\text{int}} = \frac{4\pi\hbar^2 n a_{\text{bg}}}{m_{\text{atom}}}$  is inserted, where  $n$  is the particle density,  $a_{\text{bg}}$  is s-wave scattering length and  $m$  is the particle mass. Depending on the sign of the scattering length the effective interaction is repulsive or attractive and scales with the scattering length. In general a negative s-wave scattering leads to collapse of BEC. The creation of BEC for the species with negative scattering length is possible only under specific condition [Bra97].

In experiment the characteristic measure of BEC is the critical phase space density

$\rho_{\text{PSD}} = n \cdot \lambda_{\text{deBroglie}}^3$ , where  $\lambda_{\text{deBroglie}} = \sqrt{\frac{h}{2\pi m k_B T}}$  is the de Broglie wavelength. Above the critical  $\rho_{\text{PSD}}$  the atomic wavepackets start to overlap and the indistinguishability of atoms starts to be sufficient. In a harmonic trapping potential the phase space density  $\rho_{\text{PSD}}$  needs to be more than 1.2 of the value above for the formation of a BEC. Taking into account the finite atom number and their interaction the critical temperature  $T_c$  can be modified [Gio96].

The first Bose-Einstein condensate of bosonic  $^{40}\text{Ca}$  was achieved in 2009 [Kra09, App13] utilizing primarily the forced evaporation in the crossed dipole trap. The evaporation itself is based on decreasing the trap depth while the high energetic atoms leave the trapping volume, and the remaining atoms rethermalize due to collisions reaching slowly lower temperature. If the temperature becomes close to  $T_c$ , BEC starts to form. During the evaporation the competitive processes like the three-body recombination rate, which are depended on the scattering length, influence strongly the formation of the BEC. Due to the large the s-wave scattering length of  $308 a_0$  of  $^{40}\text{Ca}$  on the one hand the scattering between the atoms is high leading to an efficient evaporation, on the another hand the three-body recombination rate contributes significantly to the total atom losses from the cloud complicating essentially the creation of BEC. To avoid these losses the tilted beam of the dipole was shifted in propagation direction to decrease the atomic density. After this it was possible to create a  $^{40}\text{Ca}$  BEC in 1.5 s with  $1.2 \cdot 10^5$  atoms.

The bosonic calcium isotopes have the same electronic structure. The difference in the isotopes mass results in a shift of the total scattering phase [Fal07], which leads to different scattering lengths in the ground state. Considering their scattering lengths it is possible to estimate individual efficient way for creation of BEC.

The isotopes  $^{42}\text{Ca}$  and  $^{40}\text{Ca}$  have almost same scattering length therefore the cooling scheme from [App13] can be adopted almost unchanged.

The scattering length  $a = 399 a_0$  of  $^{44}\text{Ca}$  is larger than  $^{40}\text{Ca}$ , which will lead to increasing of the losses due to the three body losses, but it seems that it can be condensed e.g. by the decreasing the atomic density.

The formation of BEC for  $^{46}\text{Ca}$  with the really large  $a = 1970 a_0$  seems almost impossible with the current approach due to the huge three body recombination.

Due to the negative scattering length  $a = -281 a_0$  a creation BEC with  $^{48}\text{Ca}$  is only possible by using the techniques increasing the scattering length e.g. OFR.

The fermionic gas of  $^{43}\text{Ca}$  could be used for the formation of a Bardeen–Cooper–Schrieffer

regime or for the BEC of the molecules [Joc03], where controlled by the MFR the molecules formed by the three-body recombination condense in a long-lived thermal equilibrium state.





# Chapter 4

## Conclusions and outlook

In the thesis several novel experimental investigations in the physics of the ultracold calcium and their comparison to the currently established resonant scattering theory developed intensively in the last decade were presented.

The high intensity photoassociation spectra of the bound molecular states  $v' = -1$  in  $c0_u^+$  and  $v' = -1$  in  $(a, c)1_u$ , which were measured for first time by [Kah14b], were investigated in detail via *one-color photoassociation spectroscopy* with intensities up to  $600 \text{ Wcm}^{-2}$ . Assuming the molecular decay rate  $\gamma_{\text{mol}}$  being twice the atomic decay rate  $\gamma_{\text{atom}}$  the stimulated rate  $\gamma_{\text{stim}}$  could be calculated from the Franck-Condon densities, which are derived using the coupled channel model developed by Prof. Tiemann. These calculated stimulated rate  $\gamma_{\text{stim}}$  are in a good agreement both for the observed FWHM of the complete PA spectra and for the FWHM of the individual Lorentzian in the Voigt profiles confirming the validity of the theoretical description for the stimulated rates and the corresponding broadening. The resonance shapes calculated according to the resonant scattering theory show a good agreement with the observed spectral line shapes even at high intensities, by including Doppler and thermal effects.

Additionally experimental loss rate coefficients were derived, considering the dipole trap geometry. They were compared to the theoretical predictions. The theory predicts the line shapes and the losses at sufficiently low intensities. In contrast to the theory both the absolute values of the observed losses coefficients and the corresponding spectral areas, which are independent of the Doppler broadening, were smaller by a factor 16 in the low intensity region, did not show a saturation in the intermediate intensity region and exceed the calculated values in the high intensity region.

Based on the Franck-Condon densities the changes of scattering length for individual collision energies were calculated. In the large detuning region  $\Delta_1 > 500 \text{ kHz}$ , where the atomic loss are lower than 50 % of atomic number for an irradiation duration less than 50 ms, the calculated values of the scattering length vary from  $-200 a_0$  to  $+800 a_0$  for

the laser intensity of  $560 \text{ Wcm}^{-2}$  depending on the detuning from the bound molecular level  $v' = -1$  in  $c0_u^+$ . This result shows promising prospects of an application of low loss optical Feshbach resonances in  $^{40}\text{Ca}$ .

Such a light induced modification of the scattering length could be detected for example by a second PA laser on another resonance, where the stimulated rate is connected to the changes of the scattering length [Eno08].

A more quantitative approach of the determination of the induced photoassociative change would be achieved by the diffraction from a BEC. Using a standing wave beam of the OFR laser, a periodic variation of the mean field in a condensate induces a phase shift of the wavefunction in the BEC. After releasing the BEC from the trap this should lead to the diffraction of the cloud into the several momentum components [Yam10]. The low loss OFR can be used to increase the lifetime of BEC by reducing the three-body losses through optimization of the scattering length comparable to the realization by the MFR in magnetic Cs [Web03]. Also other interesting physical phenomena like solitons or even soliton trains are postulated to be excited by inducing a local change inside a BEC [Bec08].

The second topic of my work was measurement of the binding energies of four most weakly bound rovibrational molecular states in the ground potential  $X^1\Sigma_g^+$  of calcium dimer  $\text{Ca}_2$  via *two-color photoassociation spectroscopy* with kHz precision. For the measurement of these PA resonances the frequency stability of the required lasers was sufficiently improved. Especially the measurement of the weakest state  $v = 40 \text{ J} = 0$  with only  $\Delta_b = -h \cdot 1.608 \text{ MHz}$  from the ground state asymptote  $^1S_0 + ^1S_0$  benefited from the improved lasers technique. On the basis of the derived binding energies, Prof. Eberhard Tiemann was able to determine the long-range dispersion parameters  $C_6$ ,  $C_8$ ,  $C_{10}$  including retardation with high accuracy. Now, for the first time, combined with the inner part of the ground state potential measured earlier by [All03] the precise potential of the calcium dimer  $\text{Ca}_2$  in ground state is available.

By the improved ground state potential the s-wave scattering length  $a$  of  $^{40}\text{Ca}$  could be determined to  $308.5(50)a_0$  with the uncertainty improved by the factor more than 10. Additionally, using the Born-Oppenheimer approximation and mass scaling the s-wave scattering lengths of all stable calcium isotopes were derived.

By a coupled channel calculation performed by Prof. Eberhard Tiemann for the excited states the Franck-Condon factors (FCF) for the transitions from the bound levels of the states  $\Omega = 1_u$  and  $0_u^+$  of the coupled system  $a^3\Sigma_u^+$  and  $c^3\Pi_u$  to bound levels of the

ground state  $X^1\Sigma_g^+$  were calculated applying the improved potential. The calculated transition moment shows a good agreement with the experimental transition moment derived from the measurement of the splitting of the Autler-Townes doublets of the bound molecular state  $v' = -1$  in  $(a, c)1_u$  at different intensities. This verifies the assumption that the molecular dipole moment at large internuclear separation is  $\sqrt{2}$  times the atomic dipole moment.

The derived FCF can be used to calculate transition paths for an efficient creation of molecules in a predetermined rovibrational ground state. Due to the similar asymptotic behaviour of the ground and excited states only a few transitions to bound ground states show large FCF. This efficient spontaneous decay to selected states can be used as a starting level for the future experiments. For example about 54% of the molecules produced in the excited state  $v' = -1$  in  $(a, c)1_u$  are expected to decay to the ground state  $v = 39 J_2 = 0$ . These molecules can be used for the precision spectroscopy between the ground state rovibrational levels, transfer the molecules into deeper ground states or more precise scattering description.

Another route for future experiments is the usage of two-color photoassociation to convert an atomic BEC to a molecular BEC by stimulated Raman adiabatic passage (STIRAP). This mechanism is very promising with expected efficiency near unity [Mac00].

In conclusion, with this work a more complete understanding of high intensity photoassociation has been obtained. The achievements prepare the theoretical basis for novel experiments with alkaline earth metals, where the scattering length can be modified by low loss optical Feshbach resonances. The additional important milestone presented here is the precise determination of the long-range parameters including retardation effect, enabling a complete description of the ground state potential  $X^1\Sigma_g^+$  and a precise value of the  $^{40}\text{Ca}$  scattering length.



# Appendices

## Thermal average of $\gamma_{\text{stim}}$

In some cases the comfortable relation of the thermal averaged stimulated rate  $\gamma_{\text{stim}}$  is useful

$$\langle \gamma_{\text{stim}} \rangle = \frac{1}{k_{\text{B}}T} \int_0^{\infty} d\epsilon_{\text{col}} \exp\left(-\frac{\epsilon_{\text{col}}}{k_{\text{B}}T}\right) \gamma_{\text{stim}}(\epsilon_{\text{col}}). \quad (4.1)$$

The term  $\frac{1}{k_{\text{B}}T}$  fulfils the norm  $\int_0^{\infty} \exp\left(-\frac{\epsilon_{\text{col}}}{k_{\text{B}}T}\right) d\epsilon_{\text{col}} = k_{\text{B}}T$ . Setting the stimulated rate  $\gamma_{\text{stim}} = 2l_{\text{opt}}k\gamma_{\text{mol}}$  with  $k = \frac{\sqrt{2\mu\epsilon_{\text{col}}}}{\hbar}$  into Eq. 4.1

$$\langle \gamma_{\text{stim}} \rangle = \frac{1}{k_{\text{B}}T} \int_0^{\infty} d\epsilon_{\text{col}} \exp\left(-\frac{\epsilon_{\text{col}}}{k_{\text{B}}T}\right) 2l_{\text{opt}} \frac{\sqrt{2\mu\epsilon_{\text{col}}}}{\hbar} \gamma_{\text{mol}} \quad (4.2)$$

$$= \frac{\gamma_{\text{mol}} 2l_{\text{opt}}}{k_{\text{B}}T} \frac{\sqrt{2\mu}}{\hbar} \int_0^{\infty} d\epsilon_{\text{col}} \exp\left(-\frac{\epsilon_{\text{col}}}{k_{\text{B}}T}\right) \sqrt{\epsilon_{\text{col}}} \quad (4.3)$$

Using the antiderivate  $\int e^{-x/t} \sqrt{x} dx = \frac{\sqrt{\pi} t^{3/2}}{2} \text{Erf}\left(\frac{\sqrt{x}}{\sqrt{t}}\right) - t\sqrt{x} \cdot e^{-x/t} + C$ , where  $\text{Erf}(x)$  is the error function, the integral can be solved to

$$= \frac{\gamma_{\text{mol}} 2l_{\text{opt}}}{k_{\text{B}}T} \frac{\sqrt{2\mu}}{\hbar} \frac{\sqrt{\pi} (k_{\text{B}}T)^{3/2}}{2} \quad (4.4)$$

$$= \sqrt{\pi} l_{\text{opt}} \frac{\sqrt{2\mu k_{\text{B}}T}}{\hbar} \gamma_{\text{mol}}. \quad (4.5)$$

For  $T = 1.0 \mu\text{K}$  and  $l_{\text{opt}} = 8834 a_0$  is  $\langle \gamma_{\text{stim}} \rangle = 2\pi \cdot 2.8 \text{ s}^{-1}$ .

## Area under $\langle K_{\text{in}} \rangle_{\text{T}}$

For determination of areas under measured lines the following calculation (compare [Sim02]) are used

$$Area(\langle K_{in} \rangle_T) = \int_{-\infty}^{+\infty} \langle K_{in} \rangle_T d\Delta \quad (4.6)$$

$$= \frac{1}{h Q_T} \int_{-\infty}^{+\infty} \int_0^{+\infty} |S_{0,0}|^2 \exp\left(-\frac{\epsilon_{col}}{k_B T}\right) d\epsilon_{col} d\Delta \quad (4.7)$$

$$= \frac{1}{h Q_T} \int_{-\infty}^{+\infty} \int_0^{+\infty} \frac{\gamma_{mol} \gamma_{stim}(\epsilon_{col})}{\Delta^2 + \left(\frac{\gamma_{mol} + \gamma_{stim}(\epsilon_{col})}{2}\right)^2} \exp\left(-\frac{\epsilon_{col}}{k_B T}\right) d\epsilon_{col} d\Delta \quad (4.8)$$

The term  $\exp\left(-\frac{\epsilon_{col}}{k_B T}\right)$  is independent from  $\Delta$  and can be factor out.

$$Area(\langle K_{in} \rangle_T) = \frac{1}{h Q_T} \int_{-\infty}^{+\infty} \exp\left(-\frac{\epsilon_{col}}{k_B T}\right) \int_0^{+\infty} \frac{\gamma_{mol} \gamma_{stim}(\epsilon_{col})}{\Delta^2 + \left(\frac{\gamma_{mol} + \gamma_{stim}(\epsilon_{col})}{2}\right)^2} d\epsilon_{col} d\Delta \quad (4.9)$$

Using the antiderivate  $\int_{-\infty}^{+\infty} \frac{ab}{x^2 + \left(\frac{a+b}{2}\right)^2} = 2\pi \frac{ab}{a+b}$  one obtains

$$Area(\langle K_{in} \rangle_T) = \frac{1}{h Q_T} \int_0^{+\infty} \frac{2\pi \gamma_{mol} \gamma_{stim}(\epsilon_{col})}{\gamma_{mol} + \gamma_{stim}(\epsilon_{col})} \exp\left(-\frac{\epsilon_{col}}{k_B T}\right) d\epsilon_{col}. \quad (4.10)$$

Two cases will be discussed.

First case for  $\gamma_{mol} \gg \gamma_{stim}$ , and therefore  $\gamma_{mol} + \gamma_{stim} \approx \gamma_{mol}$ , is valid for the low PA intensities<sup>1</sup>. The integral can be sequentially solved as following

$$Area_1(\langle K_{in} \rangle_T) = \frac{2\pi}{h Q_T} \int_0^{+\infty} \gamma_{stim}(\epsilon_{col}) \exp\left(-\frac{\epsilon_{col}}{k_B T}\right) d\epsilon_{col}. \quad (4.11)$$

Now according to the Wigner threshold law [Jon99, Wig48] the stimulated rate is assumed to be  $\gamma_{stim} = 2l_{opt} \frac{\sqrt{2\mu\epsilon_{col}}}{\hbar} \gamma_{mol}$

$$Area_1(\langle K_{in} \rangle_T) = \frac{2\pi}{h Q_T} \int_0^{+\infty} 2l_{opt} \frac{\sqrt{2\mu\epsilon_{col}}}{\hbar} \gamma_{mol} \exp\left(-\frac{\epsilon_{col}}{k_B T}\right) d\epsilon_{col} \quad (4.12)$$

$$= \frac{2\pi}{h Q_T} 2l_{opt} \frac{\sqrt{2\mu}}{\hbar} \gamma_{mol} \int_0^{+\infty} \sqrt{\epsilon_{col}} \exp\left(-\frac{\epsilon_{col}}{k_B T}\right) d\epsilon_{col} \quad (4.13)$$

$$= 4\pi \frac{l_{opt} \sqrt{2\mu} \gamma_{mol}}{h Q_T \hbar} \cdot \frac{\sqrt{\pi} (k_B T)^{3/2}}{2} = \frac{2\pi l_{opt} \gamma_{mol} \hbar}{\mu}. \quad (4.14)$$

<sup>1</sup>This ansatz is also discussed in publications [MdE11, MdE08]

The areas in the low intensity region are independent from the temperature  $T$  and can be calculated under the observed PA spectrum by considering the trap volume  $V_{\text{DT}}$ :

$$Area_{\text{low}}(\beta) = \frac{2}{\sqrt{8}V_{\text{DT}}} Area_1(\langle K_{\text{in}} \rangle_{\text{T}}) = \frac{2}{\sqrt{8}V_{\text{DT}}} \cdot \frac{2\pi l_{\text{opt}} \gamma_{\text{mol}} h}{\mu}. \quad (4.15)$$

Due to the calcium narrow intercombination line  $\gamma_{\text{mol}}$  of  $2\pi \cdot 748 \text{ s}^{-1}$  this formula is valid in the really shallow intensity region  $I_1 < 10 \text{ Wcm}^{-2}$  (depending on the Frank-Condon density).

Another case is the numerical calculation for all possible  $\gamma_{\text{stim}}$ . Starting from Eq. 4.10,

$$Area_2(\langle K_{\text{in}} \rangle_{\text{T}}) = \frac{2\pi}{h Q_{\text{T}}} \int_0^\infty \frac{2l_{\text{opt}} \frac{\sqrt{2\mu\epsilon_{\text{col}}}}{\hbar} \gamma_{\text{mol}} \gamma_{\text{mol}}}{\gamma_{\text{mol}} + 2l_{\text{opt}} \frac{\sqrt{2\mu\epsilon_{\text{col}}}}{\hbar} \gamma_{\text{mol}}} \exp\left(-\frac{\epsilon_{\text{col}}}{k_{\text{B}}T}\right) d\epsilon_{\text{col}} \quad (4.16)$$

$$= \frac{2\pi \gamma_{\text{mol}}}{h Q_{\text{T}}} \int_0^\infty \frac{2l_{\text{opt}} \frac{\sqrt{2\mu}}{\hbar} \sqrt{\epsilon_{\text{col}}}}{1 + 2l_{\text{opt}} \frac{\sqrt{2\mu}}{\hbar} \sqrt{\epsilon_{\text{col}}}} \exp\left(-\frac{\epsilon_{\text{col}}}{k_{\text{B}}T}\right) d\epsilon_{\text{col}}. \quad (4.17)$$

The integral can be numerically approximated. The graphical representation of its solution are shown in Fig. 4.1.

In the region of low intensity (small  $l_{\text{opt}}$  Fig. 4.1 - left) of the solution the area reproduces the linear behaviour of Eq. 4.15, but in the region of high intensities is saturated. In the analysis of the high power measurements Sect. 2.3 the numerical solution is used as follow:

$$Area(\beta) = \frac{2}{\sqrt{8}V_{\text{DT}}} Area_2(\langle K_{\text{in}} \rangle_{\text{T}}) = \frac{2}{\sqrt{8}V_{\text{DT}}} \frac{2\pi \gamma_{\text{mol}}}{h Q_{\text{T}}} \cdot \text{Solution}(l_{\text{opt}}(I_1), T) \quad (4.18)$$

Notice that the  $Area_{\text{complete}}$  for different temperatures have the same values in the region of the low intensities. That occurs due to  $Q_{\text{T}} \propto T^{3/2}$  compare Eq. 4.15.

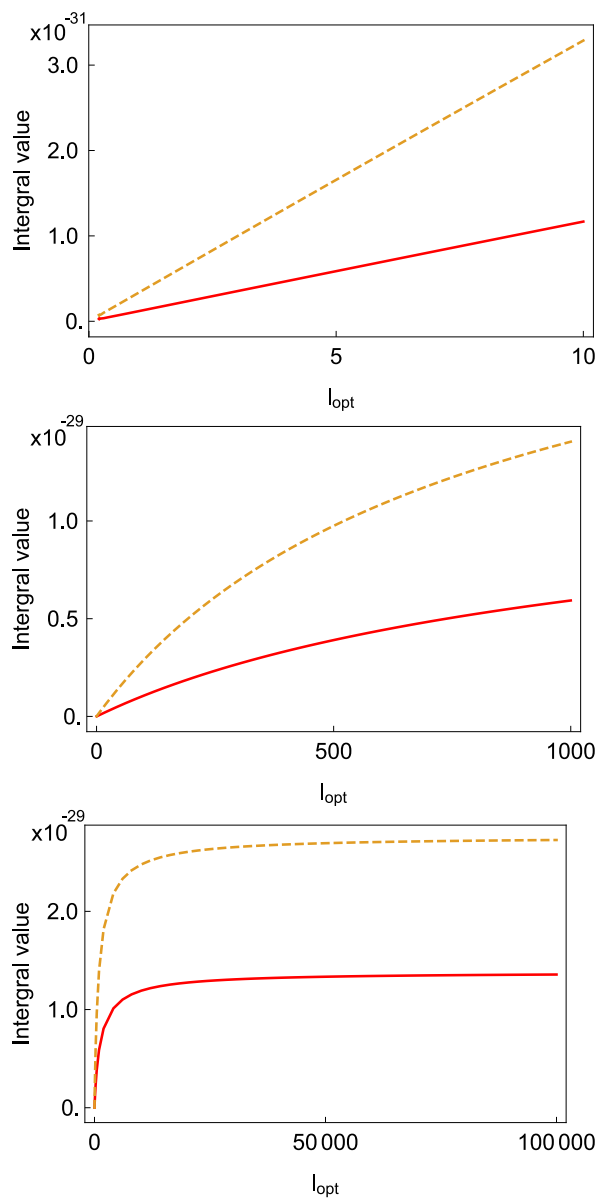


Figure 4.1: Graphical representation of the integral in dependency of the optical length for temperatures of  $2 \mu K$  (orange dashed line) and  $1 \mu K$  (red line)



## Bibliography

- [Abr97] E. R. I. Abraham, W. I. McAlexander, J. M. Gerton, R. G. Hulet, R. Côté and A. Dalgarno, “Triplet  $s$ -wave resonance in  ${}^6\text{Li}$  collisions and scattering lengths of  ${}^6\text{Li}$  and  ${}^7\text{Li}$ ”, *Phys. Rev. A*, **55**, R3299–R3302 (1997).
- [All02] O. Allard, A. Pashov, H. Knöckel and E. Tiemann, “Ground-state potential of the Ca dimer from Fourier-transform spectroscopy”, *Phys. Rev. A*, **66**, 042503–1–9 (2002).
- [All03] O. Allard, C. Samuelis, A. Pashov, H. Knöckel and E. Tiemann, “Experimental study of the  $\text{Ca}_2$   ${}^1\text{S} + {}^1\text{S}$  asymptote”, *Eur. Phys. J. D*, **26**, 155–164 (2003).
- [App13] Oliver Appel, *Bose-Einstein Condensation and Narrow-Line Photoassociation Spectroscopy of Calcium*, Ph.D. thesis, Fakultät für Mathematik und Physik der Gottfried Wilhelm Leibniz Universität Hannover (2013), 08/2013 eingereichte Version.
- [Aut55] S. H. Autler and C. H. Townes, “Stark effect in rapidly varying fields”, *Phys. Rev.*, **100**, 703–722 (1955).
- [Bec08] Christoph Becker, Simon Stellmer, Parvis Soltan-Panahi, Sören Dörscher, Mathis Baumert, Eva-Maria Richter, Jochen Kronjäger, Kai Bongs and Klaus Sengstock, “Oscillations and interactions of dark and dark-bright solitons in Bose-Einstein condensates”, *Nature Physics*, **4**, 496 – 501 (2008).
- [Bel12] K. Beloy, J. A. Sherman, N. D. Lemke, N. Hinkley, C. W. Oates and A. D. Ludlow, “Determination of the  $5d6s$   ${}^3D_1$  state lifetime and blackbody-radiation clock shift in Yb”, *Phys. Rev. A*, **86**, 051404 (2012).
- [Bev89] N. Beverini, F. Giammanco, E. Maccioni, F. Strumia and G. Vissani, “Measurement of the calcium  ${}^1P_1$ - ${}^1D_2$  transition rate in a laser-cooled atomic beam”, *J. Opt. Soc. Am. B*, **6**, 2188–2193 (1989).

- [Bin01a] T. Binnewies, “Neuartige Kühlverfahren zur Erzeugung ultrakalter Ca-Atome”, PTB-Bericht PTB-Opt-65, Physikalisch–Technische Bundesanstalt, Braunschweig (2001).
- [Bin01b] T. Binnewies, G. Wilpers, U. Sterr, F. Riehle, J. Helmcke, T. E. Mehlstäubler, E. M. Rasel and W. Ertmer, “Doppler cooling and trapping on forbidden transitions”, *Phys. Rev. Lett.*, **87**, 123002–1–4 (2001).
- [Boh96] John L. Bohn and P. S. Julienne, “Semianalytic treatment of two-color photoassociation spectroscopy and control of cold atoms”, *Phys. Rev. A*, **54**, R4637–R4640 (1996).
- [Boh97] John L. Bohn and P. S. Julienne, “Prospects for influencing scattering lengths with far-off-resonant light”, *Phys. Rev. A*, **56**, 1486–1491 (1997).
- [Boh99] John L. Bohn and P. S. Julienne, “Semianalytic theory of laser-assisted resonant cold collisions”, *Phys. Rev. A*, **60**, 414–425 (1999).
- [Bra97] C. C. Bradley, C. A. Sackett and R. G. Hulet, “Bose-Einstein condensation of lithium: Observation of limited condensate number”, *Phys. Rev. Lett.*, **78**, 985–989 (1997).
- [Chi85] Marita C. Chidichimo, “Evaluation of the specific mass shift and field shift in the alkaline-earth Sr atom”, *Zeitschrift für Physik A Hadrons and Nuclei*, **321**, 549–555 (1985).
- [Chi10] Cheng Chin, Rudolf Grimm, Paul Julienne and Eite Tiesinga, “Feshbach resonances in ultracold gases”, *Rev. Mod. Phys.*, **82**, 1225–1286 (2010).
- [Chu85] S. Chu, L. Hollberg, J. E. Bjorkholm, A. Cable and A. Ashkin, “Three-dimensional viscous confinement and cooling of atoms by resonance radiation pressure”, *Phys. Rev. Lett.*, **55**, 48–51 (1985).
- [Ciu04] R. Ciuryło, E. Tiesinga, S. Kotochigova and P. S. Julienne, “Photoassociation spectroscopy of cold alkaline-earth-metal atoms near the intercombination line”, *Phys. Rev. A*, **70**, 062710 (2004).
- [Ciu05] R. Ciuryło, E. Tiesinga and P. S. Julienne, “Optical tuning of the scattering length of cold alkaline-earth-metal atoms”, *Phys. Rev. A*, **71**, 030701–1–4 (2005).

- [Com00] D. Comparat, C. Drag, B. Laburthe Tolra, A. Fioretti, P. Pillet, A. Crubellier, O. Dulieu and F. Masnou-Seeuws, “Formation of cold  $\text{Cs}_2$  ground state molecules through photoassociation in the  $1_u$  pure long-range state”, *Eur. Phys. J. D*, **11**, 59–71 (2000).
- [Dal96] F. Dalfovo, L. Pitaevskii and S. Stringari, “The condensate wave function of a trapped atomic gas”, *J. Res. Natl. Inst. Stand. Technol.*, **101**, 537–544 (1996).
- [Deg04a] Carsten Degenhardt, *Freie und gespeicherte Calcium-Atome für ein optisches Frequenznormal*, Ph.D. thesis, Universität Hannover, Welfengarten 1 (2004), online available at <http://www.tib.uni-hannover.de>.
- [Deg04b] Carsten Degenhardt, Hardo Stoehr, Uwe Sterr, Fritz Riehle and Christian Lisdat, “Wavelength dependent ac-Stark shift of the  $^1\text{S}_0$ - $^3\text{P}_1$  transition at 657 nm in Ca”, *Phys. Rev. A*, **70**, 023414–1–6 (2004).
- [Deg05] Carsten Degenhardt, Hardo Stoehr, Christian Lisdat, Guido Wilpers, Harald Schnatz, Burghard Lipphardt, Tatiana Nazarova, Paul-Eric Pottie, Uwe Sterr, Jürgen Helmcke and Fritz Riehle, “Calcium optical frequency standard with ultracold atoms: Approaching  $10^{-15}$  relative uncertainty”, *Phys. Rev. A*, **72**, 062111–1–17 (2005).
- [Der03] A. Derevianko, S.G. Porsev, S. Kotochigova, E. Tiesinga and P.S. Julienne, “Ultracold collision properties of metastable alkaline-earth atoms”, *Phys. Rev. Lett.*, **90**, 063002 (2003).
- [Edm57] A. R. Edmonds, *Angular momentum in quantum mechanics*, Princeton University Press, Princeton, New Jersey (1957).
- [Eno08] K. Enomoto, K. Kasa, M. Kitagawa and Y. Takahashi, “Optical Feshbach resonance using the intercombination transition”, *Phys. Rev. Lett.*, **101**, 203201 (2008).
- [Ert85] W. Ertmer, R. Blatt, J. L. Hall and M. Zhu, “Laser manipulation of atomic beam velocities: Demonstration of stopped atoms and velocity reversal”, *Phys. Rev. Lett.*, **54**, 996 (1985).

- [Fal07] Stephan Falke, Eberhard Tiemann and Christian Lisdat, “Born-Oppenheimer approximation for mass scaling of cold-collision properties”, *Phys. Rev. A*, **76**, 012724–1–7 (2007).
- [Fal08] St. Falke, H. Knöckel, J. Friebe, M. Riedmann, E. Tiemann and Ch. Lisdat, “Potassium ground-state scattering parameters and Born-Oppenheimer potentials from molecular spectroscopy”, *Phys. Rev. A*, **78**, 012503–1–13 (2008).
- [Fal14] Stephan Falke, Nathan Lemke, Christian Grebing, Burghard Lipphardt, Stefan Weyers, Vladislav Gerginov, Nils Huntemann, Christian Hagemann, Ali Al-Masoudi, Sebastian Häfner, Stefan Vogt, Uwe Sterr and Christian Lisdat, “A strontium lattice clock with  $3 \times 10^{-17}$  inaccuracy and its frequency”, *New J. Phys.*, **16**, 073023 (2014).
- [Fan61] U. Fano, “Effects of configuration interaction on intensities and phase shifts”, *Phys. Rev.*, **124**, 1866–1878 (1961).
- [Fat00] F. K. Fatemi, K. M. Jones and P. D. Lett, “Observation of optically induced Feshbach resonances in collisions of cold atoms”, *Phys. Rev. Lett.*, **85**, 4462–4465 (2000).
- [Fed96] P. O. Fedichev, Yu. Kagan, G. V. Shlyapnikov and J. T. M. Walraven, “Influence of nearly resonant light on the scattering length in low-temperature atomic gases”, *Phys. Rev. Lett.*, **77**, 2913–2916 (1996).
- [Gio96] S. Giorgini, L. P. Pitaevskii and S. Stringari, “Condensate fraction and critical temperature of a trapped interacting Bose gas”, *Phys. Rev. A*, **54**, R4633–R4636 (1996).
- [Gri93] G. F. Gribakin and V. V. Flambaum, “Calculation of the scattering length in atomic collisions using the semiclassical approximation”, *Phys. Rev. A*, **48**, 546–553 (1993).
- [Gri05] A. Griesmaier, J. Werner, S. Hensler, J. Stuhler and T. Pfau, “Bose-Einstein condensation of chromium”, *Phys. Rev. Lett.*, **94**, 160401–1–4 (2005).
- [GUM08] “Evaluation of measurement data – guide to the expression of uncertainty in measurement”, *JCGM 100:2008* (2008).

- [Hän75] T. W. Hänsch and A. L. Schawlow, “Cooling of gases by laser radiation”, *Opt. Commun.*, **13**, 68–69 (1975).
- [Hän80] T. W. Hänsch and B. Couillaud, “Laser frequency stabilization by polarization spectroscopy of a reflecting reference cavity”, *Opt. Commun.*, **35**, 441–444 (1980).
- [Hun14] N. Huntemann, B. Lipphardt, Chr. Tamm, V. Gerginov, S. Weyers and E. Peik, “Improved limit on a temporal variation of  $m_p/m_e$  from comparisons of Yb<sup>+</sup> and Cs atomic clocks”, *Phys. Rev. Lett.*, **113**, 210802 (2014).
- [Ing98] M. Inguscio, S. Stringari and C. Wieman, editors, *Collisional dynamics of ultra-cold atomic gases*, volume 140 of *International School of Physics Enrico Fermi* (1998), ISBN 0 9673355 5 8.
- [Joc03] S. Jochim, M. Bartenstein, A. Altmeyer, G. Hendl, S. Riedl, C. Chin, J. Hecker Denschlag and R. Grimm, “Bose-Einstein condensation of molecules”, *Science*, **302**, 2101–2103 (2003).
- [Jon99] Kevin M. Jones, Paul D. Lett, Eite Tiesinga and Paul S. Julienne, “Fitting line shapes in photoassociation spectroscopy of ultracold atoms: A useful approximation”, *Phys. Rev. A*, **61**, 012501 (1999).
- [Jon06] Kevin M. Jones, Eite Tiesinga, Paul D. Lett and Paul S. Julienne, “Ultracold photoassociation spectroscopy: Long-range molecules and atomic scattering”, *Rev. Mod. Phys.*, **78**, 483–535 (2006).
- [Jun08] M. Junker, D. Dries, C. Welford, J. Hitchcock, Y. P. Chen and R. G. Hulet, “Photoassociation of a Bose-Einstein condensate near a Feshbach resonance”, *Phys. Rev. Lett.*, **101**, 060406 (2008).
- [Kah14a] Max Kahmann, *Link Between Photoassociation and Optical Feshbach Resonances Through the Example of Calcium*, Ph.D. thesis, QUEST-Leibniz-Forschungsschule der Gottfried-Wilhelm-Leibniz Universität Hannover (2014), online.
- [Kah14b] Max Kahmann, Eberhard Tiemann, Oliver Appel, Uwe Sterr and Fritz Riehle, “Photoassociation spectroscopy of <sup>40</sup>Ca measured with kilohertz accuracy near the <sup>3</sup>P<sub>1</sub>+<sup>1</sup>S<sub>0</sub> asymptote and its Zeeman effect”, *Phys. Rev. A*, **89**, 023413 (2014).

- [Kim04] J. Kim, U.D. Rapol, S. Moal, J. Léonard, M. Walhout and M. Leduc, “Photoassociation experiments with ultracold metastable helium”, *Eur. Phys. J. D*, **31**, 227–237 (2004).
- [Kit08] Masaaki Kitagawa, Katsunari Enomoto, Kentaro Kasa, Yoshiro Takahashi, Roman Ciuryło, Pascal Naidon and Paul S. Julienne, “Two-color photoassociation spectroscopy of ytterbium atoms and the precise determinations of s-wave scattering lengths”, *Phys. Rev. A*, **77**, 012719 (2008).
- [Kra09] Sebastian Kraft, Felix Vogt, Oliver Appel, Fritz Riehle and Uwe Sterr, “Bose-Einstein condensation of alkaline earth atoms:  $^{40}\text{Ca}$ ”, *Phys. Rev. Lett.*, **103**, 130401 (2009).
- [Lel87] L. P. Lellouch and L. R. Hunter, “Measurement of the  $4s4p\ ^1\text{P}-4s3d\ ^1\text{D}$  spontaneous emission rate in calcium by use of a Stark-electric-quadrupole interference”, *Phys. Rev. A*, **36**, 3490–3493 (1987).
- [Lim08] Lih-King Lim, C. Morais Smith and Andreas Hemmerich, “Staggered-vortex superfluid of ultracold bosons in an optical lattice”, *Phys. Rev. Lett.*, **100**, 130402 (2008).
- [Lis02] Ch. Lisdat, N. Vanhaecke, D. Comparat and P. Pillet, “Line shape analysis of two-colour photoassociation spectra on the example of the  $\text{Cs}_2$  ground state”, *Eur. Phys. J. D*, **21**, 299–309 (2002).
- [Lis16] C. Lisdat, G. Grosche, N. Quintin, C. Shi, S. M. F. Raupach, C. Grebing, D. Nicolodi, F. Stefani, A. Al-Masoudi, S. Dörscher, S. Häfner, J.-L. Robyr, N. Chiodo, S. Bilicki, E. Bookjans, A. Koczwar, S. Koke, A. Kuhl, F. Wiotte, F. Meynadier, E. Camisard, M. Abgrall, M. Lours, T. Legero, H. Schnatz, U. Sterr, H. Denker, C. Chardonnet, Y. Le Coq, G. Santarelli, A. Amy-Klein, R. Le Targat, J. Lodewyck, O. Lopez and P.-E. Pottie, “A clock network for geodesy and fundamental science”, *Nature Communications*, **7**, 12443 EP – (2016), article.
- [Mac00] M. Mackie, R. Kowalski and J. Javanainen, “Bose-stimulated Raman adiabatic passage in photoassociation”, *Phys. Rev. Lett.*, **84**, 3803–3806 (2000).

- [Mac01] Mette Machholm, Paul S. Julienne and Kalle-Antti Suominen, “Calculations of collisions between cold alkaline earth atoms in a weak laser field”, *Phys. Rev. A*, **64**, 033425–1–19 (2001).
- [Mar04] H. S. Margolis, G. P. Barwood, G. Huang, H. A. Klein, S. N. Lea, K. Szymaniec and P. Gill, “Hertz-level measurement of the optical clock frequency in a single  $^{88}\text{Sr}^+$  ion”, *Science*, **306**, 1355–1358 (2004).
- [McG15a] B. H. McGuyer, M. McDonald, G. Z. Iwata, W. Skomorowski, R. Moszynski and T. Zelevinsky, “Control of optical transitions with magnetic fields in weakly bound molecules”, *Phys. Rev. Lett.*, **115**, 053001 (2015).
- [McG15b] B. H. McGuyer, M. McDonald, G. Z. Iwata, M. G. Tarallo, A. T. Grier, F. Apfelbeck and T. Zelevinsky, “High-precision spectroscopy of ultracold molecules in an optical lattice”, *New J. Phys.*, **17**, 055004 (2015).
- [McG15c] Bart H. McGuyer, Mickey McDonald, Geoffrey Z. Iwata, Marco G. Tarallo, Wojciech Skomorowski, Robert Moszynski and Tanya Zelevinsky, “Precise study of asymptotic physics with subradiant ultracold molecules”, *Nature Physics*, **11**, 32–36 (2015).
- [McK02] C. McKenzie, J. Hecker Denschlag, H. Häffner, A. Browaeys, Luís E. E. de Araujo, F. K. Fatemi, K. M. Jones, J. E. Simsarian, D. Cho, A. Simoni, E. Tiesinga, P. S. Julienne, K. Helmerson, P. D. Lett, S. L. Rolston and W. D. Phillips, “Photoassociation of sodium in a Bose-Einstein condensate”, *Phys. Rev. Lett.*, **88**, 120403 (2002).
- [MdE08] Y. N. Martinez de Escobar, P. G. Mickelson, P. Pellegrini, S. B. Nagel, A. Traverso, M. Yan, R. Côté and T. C. Killian, “Two-photon photoassociative spectroscopy of ultracold  $^{88}\text{Sr}$ ”, *Phys. Rev. A*, **78**, 062708 (2008).
- [MdE11] Yenny Natali Martinez de Escobar, *Bose-Einstein Condensation of  $^{84}\text{Sr}$* , Ph.D. thesis, Rice University, Houston (2011).
- [Meh03] T. E. Mehlstäubler, J. Keupp, A. Douillet, N. Rehbein, E. M. Rasel and W. Ertmer, “Modelling three-dimensional-quench cooling for alkaline-earth atoms”, *J. Opt. B: Quantum Semiclass. Opt.*, **5**, S183–S189 (2003).
- [Mes99] D. Meschede, *Optik, Licht und Laser*, Teubner Studienbücher (1999).

- [Mes11] Vladimir V. Meshkov, Andrey V. Stolyarov and Robert J. Le Roy, “Rapid, accurate calculation of the s-wave scattering length”, *J. Chem. Phys.*, **135**, 154108 (2011).
- [Mid12] Thomas Middelmann, Stephan Falke, Christian Lisdat and Uwe Sterr, “High accuracy correction of blackbody radiation shift in an optical lattice clock”, *Phys. Rev. Lett.*, **109**, 263004 (2012).
- [Mit08] J. Mitroy and J.-Y. Zhang, “Properties and long range interactions of the calcium atom”, *J. Chem. Phys.*, **128**, 134305 (2008).
- [Mos03] Robert Moszynski, Grzegorz Łach, Michał Jaszuński and Béatrice Bussery-Honvault, “Long-range relativistic interactions in the cowan-griffin approximation and their qed retardation: Application to helium, calcium, and cadmium dimers”, *Phys. Rev. A*, **68**, 052706 (2003).
- [Nap94] R. Napolitano, J. Weiner, Carl. J. Williams and Paul S. Julienne, “Line shapes of high resolution photoassociation spectra of optically cooled atoms”, *Phys. Rev. Lett.*, **73**, 1352–1355 (1994).
- [Naz07] Tatiana Nazarova, *Towards the Quantum Noise Limit in Ramsey-Bordé Atom Interferometry*, Ph.D. thesis, Fakultät für Mathematik und Physik der Gottfried Wilhelm Leibniz Universität Hannover (2007), Online available at <http://www.tib.uni-hannover.de>.
- [Nic15] T.L. Nicholson, S. Blatt, B.J. Bloom, J.R. Williams, J.W. Thomsen, J. Ye, Paul S. Julienne, T. L. Nicholson, B. J. Bloom, J. R. Williams, J. W. Thomsen, J. Ye and Paul S. Julienne, “Optical Feshbach resonances: Field-dressed theory and comparison with experiments”, *Phys. Rev. A*, **92**, 022709 (2015).
- [Pac17] Evgenij Pachomow, Veit Peter Dahlke, Eberhard Tiemann, Fritz Riehle and Uwe Sterr, “Ground-state properties of  $\text{Ca}_2$  from narrow-line two-color photoassociation”, *Phys. Rev. A*, **95**, 043422 (2017).
- [Por02] S. G. Porsev and A. Derevianko, “High-accuracy relativistic many-body calculations of van der Waals coefficients  $C_6$  for alkaline-earth-metal atoms”, *Phys. Rev. A*, **65**, 020701(R) (2002).



- [Por06] S. G. Porsev and A. Derevianko, “High-accuracy calculations of dipole, quadrupole, and octupole electric dynamic polarizabilities and van der Waals coefficients  $C_6$ ,  $C_8$ , and  $C_{10}$  for alkaline-earth dimers”, *J. Exp. Theor. Phys.*, **102**, 195–205 (2006).
- [Pro85] J. Prodan, A. Migdall, W. Phillips, I. So, H. Metcalf and J. Dalibard, “Stopping atoms with laser light”, *Phys. Rev. Lett.*, **54**, 992–995 (1985).
- [Qué12] Goulven Quéméner and Paul S. Julienne, “Ultracold molecules under control!”, *Chemical Reviews*, **112**, 4949–5011 (2012).
- [Raa87] E. L. Raab, M. Prentiss, A. Cable, S. Chu and D. E. Pritchard, “Trapping of neutral sodium atoms with radiation pressure”, *Phys. Rev. Lett.*, **59**, 2631–2634 (1987).
- [Reg03] Cindy A. Regal, Christopher Ticknor, John L. Bohn and Deborah S. Jin, “Creation of ultracold molecules from a Fermi gas of atoms”, *Nature*, **424**, 47–50 (2003).
- [San03] Robin Santra and Chris H. Greene, “Tensorial analysis of the long-range interaction between metastable alkaline-earth-metal atoms”, *Phys. Rev. A*, **67**, 062713 (2003).
- [Sch05] T. Schneider, E. Peik and Chr. Tamm, “Sub-Hertz optical frequency comparisons between two trapped  $^{171}\text{Yb}$  ions”, *Phys. Rev. Lett.*, **94**, 230801–1–4 (2005).
- [Sch08] André Schirotzek, Yong il Shin, Christian H. Schunck and Wolfgang Ketterle, “Determination of the superfluid gap in atomic Fermi gases by quasi-particle spectroscopy”, *Phys. Rev. Lett.*, **101**, 140403 (2008).
- [Sim02] A. Simoni, P. S. Julienne, E. Tiesinga and C. J. Williams, “Intensity effects in ultracold photoassociation line shapes”, *Phys. Rev. A*, **66**, 063406 (2002).
- [Ste03] Uwe Sterr, Tomas Binnewies, Carsten Degenhardt, Guido Wilpers, Jürgen Helmcke and Fritz Riehle, “Prospects of Doppler cooling on forbidden lines”, *J. Opt. Soc. Am. B*, **20**, 985 (2003).

- [Ste09] Simon Stellmer, Meng Khoon Tey, Bo Huang, Rudolf Grimm and Florian Schreck, “Bose-Einstein condensation of Strontium”, *Phys. Rev. Lett.*, **103**, 200401 (2009).
- [Swa11] Matthew D. Swallows, Michael Bishof, Yige Lin, Sebastian Blatt, Michael J. Martin, Ana Maria Rey and Jun Ye, “Suppression of collisional shifts in a strongly interacting lattice clock”, *Science*, **331**, 1043–1046 (2011).
- [Tho87] H. R. Thorsheim, J. Weiner and P. S. Julienne, “Laser-induced photoassociation of ultracold sodium atoms”, *Phys. Rev. Lett.*, **58**, 2420–2423 (1987).
- [Tie03] Eberhard Tiemann, *Cold Atoms and Molecules*, chapter Cold Molecules, 175–214, Wiley-VCH (2003).
- [Tie15] Eberhard Tiemann, Max Kahmann, Evgenij Pachomow, Fritz Riehle and Uwe Sterr, “Nonlinear Zeeman effect in photoassociation spectra of  $^{40}\text{Ca}$  near the  $^3\text{P}_1 + ^1\text{S}_0$  asymptote”, *Phys. Rev. A*, **92**, 023419 (2015).
- [Tsa97] C. C. Tsai, R. S. Freeland, J. M. Vogels, H. M. J. M. Boesten, B. J. Verhaar and D. J. Heinzen, “Two-color photoassociation spectroscopy of ground state  $\text{Rb}_2$ ”, *Phys. Rev. Lett.*, **79**, 1245–1248 (1997).
- [Ulm12] Juris Ulmanis, Johannes Deiglmayr, Marc Repp, Roland Wester and Matthias Weidemüller, “Ultracold molecules formed by photoassociation: Heteronuclear dimers, inelastic collisions, and interactions with ultrashort laser pulses”, *Chemical Reviews*, **112**, 4890–4927 (2012).
- [vA99] F. A. van Abeelen and B. J. Verhaar, “Determination of collisional properties of cold Na atoms from analysis of bound-state photoassociation and Feshbach resonance field data”, *Phys. Rev. A*, **59**, 578–584 (1999).
- [Van04] N. Vanhaecke, Ch. Lisdat, B. T’Jampens, D. Comparat, A. Crubellier and P. Pillet, “Accurate asymptotic ground state potential curves of  $\text{Cs}_2$  from two-colour photoassociation”, *Eur. Phys. J. D*, **28**, 351–360 (2004).
- [Vog07] F. Vogt, Ch. Grain, T. Nazarova, U. Sterr, F. Riehle, Ch. Lisdat and E. Tiemann, “Determination of the calcium ground state scattering length by photoassociation spectroscopy at large detunings”, *Eur. Phys. J. D*, **44**, 73–79 (2007).

- [Vog09] Felix Vogt, *Creation of cold and dense ensembles of calcium atoms*, Ph.D. thesis, Gottfried Wilhelm Leibniz Universität Hannover (2009), Online available at <http://www.tib.uni-hannover.de>.
- [Vog16] Stefan Vogt, Sebastian Häfner, Jacopo Grotti, Silvio Koller, Ali Al-Masoudi, Uwe Sterr and Christian Lisdat, “A transportable optical lattice clock”, *Journal of Physics: Conference Series*, **723**, 012020 (2016).
- [Wan00] H. Wang, A. N. Nikolov, J. R. Ensher, P. L. Gould, E. E. Eyler, W. C. Stwalley, J. P. Burke, J. L. Bohn, Chris. H. Greene, E. Tiesinga, C. J. Williams and P. S. Julienne, “Ground-state scattering lengths for potassium isotopes determined by double-resonance photoassociative spectroscopy of ultracold  $^{39}\text{K}$ ”, *Phys. Rev. A*, **62**, 052704 (2000).
- [Web03] Tino Weber, Jens Herbig, Michael Mark, Hanns-Christoph Nägerl and Rudolf Grimm, “Three-body recombination at large scattering lengths in an ultracold atomic gas”, *Phys. Rev. Lett.*, **91**, 123201 (2003).
- [Wig48] Eugene P. Wigner, “On the behavior of cross sections near thresholds”, *Phys. Rev.*, **73**, 1002–1009 (1948).
- [Wil95] R. S. Williamson III and T. Walker, “Magneto-optical trapping and ultracold collisions of potassium atoms”, *J. Opt. Soc. Am. B*, **12**, 1393–1397 (1995).
- [Yam10] Rekishu Yamazaki, Shintaro Taie, Seiji Sugawa and Yoshiro Takahashi, “Submicron scale spatial modulation of an interatomic interaction in a Bose-Einstein condensate”, *Phys. Rev. Lett.*, **105**, 050405–1–4 (2010).
- [Yan13a] Mi Yan, *Optical Feshbach Resonances and Coherent Photoassociation in a Strontium BEC*, Ph.D. thesis, Rice University, Houston (2013).
- [Yan13b] Mi Yan, B. J. DeSalvo, Ying Huang, P. Naidon and T. C. Killian, “Rabi oscillations between atomic and molecular condensates driven with coherent one-color photoassociation”, *Phys. Rev. Lett.*, **111**, 150402 (2013).
- [Zel06] T. Zelevinsky, M. M. Boyd, A. D. Ludlow, T. Ido, J. Ye, R. Ciuryło, P. Naidon and P. S. Julienne, “Narrow line photoassociation in an optical lattice”, *Phys. Rev. Lett.*, **96**, 203201 (2006).

- [Zwi03] Martin W. Zwierlein, Zoran Hadzibabic, Subhadeep Gupta and Wolfgang Ketterle, “Spectroscopic insensitivity to cold collisions in a two-state mixture of fermions”, *Phys. Rev. Lett.*, **91**, 250404 (2003).

# Publications

## Conference contributions

- Evgenij Pachomow, Veit Dahlke, Eberhard Tiemann, Uwe Sterr and Fritz Riehle  
*Two-colour photoassociation spectroscopy in  $^{40}\text{Ca}$  near the  $^3P_1 - ^1S_0$  asymptote*  
International Workshop on Ultracold Group II Atoms, Paris (poster) 2016
- Veit Dahlke, Evgenij Pachomow, Eberhard Tiemann, Uwe Sterr and Fritz Riehle  
*Precision two-color spectroscopy of long-range ground-state vibrational levels in ultracold  $^{40}\text{Ca}$*   
Deutsche physikalische Gesellschaft Frühjahrstagung, Hannover (poster) 2016
- Uwe Sterr, Evgenij Pachomow, Veit Dahlke, Eberhard Tiemann and Fritz Riehle  
*Lineshapes in narrow-line one and two-color photoassociation of ultracold calcium*  
23th international conference on spectral line shapes, Torun (talk) 2016
- Fritz Riehle, Evgenij Pachomow, Max Kahmann, Veit Dahlke, Eberhard Tiemann and Uwe Sterr  
*One and two-colour photoassociation spectroscopy in  $^{40}\text{Ca}$  near the  $^3P_1 - ^1S_0$  asymptote*  
International conference on laser spectroscopy, Singapore (poster) 2015
- Evgenij Pachomow, Veit Dahlke, Eberhard Tiemann, Uwe Sterr and Fritz Riehle  
*Improved ground-state scattering length of calcium by two-color photoassociation*  
Gordon research conference / atomic physics, Newport RI (poster) 2015
- Veit Dahlke, Evgenij Pachomow, Eberhard Tiemann, Uwe Sterr and Fritz Riehle  
*Improved ground-state scattering length of  $^{40}\text{Ca}$  by two-color photoassociation*  
Deutsche physikalische Gesellschaft Frühjahrstagung, Heidelberg (poster) 2015
- Fritz Riehle, Evgenij Pachomow, Max Kahmann, Eberhard Tiemann and Uwe Sterr  
*Building Molecules with Light*  
Tokyo university of science, Tokyo (talk) 2014

- Evgenij Pachomow, Max Kahmann, Eberhard Tiemann, Uwe Sterr and Fritz Riehle  
*Towards optical Feshbach resonances with  $^{40}\text{Ca}$*   
International conference on atomic physics, Washington (poster) 2014
- Max Kahmann, Evgenij Pachomow, Eberhard Tiemann, Uwe Sterr and Fritz Riehle  
*Ultra stable laser system for two color photoassociation of Ca*  
Deutsche physikalische Gesellschaft Frühjahrstagung, Berlin (poster) 2014
- Evgenij Pachomow, Max Kahmann, Uwe Sterr, Fritz Riehle and Eberhard Tiemann  
*Towards optical Feshbach resonances with  $^{40}\text{Ca}$*   
Deutsche physikalische Gesellschaft Frühjahrstagung, Berlin (talk) 2014
- Max Kahmann, Eberhard Tiemann, Evgenij Pachomow, Uwe Sterr and Fritz Riehle  
*Photoassociation spectroscopy of ultracold  $^{40}\text{Ca}$  near the  $^1S_0 + ^3P_1$  asymptote*  
Division seminar University of Torun (talk) 2014
- Evgenij Pachomow, Max Kahmann, Uwe Sterr, Fritz Riehle and Eberhard Tiemann  
*Towards optical Feshbach resonances with  $^{40}\text{Ca}$*   
Research training group 1729 seminar, Hannover (talk) 2013
- Max Kahmann, Evgenij Pachomow, Eberhard Tiemann, Fritz Riehle and Uwe Sterr  
*Optical Feshbach Resonances with Calcium at the  $^1S_0 + ^3P_1$  Asymptote*  
Research training group 1729 workshop, Visselhövede (poster) 2013
- Evgenij Pachomow, Max Kahmann, Eberhard Tiemann, Fritz Riehle and Uwe Sterr  
*Photoassociation of Ultracold Calcium at the  $^1S_0 + ^3P_1$  Asymptote*  
Research training group 1729 workshop, Visselhövede (poster) 2013
- Evgenij Pachomow, Max Kahmann, Oliver Appel, Fritz Riehle, Uwe Sterr and Eberhard Tiemann  
*Photoassociation of Ultracold Calcium at the  $^1S_0 + ^3P_1$  Asymptote*  
Young atom opticians conference, Birmingham (poster) 2013

- Max Kahmann, Oliver Appel, Evgenij Pachomow, Fritz Riehle and Uwe Sterr  
*Optical Feshbach Resonances with  $^{40}\text{Ca}$*   
Atomic physics seminar, Oberjoch (talk) 2013
- Max Kahmann, Oliver Appel, Evgenij Pachomow, Fritz Riehle and Uwe Sterr  
*Optical Feshbach Resonances with  $^{40}\text{Ca}$*   
Optical clock seminar, Braunschweig (talk) 2013
- Marcel Marschewski, Evgenij Pachomow, Oliver Höfft, Wolfgang Maus-Friedrichs, Frank Enders  
*Investigation of the growth of thin Ionic Liquids films on Au(111) and HOPG*  
Deutsche physikalische Gesellschaft Frühjahrstagung, Dresden (poster) 2011
- Evgenij Pachomow, Marcel Marschewski, Oliver Höfft, Wolfgang Maus-Friedrichs, Frank Enders  
*Deposition of silver nanoparticles on to thin films of ionic liquid on  $\text{SiO}_2$*   
Deutsche physikalische Gesellschaft Frühjahrstagung, Regensburg (poster) 2010
- Lothar Klarhöfer, Evgenij Pachomow, Wolfgang Maus-Friedrichs, Wolfgang Viöl  
*Valence band spectroscopy on plasma treated wood surface*  
Deutsche physikalische Gesellschaft Frühjahrstagung, Dresden (poster) 2010

## Reviewed publications

- Evgenij Pachomow, Veit Dahlke, Eberhard Tiemann, Fritz Riehle and Uwe Sterr  
*Ground-state properties of  $\text{Ca}_2$  from narrow line two-color photoassociation*  
Phys. Rev. A, **95**, 043422, 2017
- Eberhard Tiemann, Max Kahmann, Evgenij Pachomow, Fritz Riehle and Uwe Sterr  
*Nonlinear Zeeman effect in photoassociation spectra of  $^{40}\text{Ca}$  near the  $^3P_1 + ^1S_0$  asymptote*  
Phys. Rev. A, **92**, 023419, 2015
- Angela Keppler, Marcel Himmerlich, Tomonori Ikari, Marcel Marschewski, Evgenij Pachomow, Oliver Höfft, Wolfgang Maus-Friedrichs, Frank Endres, Stefan Krischok  
*Changes of the near-surface chemical composition of the 1-ethyl-3-methylimidazolium*

*bis(trifluoromethylsulfonyl)imide room temperature ionic liquid under the influence of irradiation.*

Chem Phys., **13**, 1174-81, 2011



# Danksagung

Ich möchte mich bei allen bedanken, die mich während dieser Zeit unterstützt und diese Arbeit ermöglicht haben:

- Meiner Ehefrau Olga, die stets ein Ohrchen für meine Probleme hatte und mich immer unterstützte
- Herrn Prof. Dr. Fritz Riehle und Herrn Dr. Uwe Sterr für die Betreuung meiner Arbeit und intensive Unterstützung, insbesondere in der letzten Phase der Arbeit
- Herrn Prof. Dr. Eberhard Tiemann für die Betreuung und sehr lehrreiche Gespräche, die mir immer ein bisschen Erleuchtung gebracht haben, und für seine Unterstützung durch die theoretischen Simulation
- Frau Prof. Dr. Silke Ospelkaus für die Betreuung als Mentorin im Rahmen des Graduiertenkollegs und für die stets aufmunternden Worte
- Herrn M. Sc. Veit Peter Dahlke für die Unterstützung in Labor und vor allem für seine lockere Art und entspannte Gespräche einerseits und die intensiven und interessanten Diskussionen über alles, angefangen von den Trivialitäten bis zu Physik
- Herrn Dr. Max Kahmann und Herrn Dr. Oliver Appel, die mich in die Geheimnisse des Calciumreiches und der vielen Laser eingeweiht haben
- Herrn Dr. Dan-Gheorghita Matei, Herrn Dipl. Phys. Robin Weyrich für die angenehmen Gespräche und gute Laune
- Herrn Dr. Sebastian Häfner, Herrn Dr. Ali Al-Masoudi, Herrn Dr. Stephan Vogt, Frau M. Sc. Sofia Herbers, Herrn Dipl. Ing. Roman Schwarz für die interessanten Gespräche und angenehmes Arbeitsklima
- Frau Dr. Gesine Grosche, Herrn Dr. Sören Dörscher, Herrn Dr. Thomas Legero für die allgemeinen Diskussionen wissenschaftlicher und privater Natur

- Herrn Dipl. Ing. Mattias Misera, Herrn Andre Uhde, Herrn Klemens Budin für die technische Unterstützung und insbesondere Herrn Dipl. Ing. Andreas Koczvara für die Lösungen der zunächst unlösbar erschienenen Probleme mit der Elektronik
- Frau Susanne Ehrenpfordt und Frau Birgit Ohlendorf für die Unterstützung in den Verwaltungsvorgängen und aller Formalien

# Lebenslauf

## Persönliche Daten

Evgenij Pachomow

Friedrich-Ebert-Platz 20, 31226 Peine

deutsch

08.11.1980 / Celinnoe (ehem. USSR)

verheiratet, eine Tochter

mail: [evgenij.pachomow@goolgemail.com](mailto:evgenij.pachomow@goolgemail.com)



## Bildung

- seit 01/2013      Wissenschaftlicher Mitarbeiter an der Physikalisch-Technischen Bundesanstalt in Braunschweig
- 10/2004–08/2011      Diplom "Physik und Physikalische Technologien" an der TU Clausthal.  
Schwerpunkt: Atom- und Molekülphysik an Oberflächen
- 08/2001–04/2004      Erwerb der Hochschulreife in Göttingen
- 10/2000–04/2001      Stipendiat der Otto-Benecke-Stiftung in Hannover
- 10/1999              Einreise nach Deutschland
- 09/1998-09/1999      Studium "Messtechnik und Kontrollmethoden der Qualität" an der Staatlichen Technischen Universität Omsk / Russland

10.02.2017